Interaction Note

Note 343

March 1978

Transient Electromagnetic Characterization of Arbitrary Conducting Bodies Through an Aperture-Perforated Conducting Screen

Korada R. Umashankar
Carl E. Baum
Air Force Weapons Laboratory

Abstract

A general procedure for the systematic transient characterization of arbitrarily shaped conducting bodies placed behind an aperture-perforated conducting screen is discussed. Coupled integro-differential equations are derived for the complex coupled boundary value problem. A few specific examples of aperture-wire scatterer or antenna geometries are treated both analytically and numerically for transient electromagnetic characterization based on the singularity expansion method. Both the frequency and time domain results are given for the coupled problem.

TABLE OF CONTENTS

ILLUSTRATIONS

ILLUSTRATIONS (Cont'd.)

ILLUSTRATIONS (Cont'd.)

ILLUSTRATIONS (Cont'd.)

ILLUSTRATIONS (Cont'd.)

INTRODUCTION

Electromagnetic transient excitation of arbitrarily shaped objects through an aperture-perforated conducting screen is a complex interaction problem. This has been given special attention recently, particularly in the broad area of EMP interaction and other related simulation applications. Also, a great deal of effort is being applied to assessing the electromagnetic effects on the protected objects behind screen in the event of external transient nuclear explosions.[1,2] This problem of aperture coupling and penetration of electromagnetic energy has been studied by many investigators to characterize general complex aperture shapes in the form of holes, slits in a ground screen[3-5] or in a scattering body itself,[6,7] which are of practical importance in the electromagnetic pulse and in interference studies. But the transient analysis and the subsequent characteristic response prediction become a still further involved process if there are other scattering objects in the vicinity of apertures, wherein one has to take into account fully the mutual interaction between them.[8.9]

As such diffraction by complex aperture shapes has been studied extensively by both analytical and numerical methods, basically in the frequency domain, based on the formulation of integral equations for the aperture-screen boundary value problem. A circular aperture,[4,10] rectangular aperture,[5,11-13] narrow finite slot and infinitely long slot[14] in a conducting screen as canonical problems give a basic foundation to the treatment of general aperture shapes in a screen.

This paper reports the preliminary investigation of the interaction problem in terms of a set of coupled integro-differential equations for a general conducting scatterer placed behind an arbitrarily shaped aperture-perforated conducting screen. Basically this turns out to be a three-body scattering problem or a two-body scattering problem with a leaky ground plane due to the presence of the aperture. Further, the following specific hybrid combinations are characterized from the integral equation formulations:

- i) narrow finite slot
- ii) array of narrow finite slots
- iii) single or multi-infinite slots
- iv) square and circular apertures

in the presence of simple objects in the form of

- i) finite straight wire
- ii) array of straight wires
- iii) infinitely long single and multiple wires
- iv) two-dimension plate surfaces

Both the frequency-domain and the time-domain characterization is discussed based on the extensive application of the Singularity Expansion Method.[2] Some numerical results are reported to explain various types of interaction.

CHAPTER I

General Formulation of the Aperture-Scatterer Integral Equation

The problem of electromagnetic coupling to a general conducting scatterer behind an aperture-perforated conducting screen is formulated in terms of a set of integro-differential equations. In figure 1.1 is shown the geometry of the interaction problem discussed, wherein S_a is an arbitrary shaped aperture in an infinite, perfectly conducting screen assumed to be in xy-plane, separating two half-space media. The left-hand space (medium 1) and the right-hand space (medium 2) respectively have permeability, permittivity and conductivity of $(\mu_-, \varepsilon_-, \sigma_-)$ and $(\mu_+, \varepsilon_+, \sigma_+)$ as their characteristics. The incident field $(\tilde{\vec{E}}^i, \tilde{\vec{H}}^i)$ is assumed to exist in left-hand space medium 1 and illuminates the aperture. The perfectly conducting general-shaped scatterer S_c is in the right-hand space (medium 2) (shadow side), which has direct electromagnetic coupling to the aperture S_a.

In the following a set of coupled integral equations are derived by treating the tangential aperture electric field $\tilde{\vec{E}}_{t_a}$ or the equivalent magnetic current $\tilde{\vec{J}}_{s_m} = -\tilde{\vec{E}}_{t_a} \times \vec{1}_z$ and the equivalent induced electric current distribution $\tilde{\vec{J}}_s$ on the conducting scatterer as unknowns.

In figures 1.2 and 1.3 are indicated the step-by-step reduction of the original problem to an equivalent problem by invoking both image theory and field equivalence principle valid for only $z < 0$ and $z > 0$ respectively. Based on figure 1.2 the total magnetic field $\tilde{\vec{H}}_-$ and the total electric field $\tilde{\vec{E}}_-$ valid for $z < 0$, can be written[14,15] in terms of the scattered field due to the equivalent magnetic current $\tilde{\vec{J}}_{s_m}$ and the short-circuited fields $(\tilde{\vec{E}}_{sc_-}, \tilde{\vec{H}}_{sc_-})$,

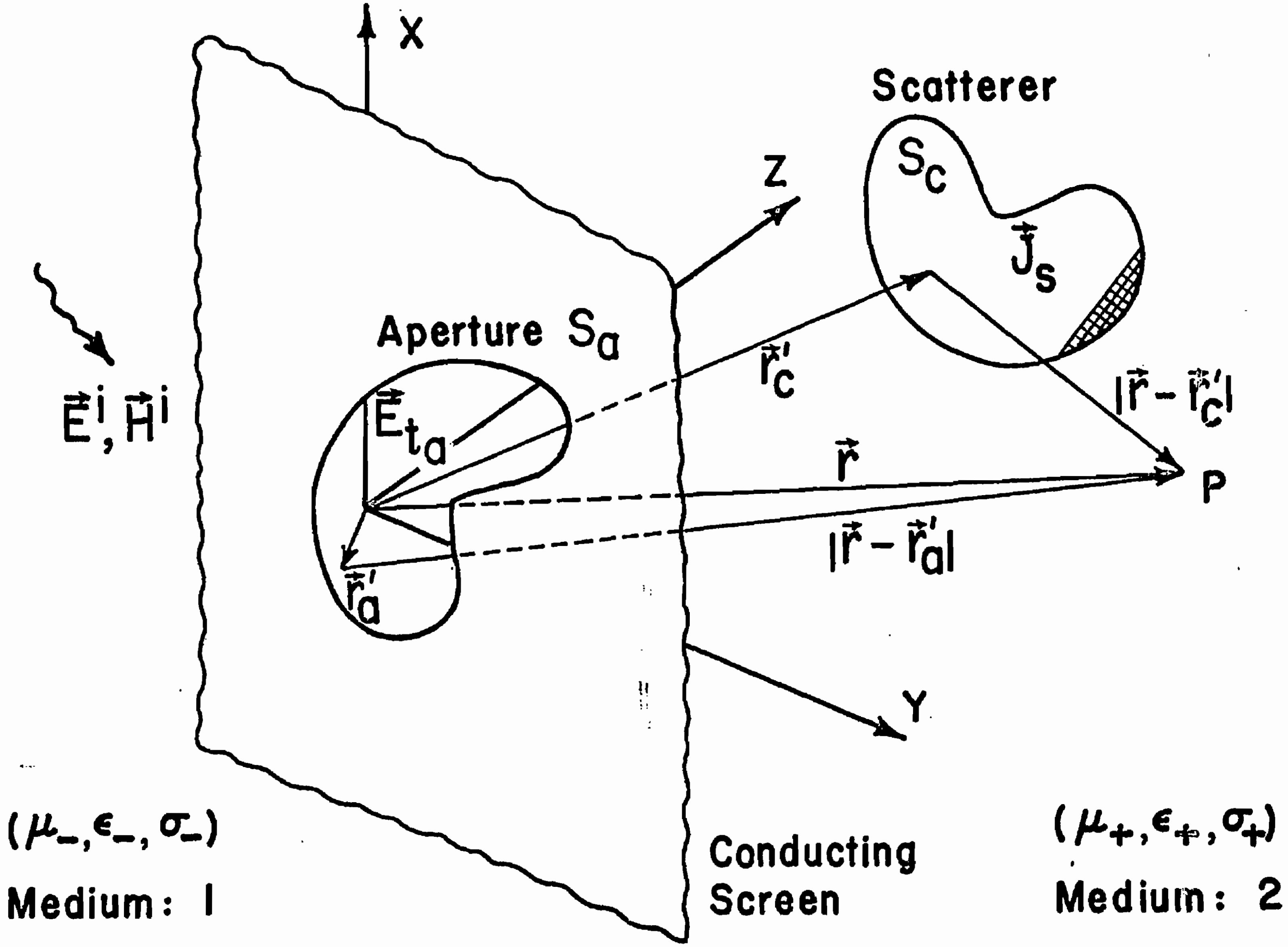

Figure 1.1 Conducting Scatterer Behind an Aperture Perforated Conducting Screen

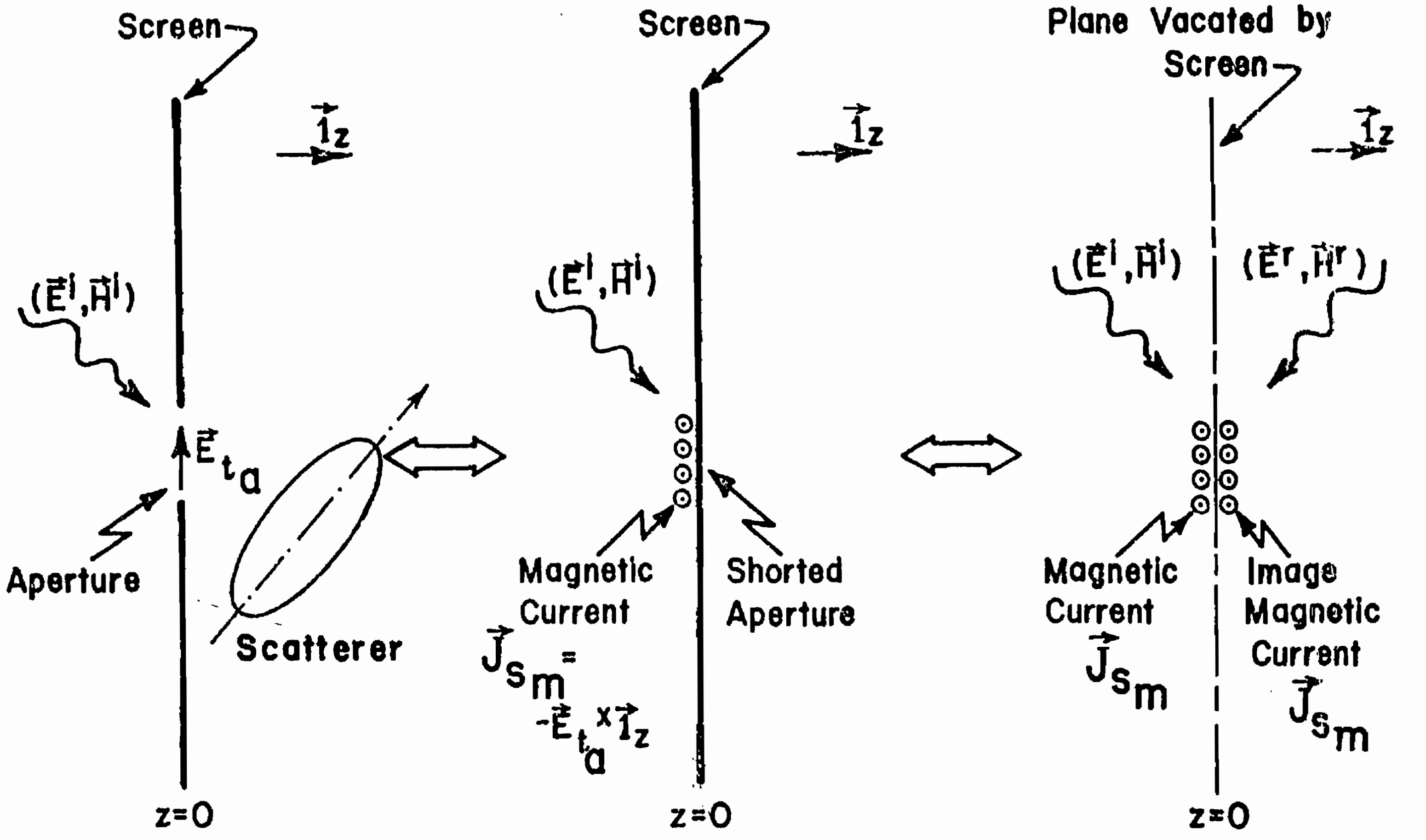

ORIGINAL PROBLEM
(VALID EVERYWHERE)
(a)

EQUIVALENT PROBLEM
(VALID, Z<0)
(b)

EQUIVALENT PROBLEM
(VALID, Z<0)
(c)

Figure 1.2 Illuminated Half-Space Equivalences

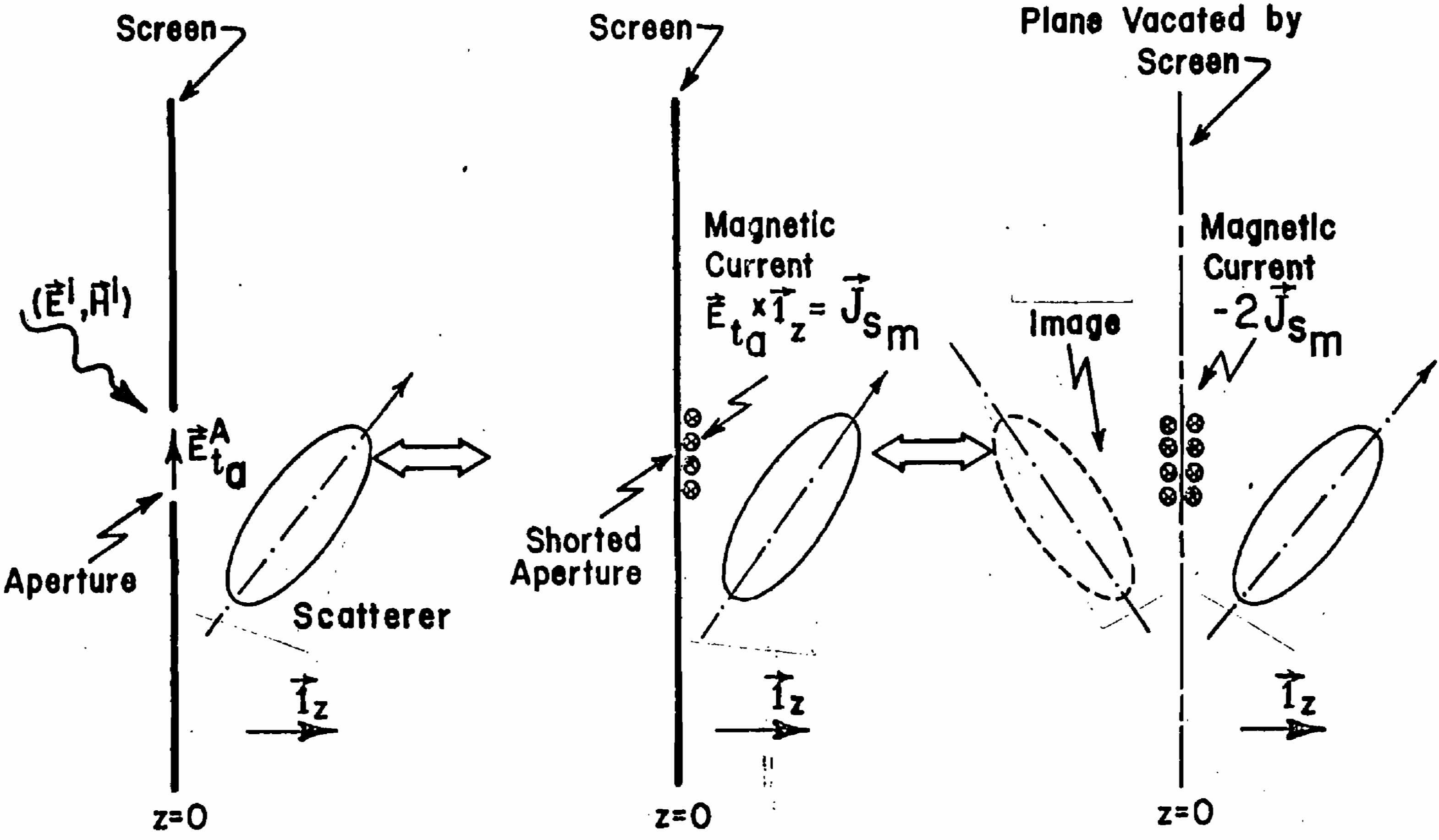

ORIGINAL PROBLEM
(VALID EVERYWHERE)
(a)

EQUIVALENT PROBLEM
(VALID, Z>0)
(b)

EQUIVALENT PROBLEM
(VALID, Z>0)
(c)

Figure 1.3 Shadow Half-Space Equivalences

$$\tilde{\vec{H}}_-(\vec{r},s) = \frac{s}{\gamma_-^2}\left[\nabla\left(\nabla \cdot \tilde{\vec{A}}_{m_-}(\vec{r},s)\right) - \gamma_-^2\tilde{\vec{A}}_{m_-}(\vec{r},s)\right] + \tilde{\vec{H}}_{sc_-}(\vec{r},s)$$

$$z < 0 \qquad (1.1)$$

$$\tilde{\vec{E}}_-(\vec{r},s) = -\frac{s}{(\sigma_- + s\varepsilon_-)}\nabla \times \tilde{\vec{A}}_{m_-}(\vec{r},s) + \tilde{\vec{E}}_{sc_-}(\vec{r},s)$$

$$z < 0 \qquad (1.2)$$

Similarly, referring to figure 1.3, the total magnetic field $\tilde{\vec{H}}_+$ and the total electric field $\tilde{\vec{E}}_+$ valid for $z > 0$, is written[14,15] in terms of the scattered field due to the equivalent magnetic current $-\tilde{\vec{J}}_{s_m}$ and due to the induced electric current $\tilde{\vec{J}}_s$ on the conducting scatterer in the presence of the perfect ground screen,

$$\tilde{\vec{H}}_+(\vec{r},s) = -\frac{s}{\gamma_+^2}\left[\nabla\left(\nabla \cdot \tilde{\vec{A}}_{m_+}(\vec{r},s)\right) - \gamma_+^2\tilde{\vec{A}}_{m_+}(\vec{r},s)\right] + \frac{1}{\mu_+}\nabla \times \tilde{\vec{A}}_+(\vec{r},s) \qquad z > 0 \qquad (1.3)$$

$$\tilde{\vec{E}}_+(\vec{r},s) = \frac{s}{\gamma_+^2}\left[\nabla\left(\nabla \cdot \tilde{\vec{A}}_+(\vec{r},s)\right) - \gamma_+^2\tilde{\vec{A}}_+(\vec{r},s)\right] + \frac{s}{(\sigma_+ + s\varepsilon_+)}\nabla \times \tilde{\vec{A}}_{m_+}(\vec{r},s) \qquad z > 0 \qquad (1.4)$$

In the expressions (1.1) to (1.4) the electric vector potential is given by

$$\tilde{\vec{A}}_{m_\pm}(\vec{r},s) = \frac{(\sigma_\pm + s\varepsilon_\pm)}{2\pi s}\iint\limits_{S_a} \tilde{\vec{J}}_{s_m}(\vec{r}_a{}',s)\,\tilde{G}_\pm(\vec{r},\vec{r}_a{}';s)\,dx_a'dy_a' \qquad (1.5)$$

$$\tilde{G}_\pm(\vec{r},\vec{r}\,';s) = \frac{e^{-\gamma_\pm|\vec{r}-\vec{r}_a{}'|}}{|\vec{r}-\vec{r}_a{}'|} \qquad (1.6)$$

$$|\vec{r}-\vec{r}_a{}'| = \left[(x-x_a')^2 + (y-y_a')^2 + z^2\right]^{\frac{1}{2}} \qquad (1.7)$$

and the magnetic vector potential $\tilde{\vec{A}}_+$ due to the conducting scatterer S_c and its image S_i is given by

$$\tilde{\vec{A}}_+(\vec{r},s) = \frac{\mu_+}{4\pi}\left[\iint_{S_c} \tilde{\vec{J}}_s(\vec{r}\,'_c,s)\ \tilde{g}(\vec{r},\vec{r}\,'_c;s)\ ds'_c + \iint_{S_i} \tilde{\vec{J}}_{s_i}(\vec{r}\,'_i,s)\ \tilde{g}(\vec{r},\vec{r}\,'_i;s)\ ds'_i\right] \tag{1.8}$$

$$\tilde{g}(\vec{r},\vec{r}\,'_{c,i};s) = \frac{e^{-\gamma_+|\vec{r}-\vec{r}\,'_{c,i}|}}{|\vec{r}-\vec{r}\,'_{c,i}|} \tag{1.9}$$

and the propagation constant referred to each side of the medium

$$\gamma_\pm = [s\mu_\pm(\sigma_\pm + s\varepsilon_\pm)]^{\frac{1}{2}} \tag{1.10}$$

in which s is the complex frequency with e^{st} field variations being assumed in the above field expressions. In fact s is the two-sided Laplace transform variable, and in deriving the above field expressions the following Laplace transform is applied to convert the field quantities from time domain to the complex frequency domain,^{2}

$$\tilde{f}(s) \equiv \int_{-\infty}^{\infty} f(t)\ e^{-st}\ dt \tag{1.11}$$

whose inverse transform has the form

$$f(t) = \frac{1}{2\pi j}\int_{\Omega_o-j\infty}^{\Omega_o+j\infty} \tilde{f}(s)\ e^{st}\ ds \tag{1.12}$$

with $\Omega_1 < \mathrm{Re}[s] < \Omega_z$ defining the strip of convergence and with the inversion contour in this strip $(\Omega_1 < \Omega_o < \Omega_2)$.

A coupled set of integro-differential equations can now be formed using expressions (1.1) to (1.4) by enforcing the appropriate boundary condition across the aperture and on the scatterer, that the transverse-to-z component of the magnetic field should be continuous across the aperture S_a and the tangential electric field should be zero on the conducting surface S_c of the scatterer,

$$\lim_{z \to (0-)} \tilde{\vec{H}}_-(\vec{r},s) = \lim_{z \to (0+)} \tilde{\vec{H}}_+(\vec{r},s) \tag{1.13}$$

and

$$\vec{1}_{S_c}(\vec{r}) \times \tilde{\vec{E}}_+(\vec{r},s) = \vec{0} \qquad \vec{r} \in S_c \tag{1.14}$$

where $\vec{1}_{S_c}$ is the outward-pointing unit vector on S_c. Hence, substituting the expressions (1.1) and (1.3) into the aperture boundary condition (1.13), we have,

$$\begin{aligned} &\frac{s}{\gamma_-^2}\left[\nabla\left(\nabla \cdot \tilde{\vec{A}}_{m_-}(\vec{r},s)\right) - \gamma_-^2 \tilde{\vec{A}}_{m_-}(\vec{r},s)\right] \times \vec{1}_z \\ &\quad + \frac{s}{\gamma_+^2}\left[\nabla\left(\nabla \cdot \tilde{\vec{A}}_{m_+}(\vec{r},s)\right) - \gamma_+^2 \tilde{\vec{A}}_{m_+}(\vec{r},s)\right] \times \vec{1}_z \\ &\quad - \frac{1}{\mu_+}\left[\nabla \times \tilde{\vec{A}}_+(\vec{r},s)\right] \times \vec{1}_z = - \tilde{\vec{H}}_{sc_-}(\vec{r},s) \times \vec{1}_z \\ &\qquad \vec{r} \in S_a \end{aligned} \tag{1.15}$$

Similarly, substituting the expression (1.4) into the conducting-scatterer boundary condition (1.14), we have

$$\begin{aligned} &\frac{s}{\gamma_+^2}\left[\nabla\left(\nabla \cdot \tilde{\vec{A}}_+(\vec{r},s)\right) - \gamma_+^2 \tilde{\vec{A}}_+(\vec{r},s)\right] \\ &\quad + \frac{s}{(\sigma_+ + s\varepsilon_+)} \nabla \times \tilde{\vec{A}}_{m_+}(\vec{r},s) = \vec{0} \qquad \vec{r} \in S_c \end{aligned} \tag{1.16}$$

In principle, the expressions (1.15) and (1.16) are the exact set of coupled integral equations for the complex case of a scattering conducting body behind an aperture-perforated conducting screen in terms of the unknown magnetic current distribution $\tilde{\vec{J}}_{sm}(\vec{r},s)$ in S_a and the induced electric current $\tilde{\vec{J}}_s(\vec{r},s)$ on S_c.

One may also note that the short-circuit magnetic field on the right-hand side of (1.15) is related to the incident magnetic field,

$$\tilde{\vec{H}}_{sc_-}(\vec{r},s) = 2\tilde{\vec{H}}^i(\vec{r},s) \tag{1.17}$$

In many instances the left-hand side medium and the right-hand side medium will have same medium characteristics (μ, ε, σ); in such case the + and - subscripts in the expression (1.15) and (1.16) can be dropped and further the following coupled integral equations result:

$$\left[\nabla\left(\nabla \cdot \tilde{\vec{A}}_m(\vec{r},s)\right) - \gamma^2\tilde{\vec{A}}_m(\vec{r},s)\right] \times \vec{1}_z - \frac{(\sigma + s\varepsilon)}{2}\left[\nabla \times \tilde{\vec{A}}(\vec{r},s)\right] \times \vec{1}_z = -\frac{\gamma^2}{s}\,\tilde{\vec{H}}^i(\vec{r},s) \times \vec{1}_z \qquad \vec{r} \in S_a \tag{1.18}$$

and

$$\left[\nabla\left(\nabla \cdot \tilde{\vec{A}}(\vec{r},s)\right) - \gamma^2\tilde{\vec{A}}(\vec{r},s)\right] + s\mu\,\nabla \times \tilde{\vec{A}}_m(\vec{r},s) = \vec{0} \qquad \vec{r} \in S_c \tag{1.19}$$

The electric vector potential $\tilde{\vec{A}}_m$ and the magnetic vector potential $\tilde{\vec{A}}$ introduced in the above expressions (1.18) and (1.19) are still given by the expressions (1.5) and (1.8) respectively after dropping the medium subscripts + and - in those definitions.

For analyzing the antenna problem, figure 1.4, one has to introduce slight modifications in the expressions (1.15) and (1.16). Since there is no incident field in the left-side medium 1, the right-hand side term in the expression (1.15) is equated to zero. Further, the boundary condition on the conducting surface S_c is that the tangential electric field is zero except at the antenna

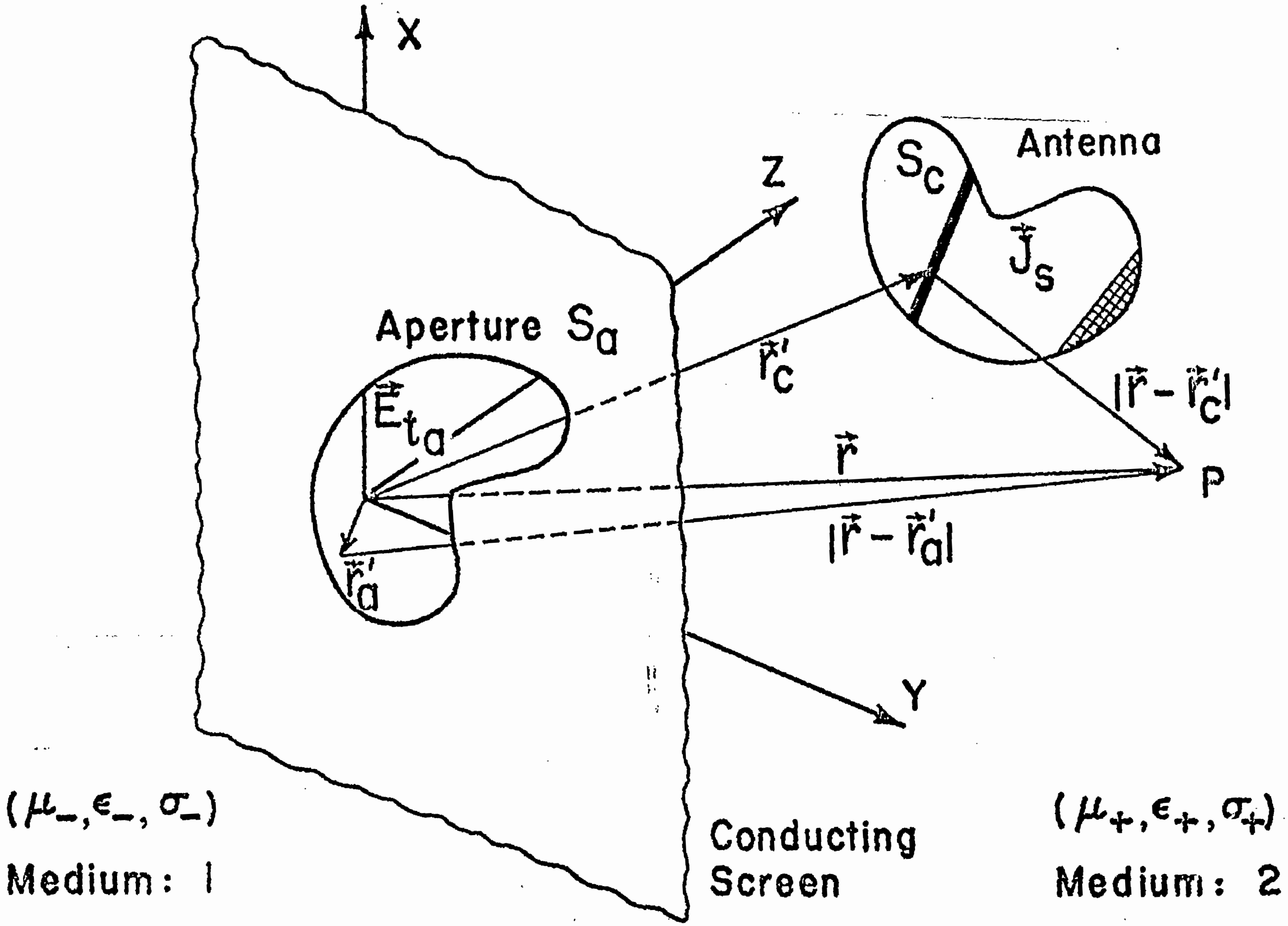

Figure 1.4 Antenna Behind an Aperture Perforated Conducting Screen

gaps across which excitation source generator is connected. Hence, the right-hand side of the expression (1.16) is replaced by $\tilde{\vec{E}}_s(\vec{r})(\vec{r} \in S_i)$ where $\tilde{\vec{E}}_s(\vec{r})$ is given appropriate source distribution on S_c. If both the incident field in the left-hand side medium and source generator at the structure are present simultaneously, one can invoke the superposition principle and analyze the problem in steps. The case when there exists incident excitation fields in both media 1 and 2, can be handled appropriately by introducing the difference of the two short-circuit fields $(\tilde{\vec{H}}_{sc-}(\vec{r},s) - \tilde{\vec{H}}_{sc+}(\vec{r},s))$ into the right-hand side of the expression (1.15) instead of the term $\tilde{\vec{H}}_{sc-}(\vec{r},s)$.

As stated earlier, the expressions (1.15) and (1.16) are the general set of coupled integro-differential equations derived in the complex frequency domain. For a specified geometry S_a of the aperture and S_c of the conducting scatterer, to obtain the current density responses the coupled integral equations are to be solved. If one is interested only with the time-harmonic solution, it is obtained by making the substitution $s = j\omega$, and similarly the time-domain responses can be obtained by taking the inverse transform, as defined by the expression (1.12), of the frequency domain solution. The expressions (1.15) and (1.16) can be written in a compact operator notation

$$\left\langle \left[\tilde{\overleftrightarrow{\Gamma}}(\vec{r},\vec{r}\,';s)\right] ; \left[\tilde{\vec{J}}(\vec{r}\,',s)\right] \right\rangle = \left[\tilde{\vec{I}}(\vec{r},s)\right] \tag{1.20}$$

where the symmetric product (similar to the inner product) between two vectors $\vec{A}(\vec{r},\vec{r}\,')$ and $\vec{B}(\vec{r})$ is defined by

$$\left\langle \vec{A}(\vec{r},\vec{r}\,') ; \vec{B}(\vec{r}) \right\rangle = \iint_S \vec{A}(\vec{r},\vec{r}\,') \cdot \vec{B}(\vec{r}\,')\, dS \tag{1.21}$$

In the expression (1.20), the system Green's function $\tilde{\overleftrightarrow{\Gamma}}(\vec{r},\vec{r}\,';s)$ is given by

$$\left[\tilde{\overleftrightarrow{\Gamma}}(\vec{r},\vec{r}\,';s)\right] = \begin{bmatrix} \tilde{\overleftrightarrow{\Gamma}}_a(\vec{r},\vec{r}_a\,';s) & \tilde{\overleftrightarrow{\Gamma}}_{ac}(\vec{r},\vec{r}_a\,';s) \\ \tilde{\overleftrightarrow{\Gamma}}_{ca}(\vec{r},\vec{r}_c\,';s) & \tilde{\overleftrightarrow{\Gamma}}_c(\vec{r},\vec{r}_c\,';s) \end{bmatrix}$$

where

$\tilde{\overleftrightarrow{\Gamma}}_a(\vec{r},\vec{r}_a\,';s)$: aperture Green's function

$\tilde{\overleftrightarrow{\Gamma}}_{ac}(\vec{r},\vec{r}_a\,';s)$: aperture-scatterer interaction Green's function

$\tilde{\overleftrightarrow{\Gamma}}_{ca}(\vec{r},\vec{r}_c\,';s)$: scatterer-aperture interaction Green's function

$\tilde{\overleftrightarrow{\Gamma}}_c(\vec{r},\vec{r}_c\,';s)$: scatterer Green's function

and the system current density response $\tilde{\vec{J}}(\vec{r}\,',s)$ has two parts corresponding to the response of the aperture $\tilde{\vec{J}}_{s_m}(\vec{r}_a\,',s)$ and that of the conducting scatterer $\tilde{\vec{J}}_s(\vec{r}_c\,',s)$,

$$\tilde{\vec{J}}(\vec{r}\,',s) = \begin{bmatrix} \tilde{\vec{J}}_{s_m}(\vec{r}_a\,',s) \\ \tilde{\vec{J}}_s(\vec{r}_c\,',s) \end{bmatrix} \qquad (1.23)$$

and the right-hand side term $\tilde{\vec{I}}(\vec{r},s)$ in the expression (1.20) represents the forcing function related to the appropriate excitation.

Basically, there is no simple analytical approach to solve the operator integral equation (1.20). One of the most familiar techniques consists in reducing the integral-operator form of the equation to the corresponding matrix-operator form of the equation based on the method of moments.[16] According to this method the unknown response $\tilde{\vec{J}}(\vec{r}\,',s)$ is expanded in terms of N basis or expansion functions,[16]

$$\tilde{\vec{J}}(\vec{r}\,',s) \simeq \sum_{n=1}^{N} \tilde{J}_n(s)\, \vec{F}(\vec{r}\,') \qquad (1.24)$$

giving rise to a numerical response vector, and the equality of the equation on the objects is established by testing the operator integral equation (1.20) by certain weight functions[16] $W_m(\vec{r},s)$, $m = 1,2,\ldots,N$ and forming the inner product (1.21) within the domain of validity of the integral equation. In terms of the method of moments notation, the expression (1.20) reduces to the matrix equation

$$\left[\tilde{\Gamma}_{m,n}(s)\right]\left[\tilde{J}_n(s)\right] = \left[\tilde{I}_m(s)\right] \tag{1.25}$$

where

$\left[\tilde{\Gamma}_{m,n}(s)\right]$: generalized system matrix

$\left[\tilde{J}_n(s)\right]$: generalized response vector

$\left[\tilde{I}_m(s)\right]$: generalized excitation vector

The solution for the current response is obtained by numerically taking the inverse of the system matrix and post-multiplying by the excitation vector,

$$\left[\tilde{J}_n(s)\right] = \left[\tilde{\Gamma}_{m,n}(s)\right]^{-1}\left[\tilde{I}_m(s)\right] \tag{1.26}$$

Hence given a complex frequency of interest $s = \Omega + j\omega$, for given type of excitation, the current response of the aperture and the scatterer is obtained from the expression (1.20).

One of the direct and commonly adopted procedures to obtain the time-domain (transient) response of the scattering objects for a given type of excitation, is to solve the equation (1.26), with $s = j\omega$, for various values of the real-frequency ω corresponding to the specified frequency band of interest, and numerically obtain the inverse transform of the frequency domain data.[2,17] Hence for the time-harmonic case,

$$\left[\tilde{J}_n(j\omega)\right] = \left[\tilde{\Gamma}_{m,n}(j\omega)\right]^{-1}\left[\tilde{I}_m(j\omega)\right] \tag{1.27}$$

and the transient or the time-domain solution is given by

$$\left[J_n(t)\right] = \frac{1}{2\pi}\int_{-\infty}^{+\infty}\left\{\left[\tilde{\Gamma}_{m,n}(j\omega)\right]^{-1}\cdot\left[\tilde{I}_m(j\omega)\right]\right\} e^{j\omega t}\, d\omega \qquad (1.28)$$

and the integration along the ω-axis is appropriately modified if one encounters any singularities either in the matrix inverse operator or in the excitation wave function.

An alternative approach recently developed for transient characterization and time-domain studies is the well-known singularity expansion method.[2,17] This is based on the question of parameterization of the total transient response of an object. In the direct approach, expressions (1.27) and (1.28), the transient study is unavoidably laborious and costly from the amount of data to be processed if the response is to be studied at every point on the structure along with different types of excitation waveforms and polarizations. According to the SEM, it is possible to express the object response in terms of few number of parameters, and once this is done, one can freely study the responses both in the frequency domain and in the time domain.[18-20]

The general formalism of the SEM began with the observations of the responses in the passive lumped circuit theory, and other experimental observations concerning the transient electromagnetic response of complex structures such as aircraft and missiles. It was observed, basically the time-domain response consists of damped sinusoids which correspond to the complex conjugate poles or the singularities in the Laplace complex frequency domain. In general one may encounter other forms of the singularities, such as multiple poles, branch points and branch cuts, essential singularities and even entire functions depending upon specific geometries under consideration. For most of the specific problems discussed in the context of this paper, only the first order pole singularities are important for the finite size conducting objects with the addition of branch cut type of singularities for the infinitely long scattering objects.

Rewriting the matrix operator equation (1.25) for the delta-function response, we have

$$\left[\tilde{\Gamma}_{m,n}(s)\right]\left[\tilde{U}_n(s)\right] = \left[\tilde{I}_m(s)\right] \tag{1.29}$$

Using the singularity expansion,[2] the current response of the object to a delta-function excitation is given by (in the class 2 form),

$$\left[\tilde{U}_n(s)\right] = \sum_\alpha \left\{\beta_\alpha [\tilde{\nu}]_\alpha \cdot [\tilde{\mu}]_\alpha\right\} \frac{\left[\tilde{I}_m(s)\right]}{(s - s_\alpha)} \tag{1.30}$$

where the complex natural frequencies s_α are obtained as the solution to the determinant equation,

$$\det\left[\tilde{\Gamma}_{m,n}(s)\right] = \vec{0} \tag{1.31}$$

the natural mode vector $[\tilde{\nu}]_\alpha$ and the coupling vector $[\tilde{\mu}]_\alpha$ are obtained as the solution to the homogeneous matrix equations,

$$\left[\tilde{\Gamma}_{m,n}(s_\alpha)\right]\left[\tilde{\nu}\right]_\alpha = \vec{0} \tag{1.32}$$

$$\left[\tilde{\Gamma}_{m,n}(s_\alpha)\right]^T\left[\tilde{\mu}\right]_\alpha = \vec{0} \tag{1.33}$$

and the normalization constant β_α is given by

$$\beta_\alpha = \frac{1}{[\tilde{\mu}]_\alpha^T \cdot \left\{\frac{d}{ds}\left[\tilde{\Gamma}_{m,n}(s_\alpha)\right]\right\} \cdot [\tilde{\nu}]_\alpha} \tag{1.34}$$

Such a representation results in a compact form of the object response. For calculating the transient response, the Laplace inverse transform definition (1.12) is used by appropriately closing the Bromowich contour, figure 1.5, either to the right half or to the left half of the complex s plane. In the expression

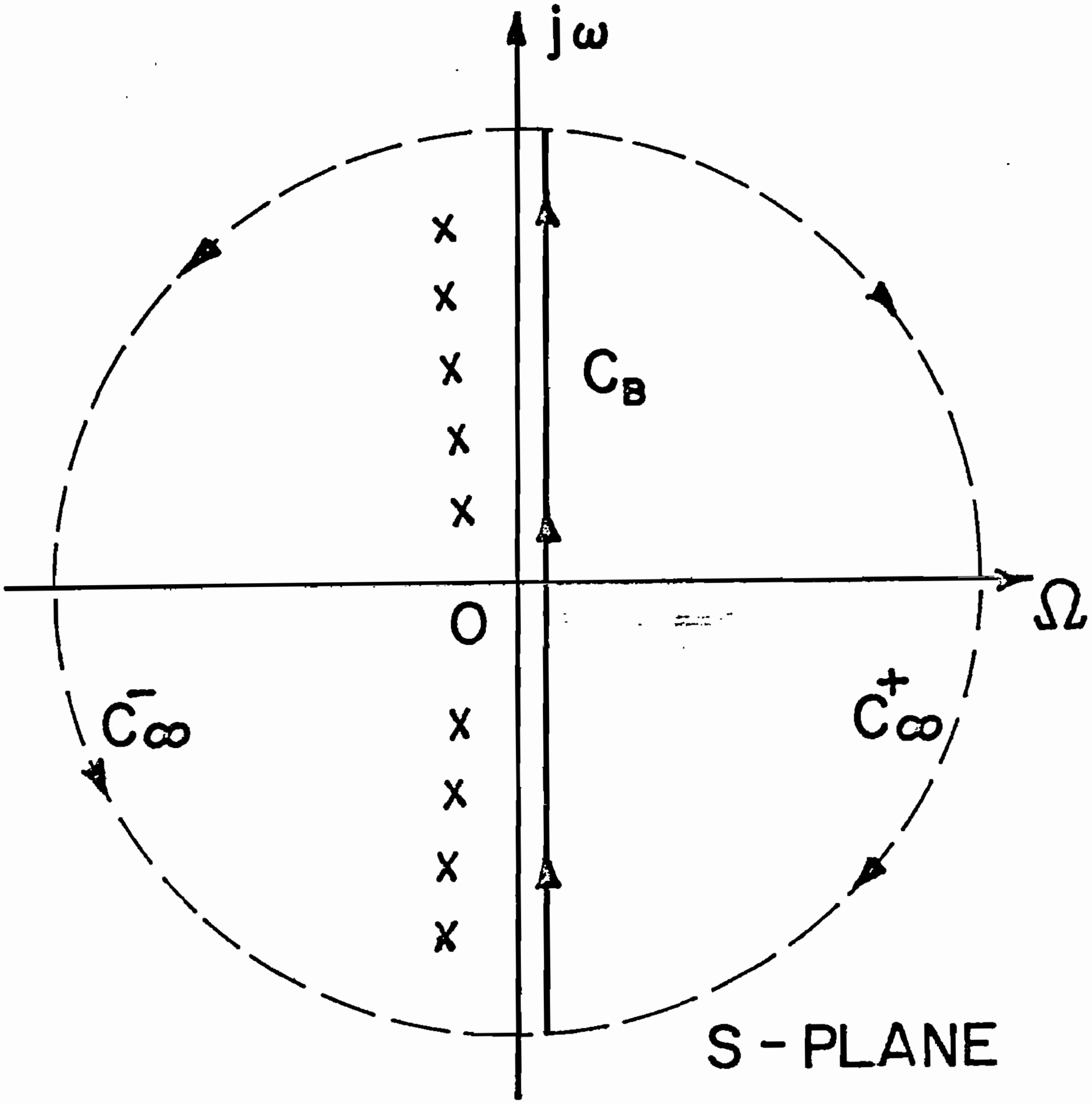

Figure 1.5 Illustration of the Closure of the Bromwich Contour in s-Plane

(1.30), the term $[\tilde{I}_m(s)]$ contains the incident excitation and it is to be modified if one wishes to incorporate other types of transient waveforms or convolute with the delta function response. Hence, we have the time domain solution,

$$\left[\tilde{U}_n(t)\right] = \sum_{\alpha} \tilde{\eta}_\alpha [\tilde{\nu}]_\alpha \, e^{s_\alpha t} \, u(t) \tag{1.35}$$

where $\tilde{\eta}_\alpha$ is the coupling coefficient defining the magnitude of the excitation coupling to a particular mode and u(t) being a unit step function.[2]

CHAPTER II

Integral Equations for the Various Aperture and Slot Geometries

The aperture-scatterer integral equations (1.15) and (1.16) reduce to a comparatively simple form for the case of diffraction by only an aperture in the planer conducting screen with no bodies placed behind it. In figure 2.1, if the conducting scatterer is removed, then the expression (1.15) becomes,

$$\frac{s}{\gamma_-^2}\left[\nabla\left(\nabla\cdot\vec{\tilde{A}}_{m_-}(\vec{r},s)\right)-\gamma_-^2\vec{\tilde{A}}_{m_-}(\vec{r},s)\right]\times\vec{1}_z$$

$$+\frac{s}{\gamma_+^2}\left[\nabla\left(\nabla\cdot\vec{\tilde{A}}_{m_+}(\vec{r},s)\right)-\gamma_+^2\vec{\tilde{A}}_{m_+}(\vec{r},s)\right]\times\vec{1}_z$$

$$=-\vec{\tilde{H}}_{sc_-}(\vec{r},s)\times\vec{1}_z \qquad (2.1)$$

$$\vec{r}\in \text{aperture } S_a$$

and if both medium 1 and 2 separated by the screen have the same medium characteristics (μ, ε, σ), then the expression (2.1) further simplifies to

$$\left[\nabla\left(\nabla\cdot\vec{\tilde{A}}_{m}(\vec{r},s)\right)-\gamma^2\vec{\tilde{A}}_{m}(\vec{r},s)\right]\times\vec{1}_z=-\frac{\gamma^2}{s}\vec{\tilde{H}}^i(\vec{r},s)\times\vec{1}_z \qquad (2.2)$$

$$\vec{r}\in \text{aperture } S_a$$

A. Rectangular Aperture

For the case of rectangular apertures, the electric vector potential $\vec{\tilde{A}}_m$ can be resolved into its rectangular components,

$$\vec{\tilde{A}}_m(\vec{r},s)=\vec{1}_x\tilde{A}_{m_x}(\vec{r},s)+\vec{1}_y\tilde{A}_{m_y}(\vec{r},s) \qquad (2.3)$$

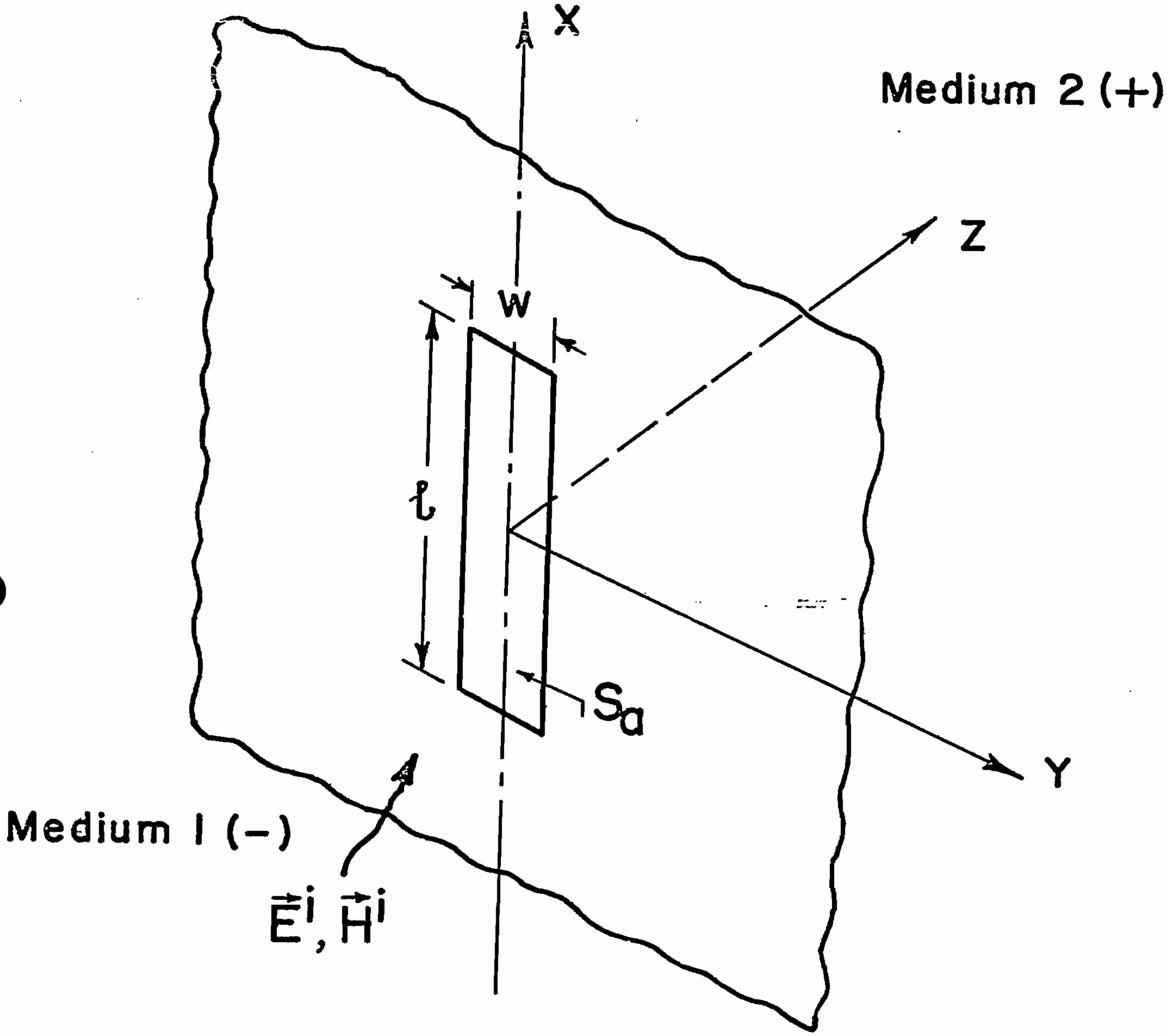

Figure 2.1 Narrow Slot in a Conducting Screen

and substituting (2.3) into the expression (2.2) yields the following coupled integro-differential equations,

$$\left(\frac{\partial^2}{\partial x^2} - \gamma^2\right)\tilde{A}_{m_x}(\vec{r},s) + \frac{\partial^2}{\partial x\partial y}\tilde{A}_{m_y}(\vec{r},s) = -\frac{\gamma^2}{s}\tilde{H}_x^i(\vec{r},s) \tag{2.4}$$

$$\left(\frac{\partial^2}{\partial y^2} - \gamma^2\right)\tilde{A}_{m_y}(\vec{r},s) + \frac{\partial^2}{\partial x\partial y}\tilde{A}_{m_x}(\vec{r},s) = -\frac{\gamma^2}{s}\tilde{H}_y^i(\vec{r},s) \tag{2.5}$$

$$\vec{r} \in S_a$$

and from the expressions (1.5), (1.6), and (1.7),

$$\tilde{A}_{m_{\substack{x\\y}}}(\vec{r},s) = \frac{(\sigma + s\varepsilon)}{2\pi s}\iint_{S_a}\tilde{J}_{s_{m_{\substack{x\\y}}}}(\vec{r}_a{}',s)\,\tilde{G}(\vec{r},\vec{r}_a{}';s)\,dx_a'dy_a' \tag{2.6}$$

$$\tilde{G}(\vec{r},\vec{r}_a{}';s) = \frac{e^{-\gamma|\vec{r} - \vec{r}_a{}'|}}{|\vec{r} - \vec{r}_a{}'|} \tag{2.7}$$

$$|\vec{r} - \vec{r}_a{}'| = \left[(x - x_a')^2 + (y - y_a')^2\right]^{\frac{1}{2}} \tag{2.8}$$

B. Narrow Slot

The geometry of the narrow slot is shown in figure 2.1, where the ratio of width to length $w/\ell << 1$. For the analysis of diffraction by narrow rectangular slots the component of the electric vector potential $\tilde{A}_{m_x}(\vec{r},s)$ in the slot axial direction is predominant and the cross component $\tilde{A}_{m_y}(\vec{r},s)$ for all practical purposes can be neglected, so that the general integral equation for the narrow slot has the form,

$$\frac{s}{\gamma_-^2}\left(\frac{\partial^2}{\partial x^2} - \gamma_-^2\right)\tilde{A}_{m_{x_-}}(\vec{r},s) + \frac{s}{\gamma_+^2}\left(\frac{\partial^2}{\partial x^2} - \gamma_+^2\right)\tilde{A}_{m_{x_+}}(\vec{r},s) = -2\tilde{H}_x^i(\vec{r},s) \tag{2.9}$$

$$\vec{r} \text{ in slot}$$

and further specializing the expression (2.9), for the case of same medium characteristics (μ, ε, σ) on both sides, the integral equation (2.9) becomes,

$$\left(\frac{\partial^2}{\partial x^2} - \gamma^2\right) \tilde{A}_{m_x}(\vec{r},s) = -\frac{\gamma^2}{s}\tilde{H}_x^i(\vec{r},s) \qquad \vec{r} \in \text{in slot} \tag{2.10}$$

where

$$\tilde{A}_{m_x}(\vec{r},s) = \frac{(\sigma + s\varepsilon)}{2\pi s}\iint_{S_a} \tilde{J}_{s_{m_x}}(\vec{r}_a\,',s)\,\tilde{G}(\vec{r},\vec{r}_a\,';s)\,dx_a'dy_a' \tag{2.11}$$

The magnetic current distribution $J_{s_{m_x}}(\vec{r}_a\,',s)$ for a narrow slot can be written in terms of the axial distribution $m(x)$ and the transverse distribution $\zeta(y)$ which has the right type of singular distribution at the edges,[21]

$$J_{s_{m_x}}(x,y) = m(x)\,\zeta(y) \tag{2.12}$$

where

$$\zeta(y) = \frac{1}{\pi}\left[\left(\frac{w}{2}\right)^2 - y^2\right]^{-\frac{1}{2}} \tag{2.13}$$

Substituting the narrow slot distribution (2.12) into the expression (2.11), we have for a narrow rectangular slot, the integro-differential equation,

$$\left(\frac{\partial^2}{\partial x^2} - \gamma^2\right) \tilde{A}_{m_x}(x,s) = -\frac{\gamma^2}{s}\tilde{H}_x^i(x,s)\,, \qquad -\frac{\ell}{2} < x < \frac{\ell}{2} \tag{2.14}$$

where

$$\tilde{A}_{m_x}(x,s) = \frac{(\sigma + s\varepsilon)}{2\pi s} \int_{-\ell/2}^{\ell/2} m(x_a') \, \tilde{G}^{NS}(x,x_a';s) \, dx_a' \tag{2.15}$$

$$\tilde{G}^{NS}(x,x_a';s) = \frac{e^{-\gamma R_a}}{R_a} \tag{2.16}$$

$$R_a = \left[(x - x_a')^2 + (\tfrac{w}{4})^2\right]^{\frac{1}{2}} \tag{2.17}$$

A point to note at this stage, is the duality[15,22] of the problem. In fact the expressions (2.4) and (2.5) are the dual equations of a rectangular plate,[13,23] while the expression (2.10) is the dual equation of a narrow strip scattering problem.

C. Narrow Multiple Slots

The case of diffraction by narrow finite multiple slots, figure 2.2, in a conducting screen can still be analyzed based on the integral equation (2.10) since all the slots considered form an array and are oriented parallel. But the electric vector potential $\tilde{A}_{m_x}$ in the expression (2.10) should be redefined to take into account the mutual interaction between the adjacent slots. Hence, the integral equation for narrow finite multiple slots is given by the integral equation (2.10) with $\tilde{A}_{m_x}$ replaced by the total electric vector potential $\tilde{A}^N_{m_x}$ due to N slots,

$$\tilde{A}^N_{m_x}(\vec{r},s) = \frac{(\sigma + s\varepsilon)}{2\pi s} \sum_{n=1}^{N} \iint_{S_a^n} \tilde{J}^n_{s_{m_x}}(\vec{r}\,'_{a_n},s) \, \tilde{G}(\vec{r},\vec{r}\,'_{a_n};s) \, dx'_{a_n} dy'_{a_n} \tag{2.18}$$

where $\tilde{J}^n_{sm_x}$ is the magnetic current distribution in the nth slot and the Green's function

$$\tilde{G}(\vec{r},\vec{r}\,'_{a_n};s) = \frac{e^{-\gamma|\vec{r} - \vec{r}\,'_{a_n}|}}{|\vec{r} - \vec{r}\,'_{a_n}|} \tag{2.19}$$

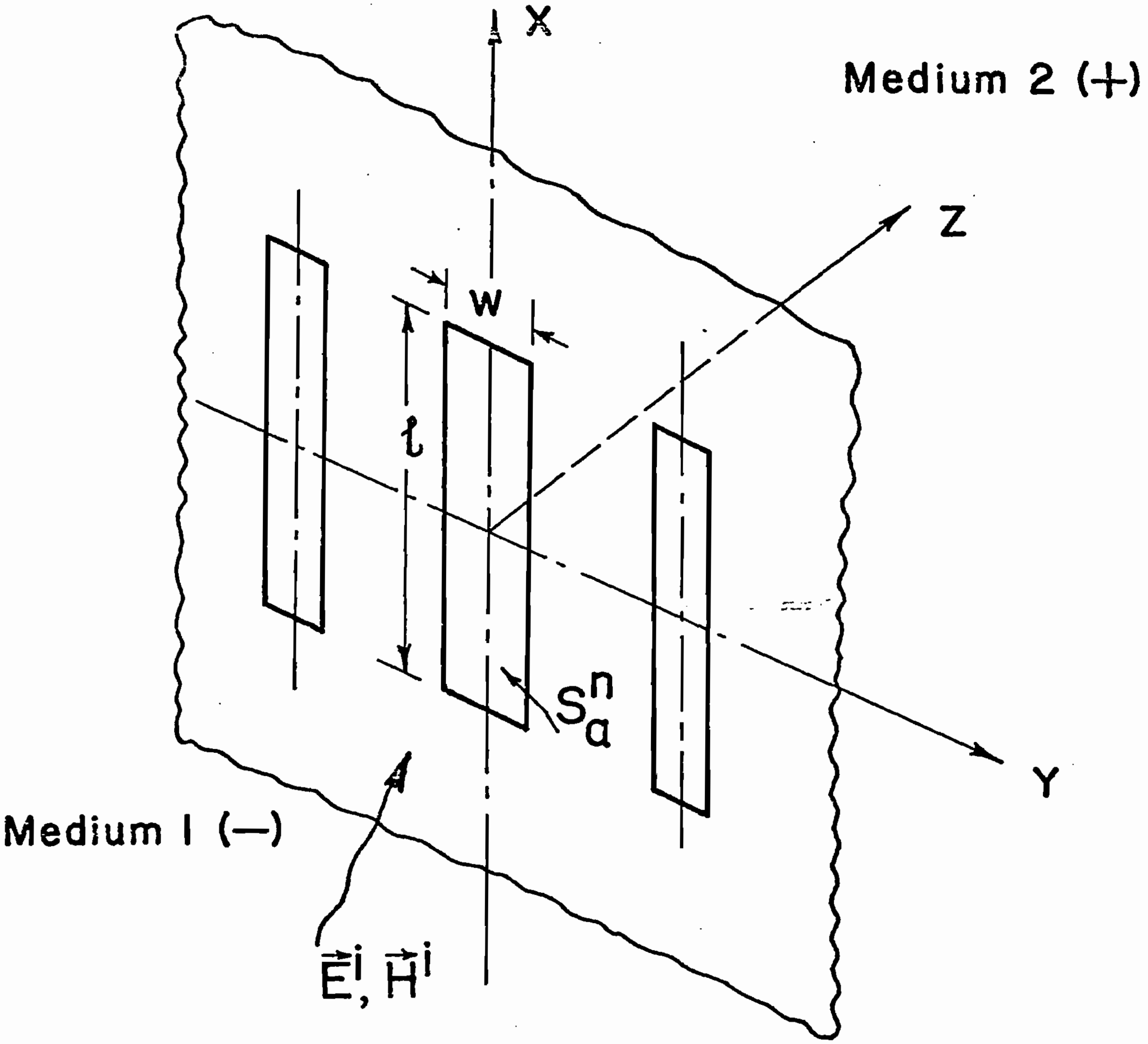

Figure 2.2 Multiple Narrow Slots in a Conducting Screen

$$|\vec{r} - \vec{r}'_{a_n}| = \left[(x - x'_{a_n})^2 + (y - y'_{a_n})^2\right]^{\frac{1}{2}} \qquad (2.20)$$

D. Infinitely Long Slots: TE and TM

In figure 2.3 is shown an infinitely long slot in a conducting screen for two different polarizations of the incident magnetic field. In the TE case, the incident magnetic field has only a y-component having the electric field transverse to the axis of the slot and both the fields being independent of the y-coordinate variable; while in the TM case, the incident electric field has only a y-component (negative) having the magnetic field transverse to the axis of the slot, again both the fields being independent of y-variable. The analysis of the infinitely long slot in a conducting screen for these two specialized, TE and TM, polarizations of the incident field is very important since the integral equations encountered, are in simple one-dimensional form; also the field distributions obtained in the two cases explain and give more insight into the more general case of diffraction by rectangular apertures in a conducting screen.

(i) TE case:

In case of TE analysis[14] of an infinitely long slot in a conducting screen, the electric field is x-directed, and transverse to the slot axis, and is independent of y-coordinate variable. Thus, we have only a y-component of the magnetic current distribution,

$$\tilde{\vec{J}}_{s_m}(\vec{r},s) = \vec{1}_y \tilde{J}_{s_{m_y}}(x,s) \qquad (2.21)$$

According to the expression (2.1), figure 2.4,

$$s\left[\tilde{A}_{m_{y_-}}(x,s) + \tilde{A}_{m_{y_+}}(x,s)\right] = 2\tilde{H}^i_y(x,s) \qquad (2.22)$$

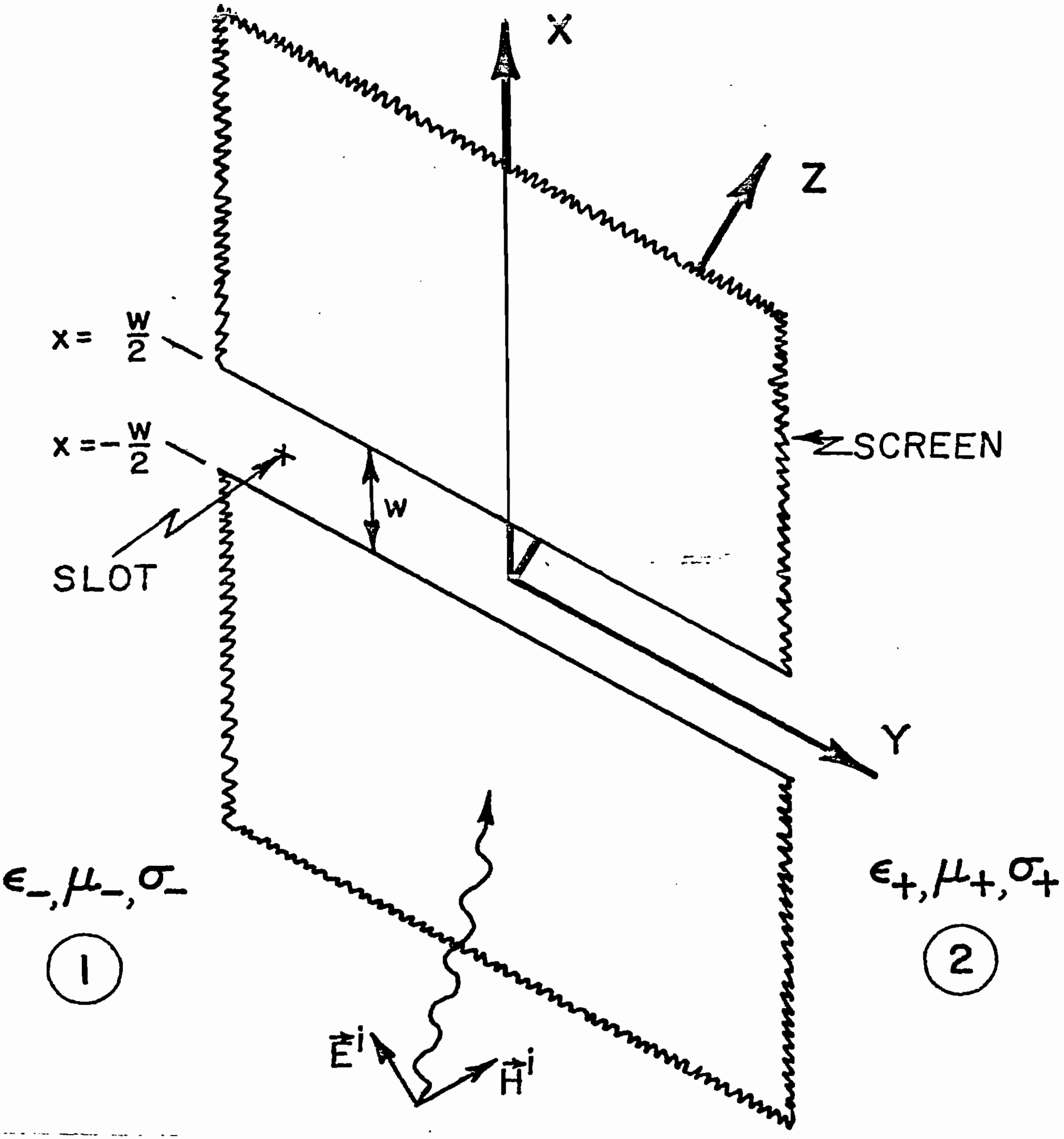

Figure 2.3 Infinite Slot in a Conducting Screen

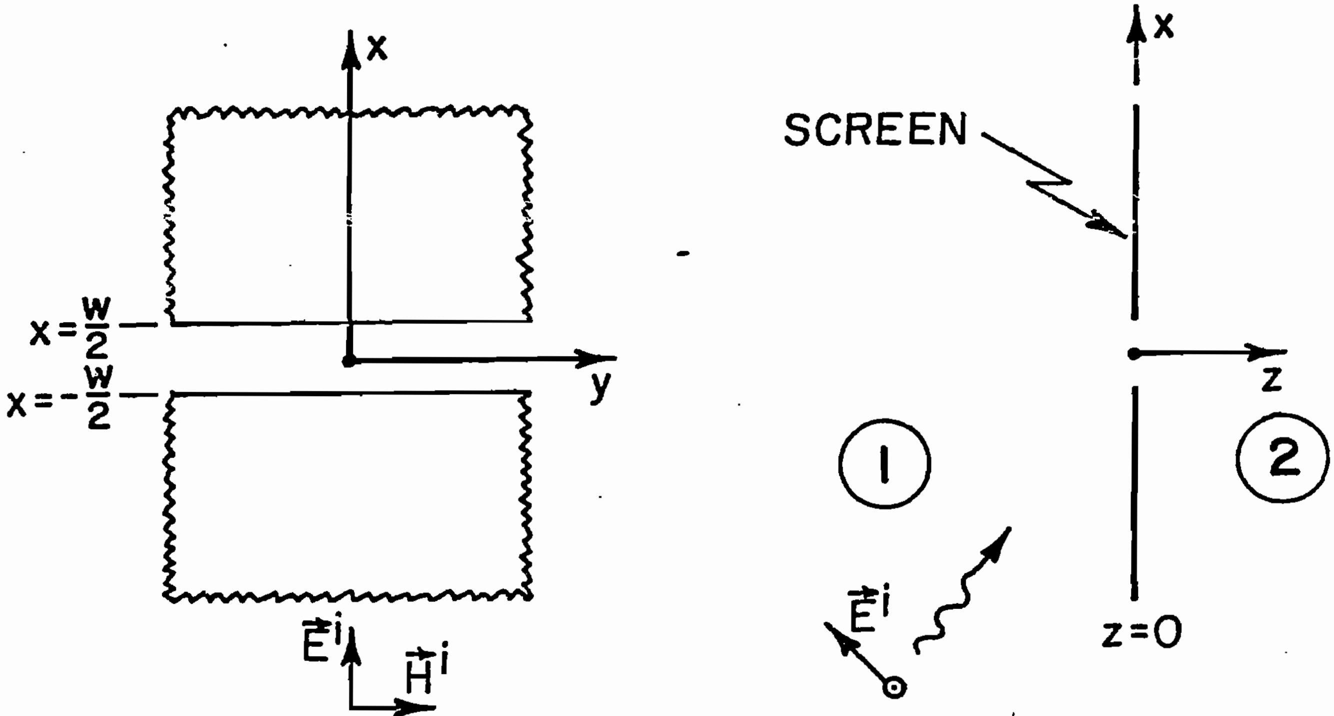

Figure 2.4 TE Excited Infinite Slot

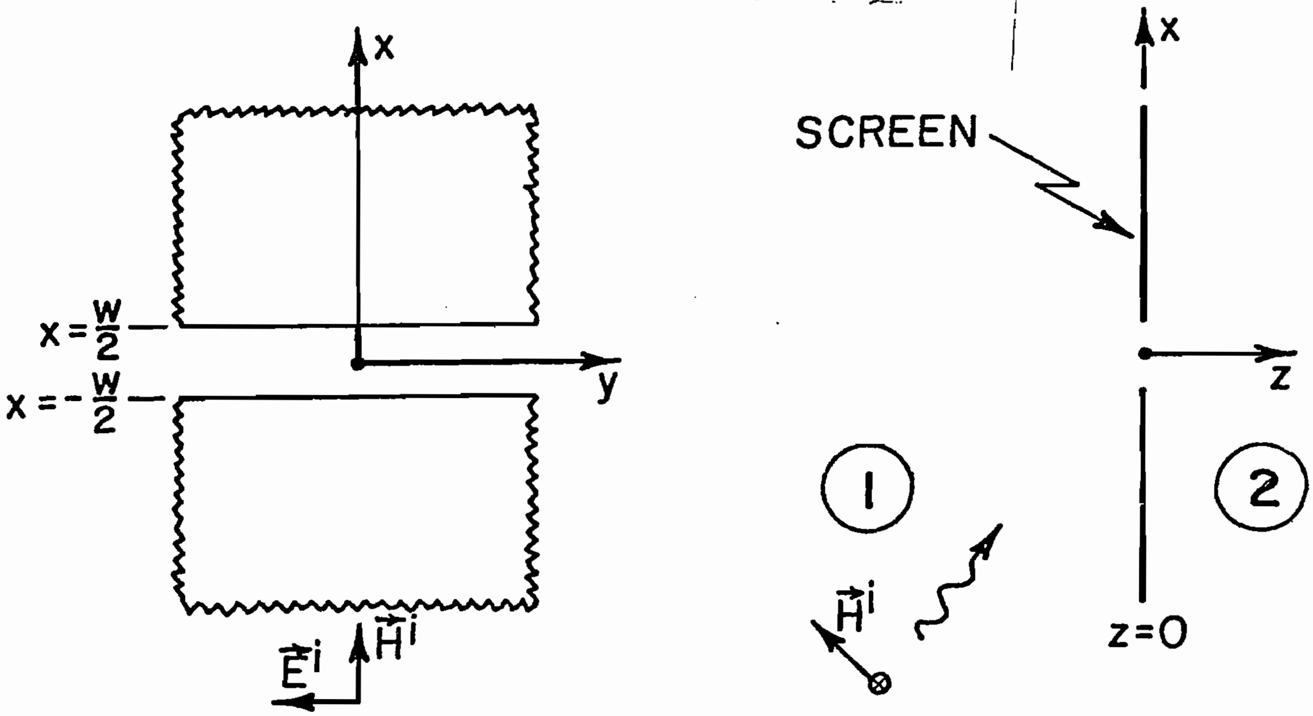

Figure 2.5 TM Excited Infinite Slot

and since $\tilde{A}_{my_-}$ and $\tilde{A}_{my_+}$ are independent of y, selecting y = 0 in the expression (1.5), we have

$$\tilde{A}_{m_{y_\pm}}(x,s) = \frac{(\sigma_\pm + s\varepsilon_\pm)}{2\pi s} \iint_{SLOT} \tilde{J}_{s_{m_y}}(\vec{r}_a\,',s)\, \tilde{G}_\pm(\vec{r},\vec{r}_a\,';s)\, dx_a'dy_a'$$

$$= \frac{(\sigma_\pm + s\varepsilon_\pm)}{j2s} \int_{x_a'=-\frac{w}{2}}^{\frac{w}{2}} \tilde{J}_{s_{m_y}}(x_a',s)\, H_0^{(2)}[-j\gamma_\pm|x-x_a'|]\,dx_a' \tag{2.23}$$

where $H_0^{(2)}$ is the Hankel function of the second kind and zero order. If both sides of the media are having the same medium characteristics (μ, ε, σ), the expressions (2.22) and (2.23) yield

$$\int_{x_a'=-\frac{w}{2}}^{\frac{w}{2}} \tilde{J}_{s_{m_y}}(x_a',s) H_0^{(2)}[-j\gamma|x-x_a'|]\,dx_a' = \frac{j2}{(\sigma + s\varepsilon)}\,\tilde{H}_y^i(x,s) \tag{2.24}$$

$$-\frac{w}{2} < x < \frac{w}{2}$$

(ii) TM case:

A similar analysis is followed for TM excitation[14] of the infinitely long slot in a conducting screen, the electric field in the slot is y-directed and independent of y-coordinate variable. We have only an x-component of the magnetic current distribution,

$$\tilde{\vec{J}}_{s_m}(\vec{r},s) = \vec{1}_x\, \tilde{J}_{s_{m_x}}(x,s) \tag{2.25}$$

According to the expression (2.1), figure 2.5,

$$\frac{s}{\gamma_-^2}\left[\frac{\partial^2}{\partial x^2} - \gamma_-^2\right]\tilde{A}_{m_{x_-}}(x,s) + \frac{s}{\gamma_+^2}\left[\frac{\partial^2}{\partial x^2} - \gamma_+^2\right]\tilde{A}_{m_{x_+}}(x,s) = -2\tilde{H}_x^i(x,s) \tag{2.26}$$

and further $\tilde{A}_{m_{x_-}}$ and $\tilde{A}_{m_{x_+}}$ are independent of the y-coordinate variable, selecting $y = 0$, we have from the expression (1.5),

$$\tilde{A}_{m_{x_\pm}}(x,s) = \frac{(\sigma_\pm + s\varepsilon_\pm)}{j2s} \int_{x_a'=-\frac{w}{2}}^{\frac{w}{2}} \tilde{J}_{s_{m_x}}(x_a',s) H_0^{(2)}[-j\gamma_\pm |x-x_a'|]\, dx_a' \tag{2.27}$$

Again, for the special case of same medium characteristics (μ, ε, σ), we have the integral equation,

$$\left[\frac{\partial^2}{\partial x^2} - \gamma^2\right] \int_{x_a'=-\frac{w}{2}}^{\frac{w}{2}} \tilde{J}_{s_{m_x}}(x_a',s) H_0^{(2)}[-j\gamma |x-x_a'|]\, dx_a' = -j2s\mu\, \tilde{H}_x^i(x,s) \tag{2.28}$$

$$-\frac{w}{2} < x < \frac{w}{2}$$

It is quite academic at this point to look at the duality of the equations (2.24) and (2.28). In fact, one obtains similar equations for an infinitely long strip scatterer, the equation (2.24) for a TM strip and the equation (2.28) for a TE excited strip in a homogeneous medium.

E. Numerical Results

A few of the canonical types of aperture shapes were discussed in the previous sections and the pertinent integral equations were derived in terms of the unknown aperture magnetic current distribution. Once these distributions are determined for a given type of incident excitation, the complete fields both in the illuminated and the shadow region can be determined using the field expressions (1.1) to (1.4). One of the powerful techniques available to obtain the solution of the integral equations is based on the method of moments.[16] This involves the process of converting the operator type equations to the corresponding matrix type equations, which can further be analyzed numerically.[23]

In figures 2.6 to 2.9, numerical results[14] are presented for the case of an infinitely long slot, based on the integral expressions (2.22) and (2.26), in which the slot is in a conducting screen, figures 2.4 and 2.5, separating two half-spaces of different electrical properties. Figures 2.6 and 2.7 give the slot distribution for the TE excitation and figures 2.8 and 2.9 for the TM excitation. The left side (-) medium is assumed to be free space in which a plane wave propagates and illuminates the infinite slot. The figures depict both the real and imaginary parts of the slot magnetic current distribution as a function of the permittivity ε_+ figures 2.6 and 2.8, and as a function of the conductivity σ_+ figures 2.7 and 2.9. The TE slot distribution has the right type of singular behavior at the edges, while in the TM distribution it goes to zero at the edges. These results are quite valuable to understand what happens for the distribution in the case of a finite rectangular slot or aperture. Based on these solutions, the fields scattered can be calculated. In figure 2.10 is shown the far-field magnetic-field variation due to the TE excited slot and in figure 2.11 is shown the far-field electric-field distribution due to the TM excitation of the slot as a function of right half-space permittivities. The results of the far-field do exhibit wavelength contraction as the permittivity is increased.

The solution of the coupled integral equations (2.4) and (2.5) for a rectangular aperture is more involved from the numerical point of view.[9,10,13] For electrically very small apertures, the solution procedure[9] based on Rayleigh series can be conveniently employed so that the zero-order and first-order solutions represent to a fair degree of accuracy the distribution in small apertures. In figure 2.12 is shown the $J_{sm_x}(x,y)$ component of the magnetic current distribution in a small square aperture for a normal plane wave excitation. Similarly in figure 2.13 is shown the distribution of the $J_{sm_x}(x,y)$ component in a narrow rectangular aperture in the presence of a conducting ground plane

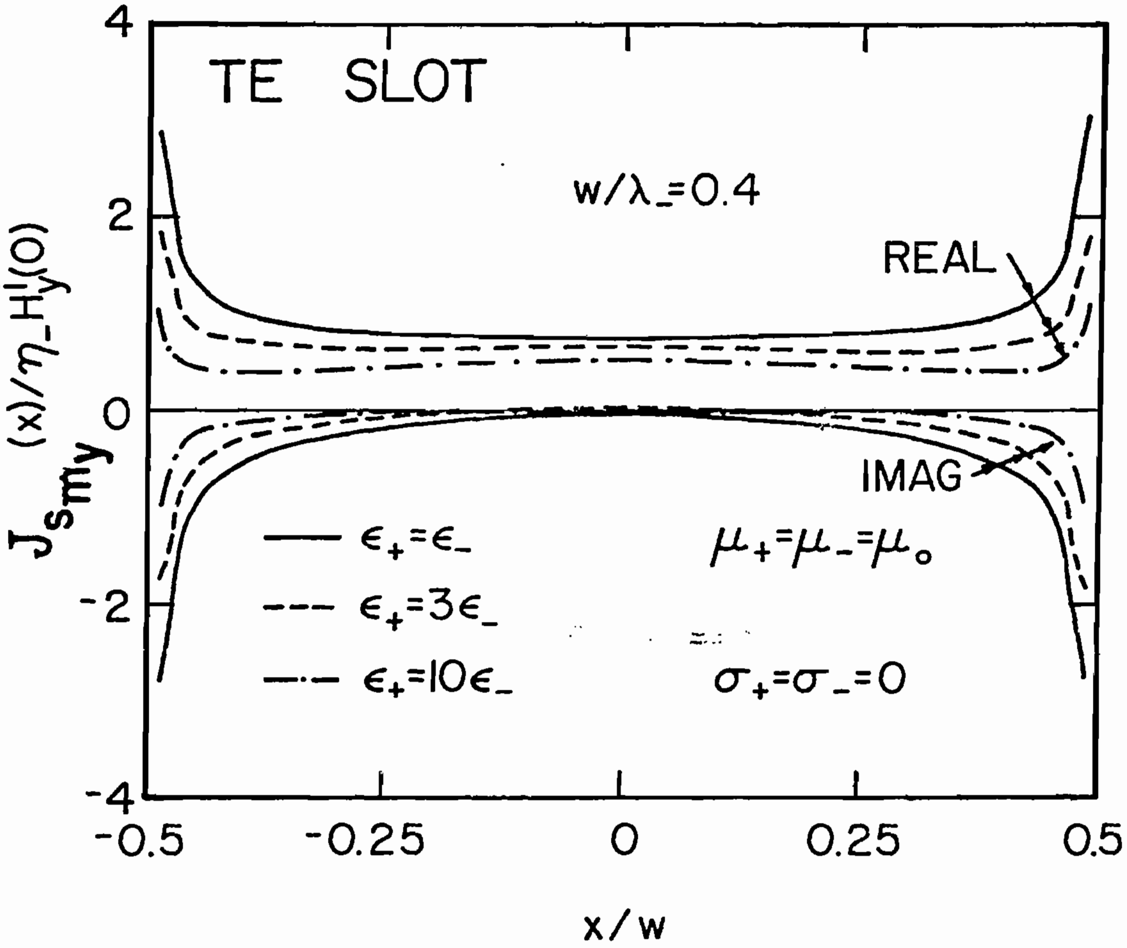

Figure 2.6 TE Magnetic Current in 0.4-Wavelength Slot for Different ε_+

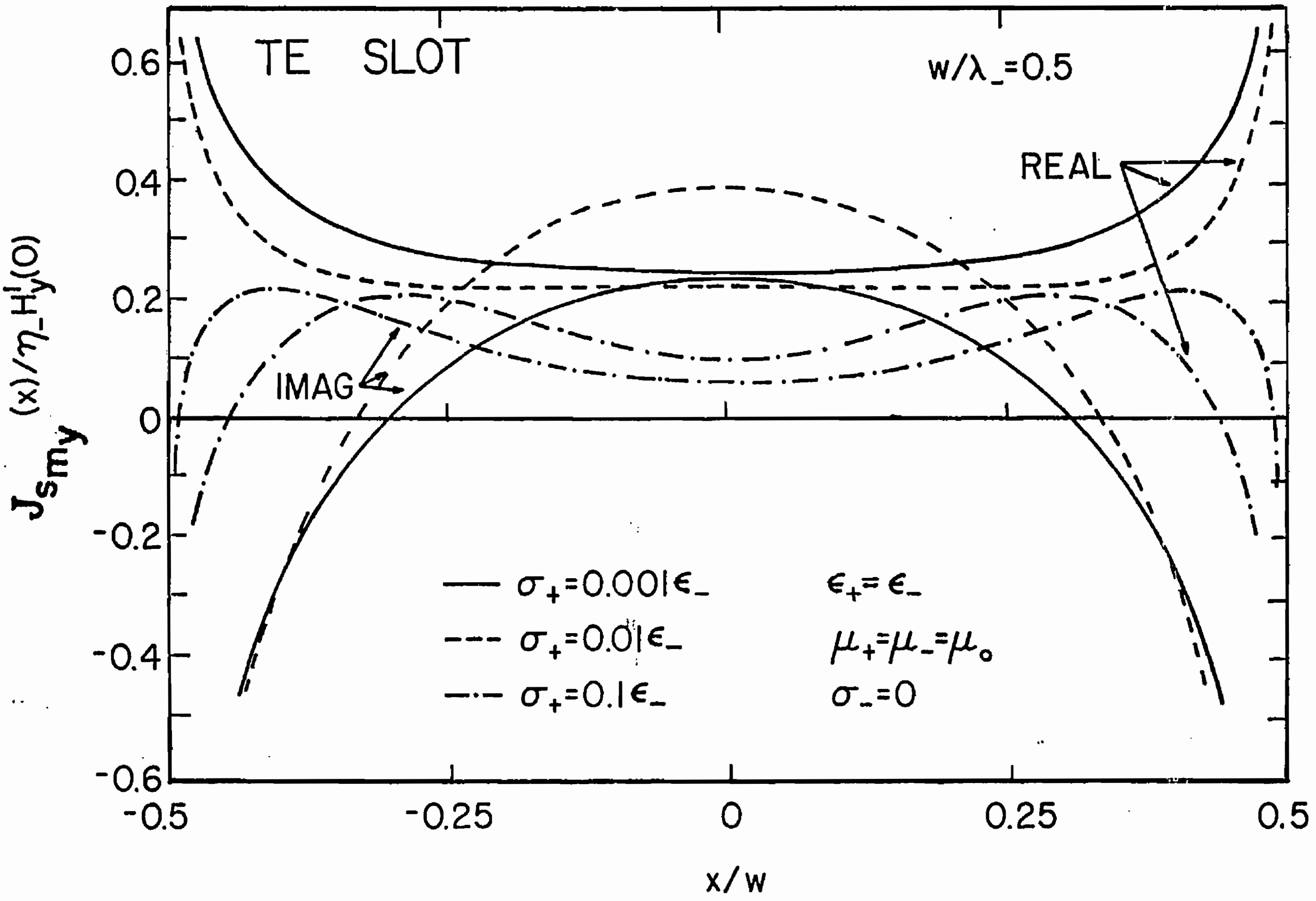

Figure 2.7 TE Magnetic Current in 0.5-Wavelength Slot for Different σ_+

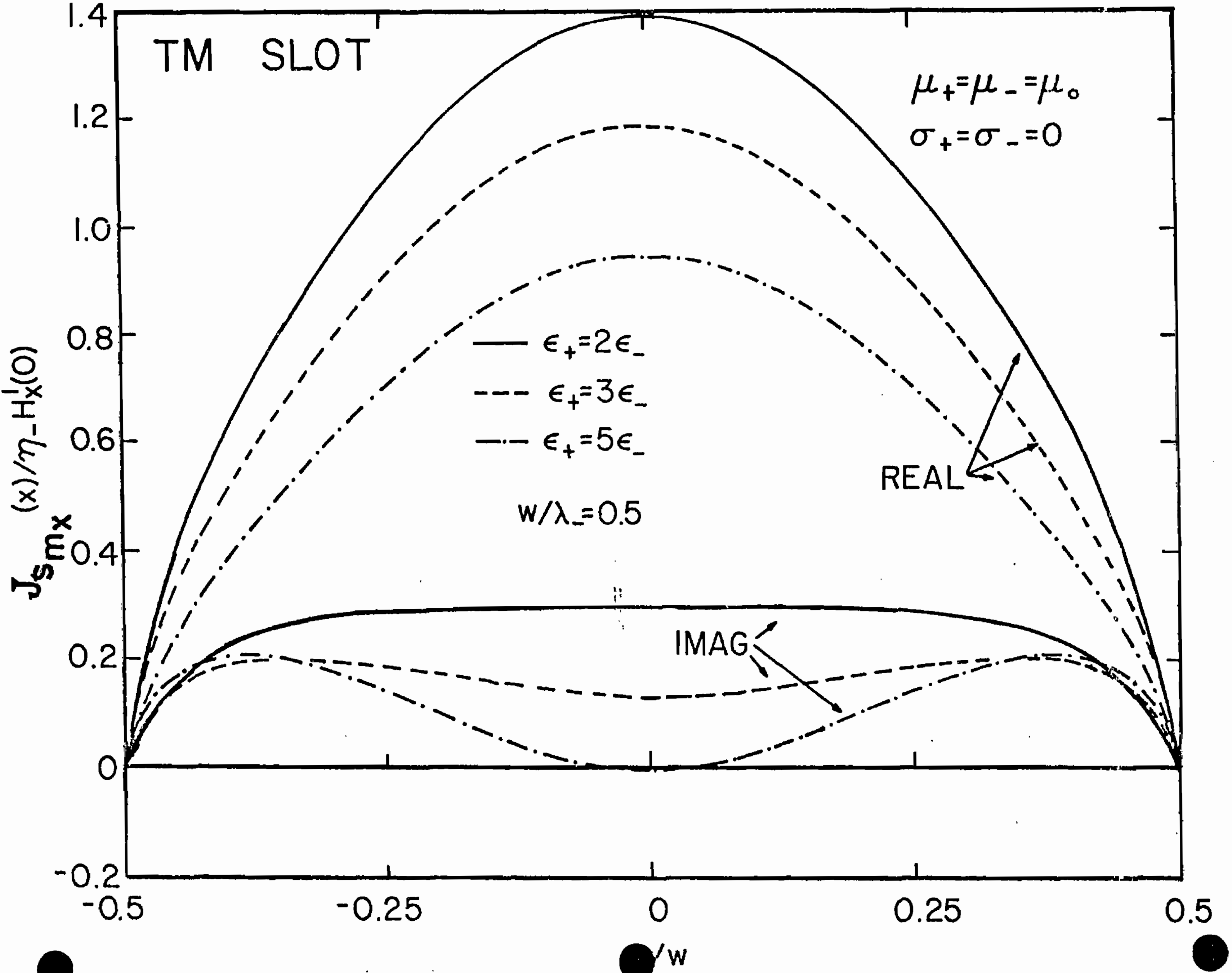

Figure 2.8 T Magnetic Curre 0.5-Wavelength Slot for

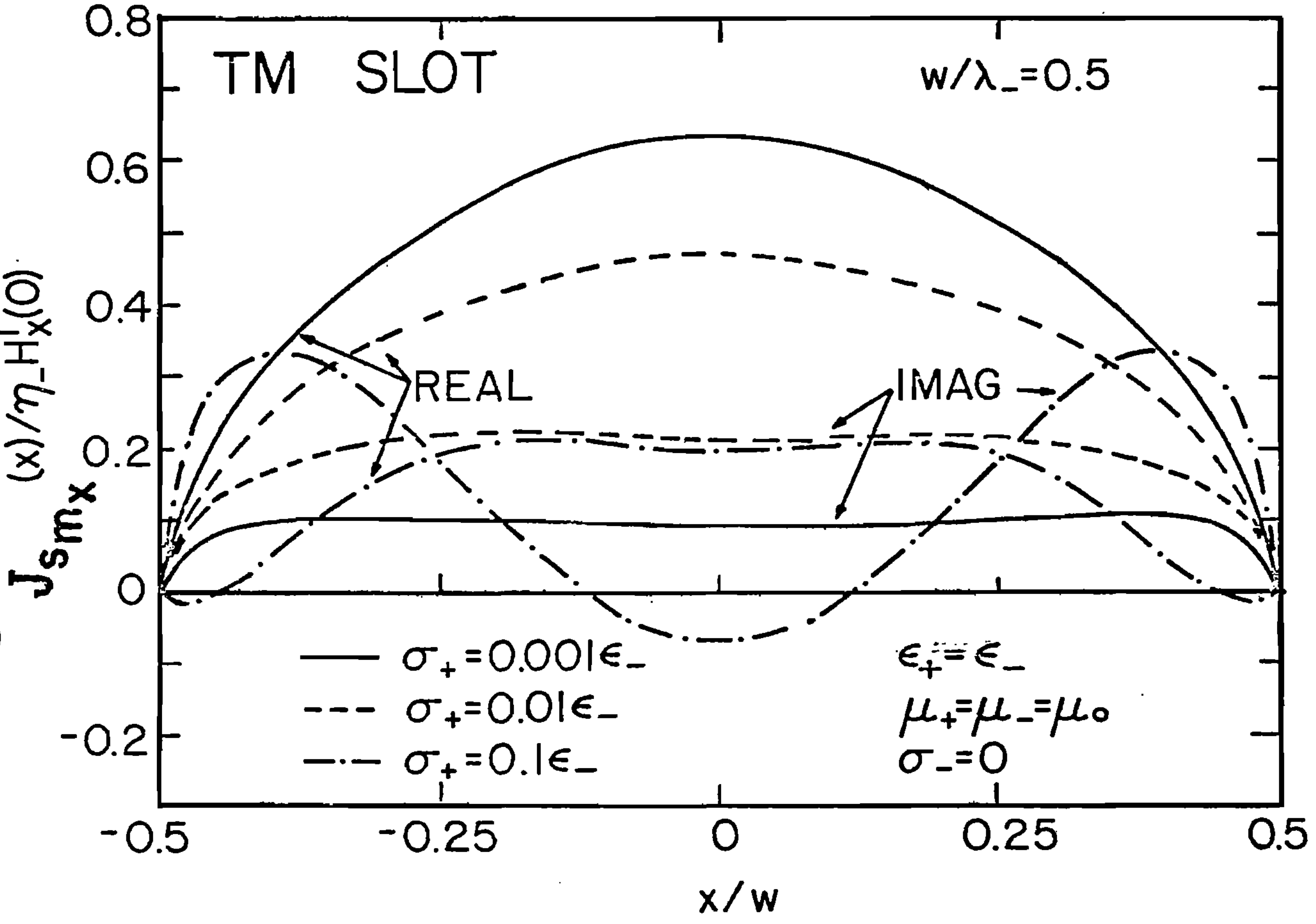

Figure 2.9 TM Magnetic Current in 0.5-Wavelength Slot for Different σ_+

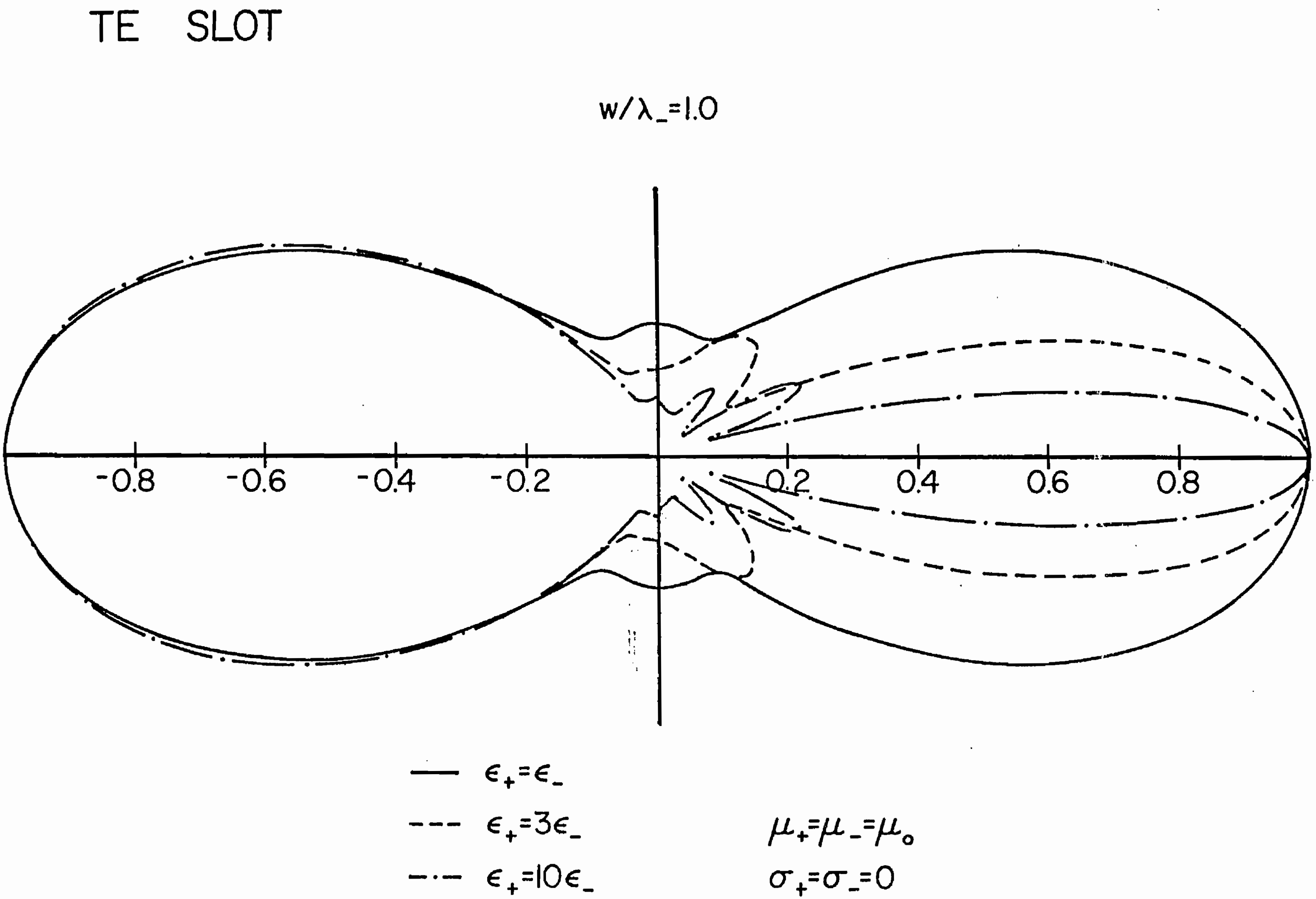

Figure 2.10 Far Magnetic Field of TE Excited Slot for Different ε_+

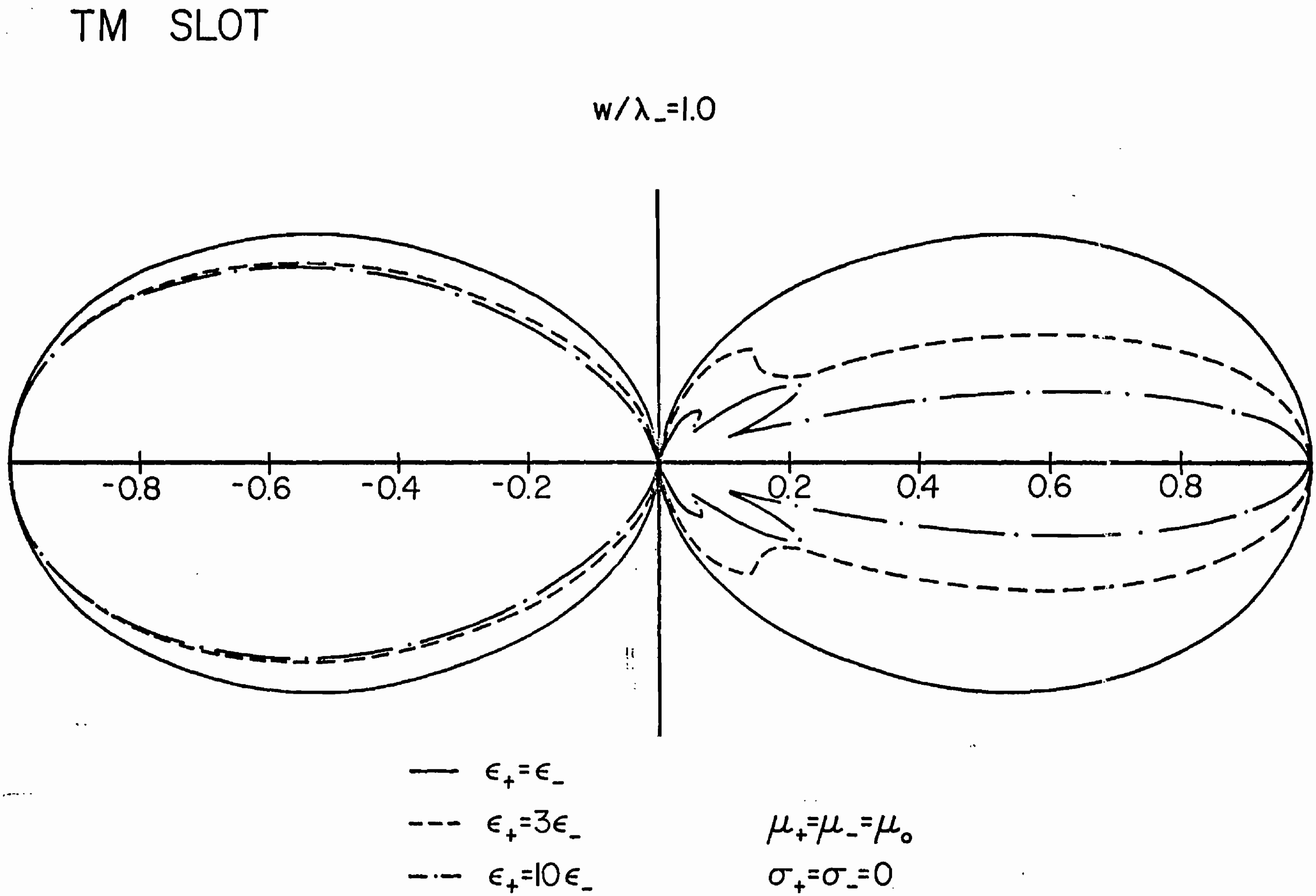

Figure 2.11 Far Electric Field of TM Excited Slot for Different ϵ_+

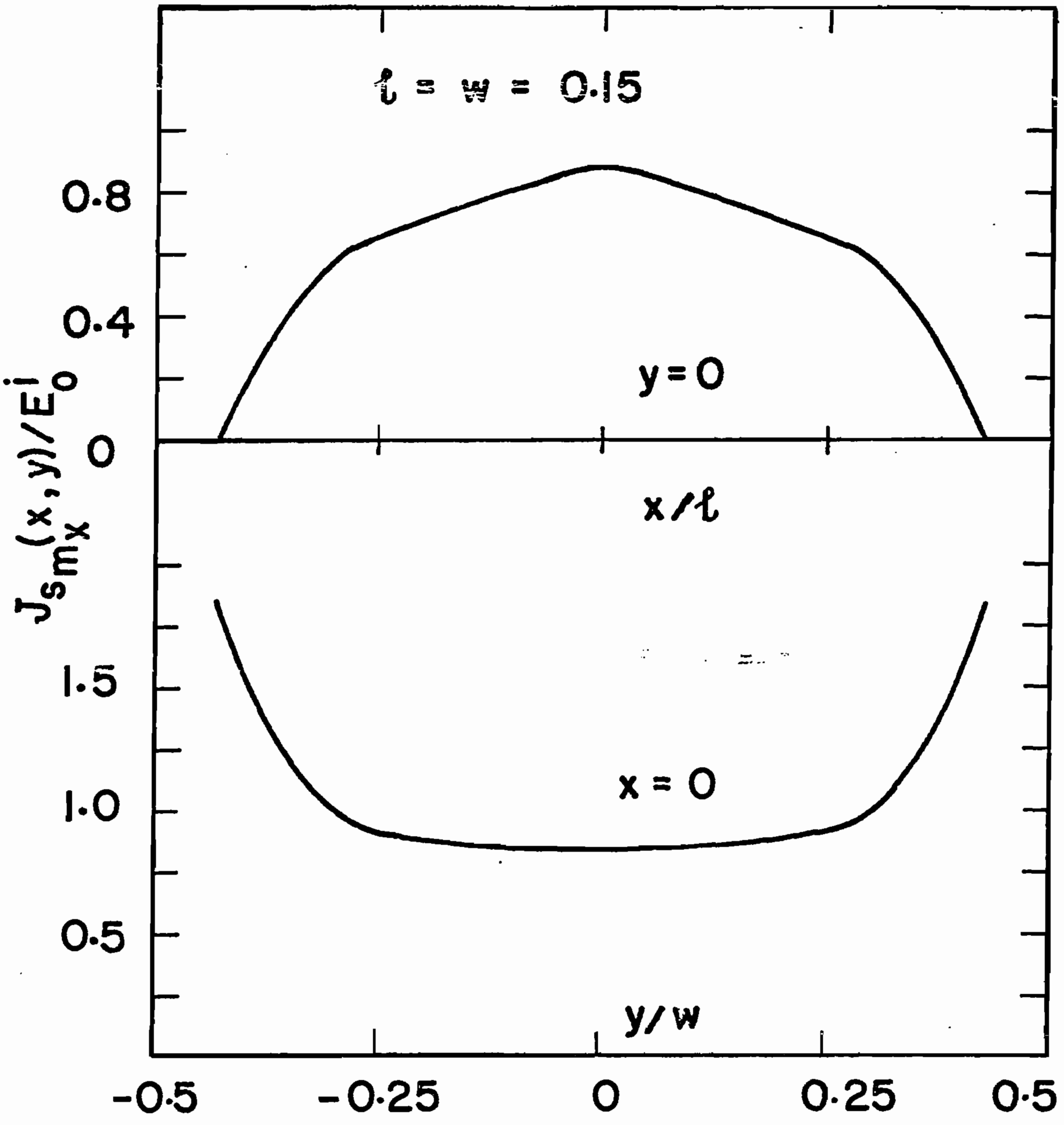

Figure 2.12 Magnetic Current Distribution in a Square Aperture

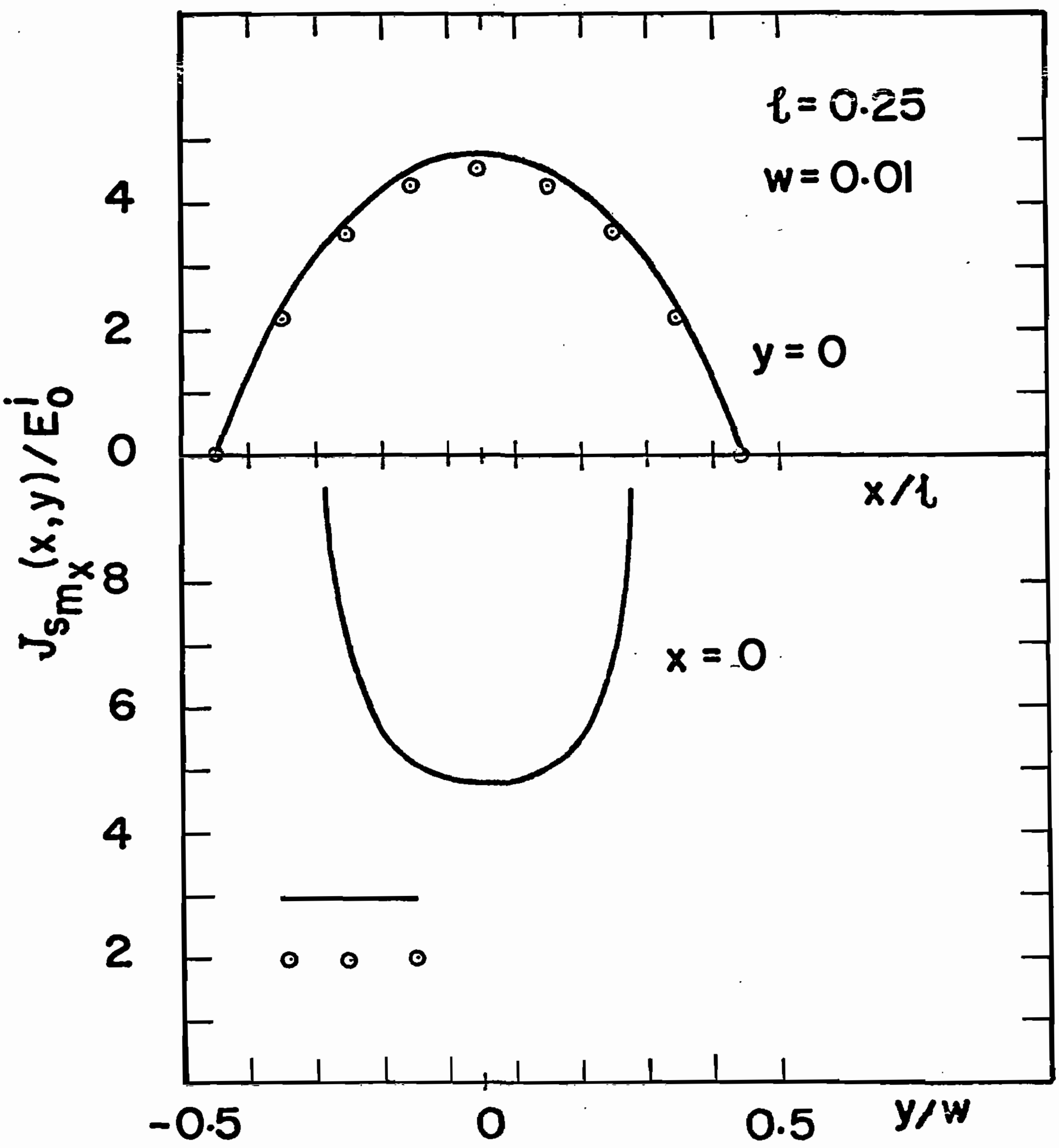

Figure 2.13 Magnetic Current Distribution in a Narrow Rectangular Slot

for normal plane wave excitation. These distributions are completely altered if a scatterer is coupled to the aperture depending on its location and orientation.

F. Aperture Dipole Moments and Penetrated Fields

In the previous sections some examples of different aperture shapes are discussed based on the integral equation formulations. The results presented are numerically oriented. If one is interested with electrically very small apertures, as is the case with many of the EMP type interaction problems, the effect of the aperture and its corresponding magnetic current distributions can be approximated in the quasi-static frequency spectrum in terms of equivalent magnetic and electric dipole moments.[11-13]

For a magnetic current distribution $\tilde{\vec{J}}_{s_m}(\vec{r}\,')$ over an aperture region S_a in the xy-plane, the equivalent magnetic dipole moment $\tilde{\vec{m}}_a$ and the equivalent electric dipole moment $\tilde{\vec{p}}_a$ are defined in terms of the following expressions[12] (which gives the correct scattered fields as in expressions (1.1) to (1.4)),

$$\tilde{\vec{m}}_a = \frac{1}{s\mu} \iint\limits_{S_a} 2\tilde{\vec{J}}_{s_m}(\vec{r}\,')\, dx_a' dy_a' \tag{2.29}$$

and

$$\tilde{\vec{p}}_a = \frac{\varepsilon}{2} \iint\limits_{S_a} 2\tilde{\vec{J}}_{s_m}(\vec{r}\,') \times \vec{r}\,'\, dx_a' dy_a' \tag{2.30}$$

Such a characterization,[12] even though approximate, gives a good representation in the far-field regions. In figures 2.14 and 2.15 are shown the penetrated E_θ electric field component in the region $z > 0$, calculated for the square aperture $\ell = w = 0.15$ wavelength with the incident field oriented normally (fig. 2.14) and edge on incidence (fig. 2.15).

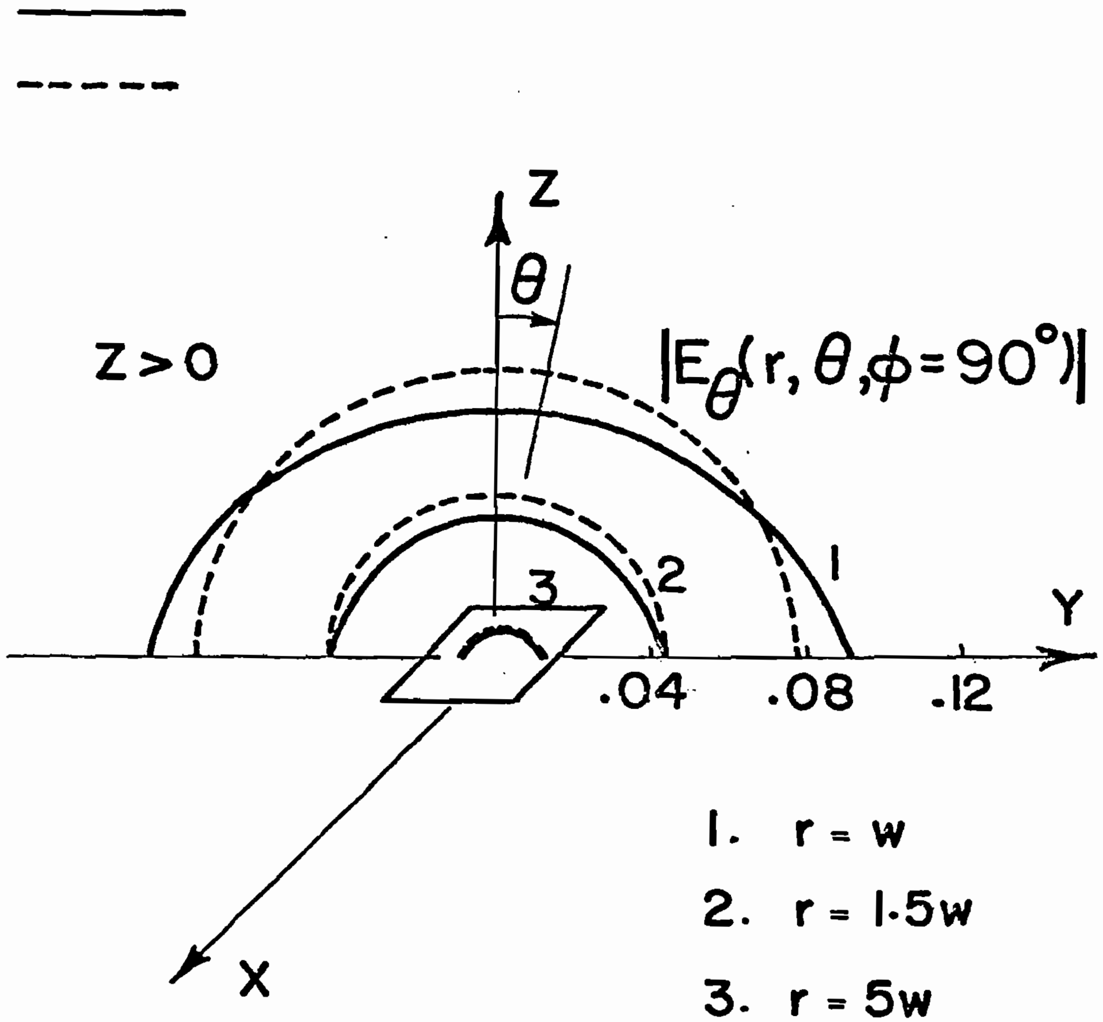

Figure 2.14 Electric Field Penetrated in the Region $z > 0$ for Square Aperture Compared with Magnetic Dipole Moment

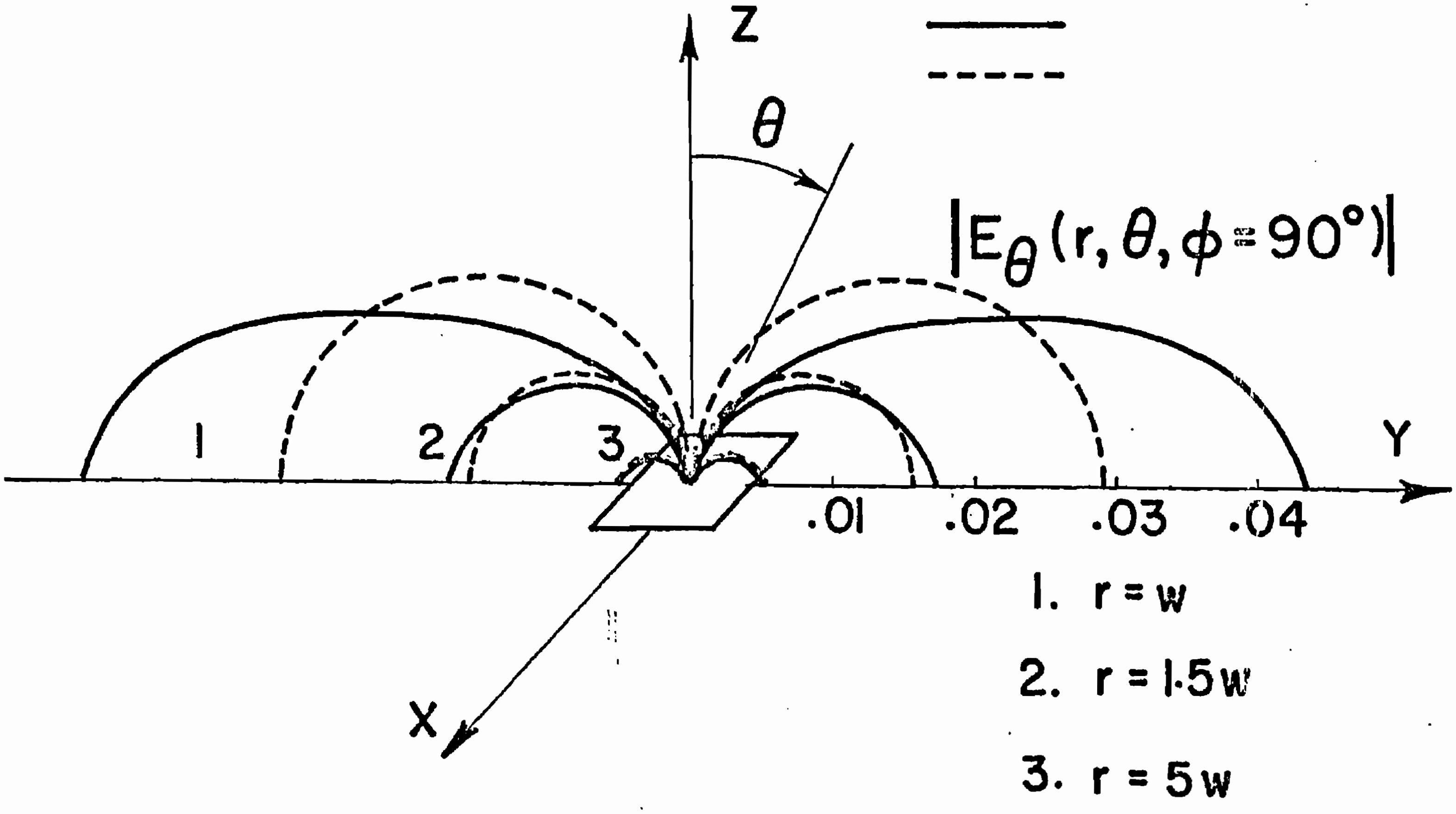

Figure 2.15 Electric Field Penetrated in the Region $z > 0$ for Square Aperture Compared with Electric Dipole Moment

CHAPTER III

Analysis of the Conducting Bodies in the Presence of Ground Screen

Conducting bodies in free space and also above a ground screen are widely treated in the literature for analyzing their scattering characteristics.[24,25] To understand the response of the objects and their coupling to the aperture geometries, it is essential to know the scattering behavior in the presence of the conducting screen. If the aperture S_a is absent in figure 1.1, the complete scattered fields $\tilde{\vec{H}}_+^c$ and $\tilde{\vec{E}}_+^c$ in the right half (+) space can be determined by expressions (1.3) and (1.4). Hence for $z > 0$, in the right half space medium,

$$\tilde{\vec{H}}_+^c(\vec{r},s) = \frac{1}{\mu_+} \nabla \times \tilde{\vec{A}}_+(\vec{r},s) \tag{3.1}$$

$$\tilde{\vec{E}}_+^c(\vec{r},s) = \frac{s}{\gamma_+^2} \left[\nabla(\nabla \cdot \tilde{\vec{A}}_+(\vec{r},s)) - \gamma_+^2 \tilde{\vec{A}}_+(\vec{r},s)\right] \tag{3.2}$$

and the magnetic vector potential $\tilde{\vec{A}}_+(\vec{r},s)$ is again given by the expression (1.8) which has both the scatterer and its image terms included. For a given scatterer geometry, the induced current can be determined subject to the boundary condition (1.14) for perfectly conducting bodies. In fact many of the integral equations obtained in the previous sections for apertures and slots separating two half spaces having the same medium characteristics are the dual equations[21] for the two-dimensional conducting plate and strip problems in a free-space medium. With the ground screen present appropriate image contributions should be included.

A. Arbitrarily Oriented Thin-Wire Configurations

Arbitrarily oriented general thin-wire configurations both in free space and above a conducting ground plane are extensively studied in the literature based on integral equation techniques and the method of moments. As such, the analysis of the wires above a ground plane is similar to the wires in free space, since the concept of images and properties of matrix symmetrization can be invoked[23] and the ground plane replaced by wire images.

In figure 3.1 are shown several wires, one designated the p^{th} wire and another designated the q^{th}. We focus major attention upon the p^{th} wire and investigate how one may calculate the electric field on this wire due to the current $\tilde{I}_p$ on itself plus that due to $\tilde{I}_q$, the current on the q^{th} wire. The contribution on the p^{th} wire due to the presence of wires other than the q^{th} may be calculated in an identical way, and then the total contribution from wires other than the p^{th} is simply a summation over all wires $q = 1,2,\ldots,N (q \neq p)$. Written symbolically, the electric field directed along the axis of the p^{th} wire and evaluated on its surface is

$$\tilde{E}_\zeta(\zeta,s) = \tilde{E}_{p_\zeta}(\zeta,s) + \vec{1}_p \cdot \sum_{\substack{q=1 \\ (q\neq p)}}^{N} \vec{\tilde{E}}_q(\zeta,s) \tag{3.3}$$

where $\tilde{E}_\zeta$ is the total axially directed field on the surface of the p^{th} wire produced by all charges and currents on the structure, $\tilde{E}_{p_\zeta}$ is that due to the current $\tilde{I}_p$, and $\vec{\tilde{E}}_q$ is that due to the q^{th} wire. In equation (3.3) $\vec{1}_p$ is the unit vector along the p^{th} wire (and has the sense of the current $\tilde{I}_p$), and ζ is an independent variable denoting axial displacement along $\vec{1}_p$ of the p^{th} wire in a local coordinate system with origin at the center of the p^{th} wire. Figure 3.2 depicts the two wires and serves to define geometric quantities of interest.

At a general point in space (x,y,z) one may write $\tilde{E}_{p_\zeta}$ in the following form:

$$\tilde{E}_{p_\zeta}(\vec{r},s) = -s\tilde{A}_p(\vec{r},s) - \frac{\partial}{\partial\zeta}\tilde{\Phi}_p(\vec{r},s) \tag{3.4}$$

where $\tilde{A}_p$ and $\tilde{\Phi}_p$ are the vector and scalar potentials, respectively, calculated from the sources on the p^{th} wire. Subject to the

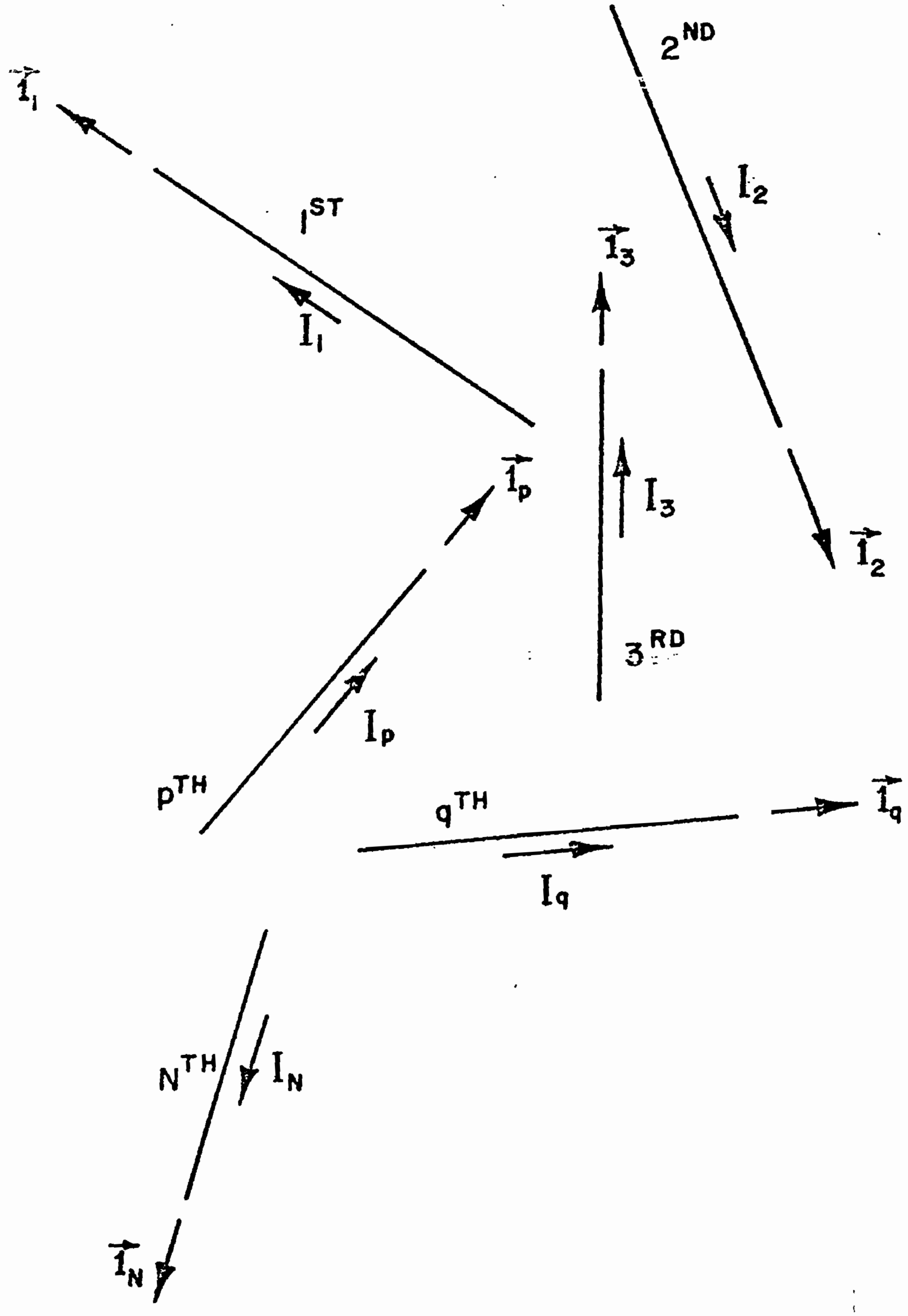

Figure 3.1 Arbitrarily Oriented Wires in Free Space

thin-wire approximations, these potentials may be written as

$$\tilde{A}_p(\vec{r},s) = \frac{\mu}{4\pi}\int_{\zeta'=-L_p/2}^{L_p/2} \tilde{I}_p(\zeta',s)\,\frac{e^{-\gamma|\vec{r}-\vec{r}_p^{\,\prime}|}}{|\vec{r}-\vec{r}_p^{\,\prime}|}\,d\zeta' \tag{3.5}$$

and

$$\tilde{\Phi}_p(\vec{r},s) = \frac{1}{4\pi\varepsilon}\int_{\zeta'=-L_p/2}^{L_p/2} \tilde{\rho}_{\ell_p}(\zeta',s)\,\frac{e^{-\gamma|\vec{r}-\vec{r}_p^{\,\prime}|}}{|\vec{r}-\vec{r}_p^{\,\prime}|}\,d\zeta' + \tilde{\Phi}_p^{r+}(\vec{r},s) + \tilde{\Phi}_p^{r-}(\vec{r},s) \tag{3.6}$$

where the general point (x,y,z) is located by

$$\vec{r} = x\vec{1}_x + y\vec{1}_y + z\vec{1}_z \tag{3.7}$$

and a source point on the pth wire by

$$\vec{r}_p^{\,\prime} = \vec{r}_p^{\,c} + \zeta'\vec{1}_p \tag{3.8}$$

In (3.5), $\vec{r}_p^{\,c}$ is a vector which locates the center of the pth wire so (3.8) itself is simply the equation of a straight line in space along the axis of the pth wire. The linear charge density on the pth wire is denoted ρ_{ℓ_p} and is, of course, related to the pth wire current by the continuity equation,

$$\frac{d}{d\zeta}\tilde{I}_p(\zeta,s) + s\tilde{\rho}_{\ell_p}(\zeta,s) = 0 \tag{3.9}$$

In (3.6) the two terms, $\tilde{\Phi}_q^{r+}$ and $\tilde{\Phi}_q^{r-}$, represent contributions to the scalar potential from the rings of discrete charge located, respectively, at the upper and lower ends of the pth wire. These charges are present whenever the current is not zero at the ends as is necessary, if the analysis is to be extended to structures involving wires which join at their end-points.

Similarly, the electric field $\tilde{\vec{E}}_q(\vec{r})$ due to sources on the q^{th} wire may be written

$$\tilde{\vec{E}}_q(\vec{r},s) = -s\tilde{A}_q(\vec{r},s)\vec{1}_q - \text{grad}\ \tilde{\Phi}_q(\vec{r},s) \tag{3.10}$$

where $\tilde{A}_q\vec{1}_q$ and $\tilde{\Phi}_q$ are the vector and scalar potentials, respectively, calculated from the sources on the q^{th} wire. $\tilde{A}_q$ and $\tilde{\Phi}_q$ can be expressed in terms of potential integrals like those of (3.5) and (3.6) with p replaced by q. The unit vector $\vec{1}_q$ is directed along the q^{th} wire and has the sense of the defined current on this wire.

Since the contributions on the p^{th} wire due to the currents on the other wires are all of the form of (3.10), only two wires are tested in general below (fig. 3.3) so that the discussion is not rendered overly complex. The extension to more than two wires is quite direct and can be done readily after the present two-wire case foundation has been established.

The axially directed electric field on the surface of the p^{th} wire shown in figure 3.2, due to sources on both the p^{th} and q^{th} wires, is

$$\tilde{E}_\zeta = -s\tilde{A}_p - \frac{\partial}{\partial\zeta}\ \tilde{\Phi}_p - s\tilde{A}_q(\vec{1}_q \cdot \vec{1}_q) - \frac{\partial}{\partial\zeta}\ \tilde{\Phi}_q \tag{3.11}$$

Retaining $\tilde{\Phi}_q$ but employing the Lorentz gauge explicitly to eliminate $\tilde{\Phi}_p$ one may convert (3.11) to an alternate form:

$$\begin{aligned}\frac{\gamma^2}{s}\ \tilde{E}_\zeta(\zeta,s) &= \left(\frac{\partial^2}{\partial\zeta^2} - \gamma^2\right)\tilde{A}_p(\zeta,s) - \gamma^2\tilde{A}_q(\zeta,s)(\vec{1}_q \cdot \vec{1}_q)\\ &\quad - \frac{\gamma^2}{s}\frac{\partial}{\partial\zeta}\ \tilde{\Phi}_q(\zeta,s)\end{aligned} \tag{3.12}$$

Actually, the Lorentz gauge is invoked implicitly relative to $\tilde{\Phi}_q$, for otherwise the potential integral representation of the scalar

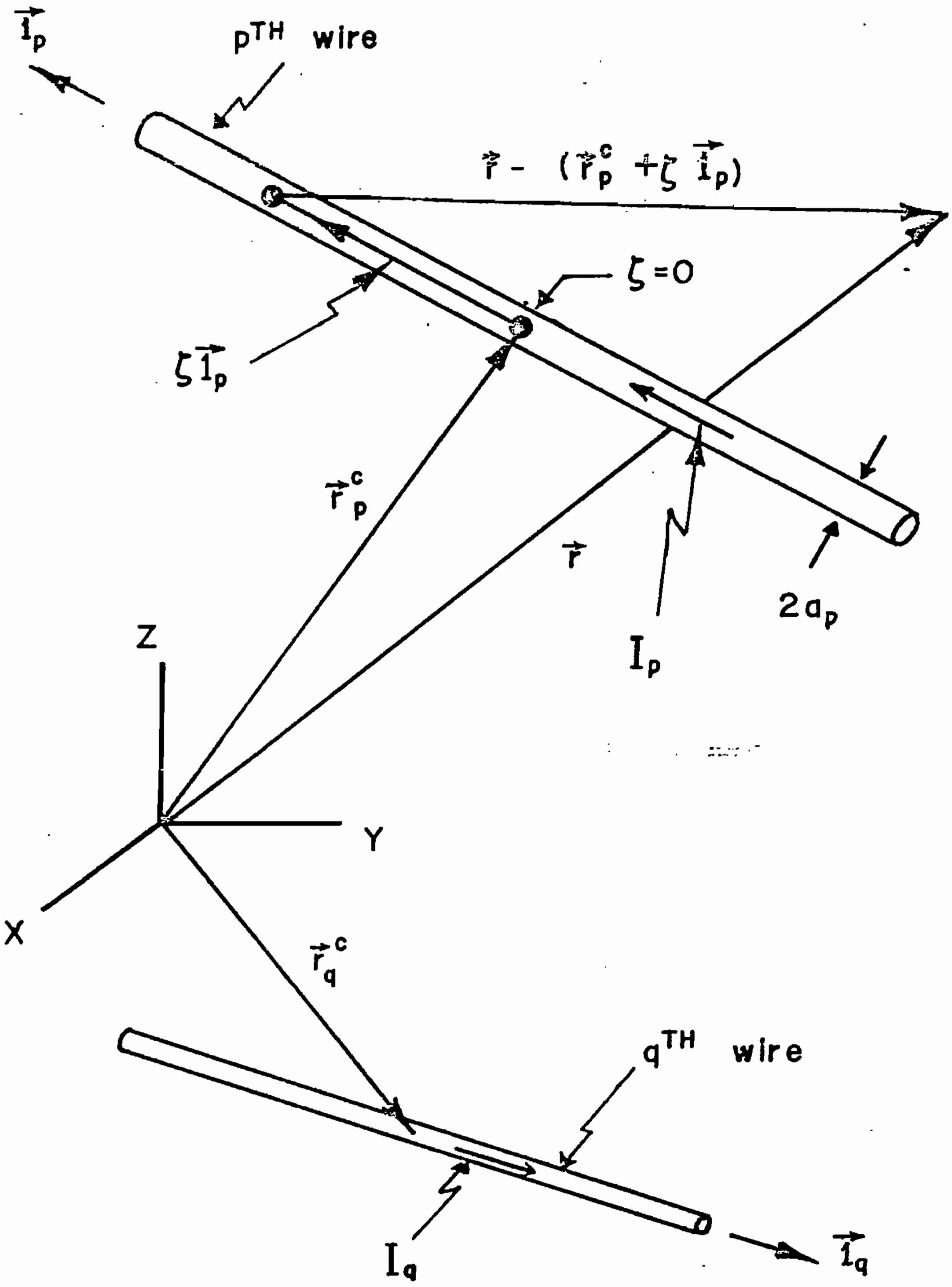

Figure 3.2 Coordinates of Two Coupled Wires

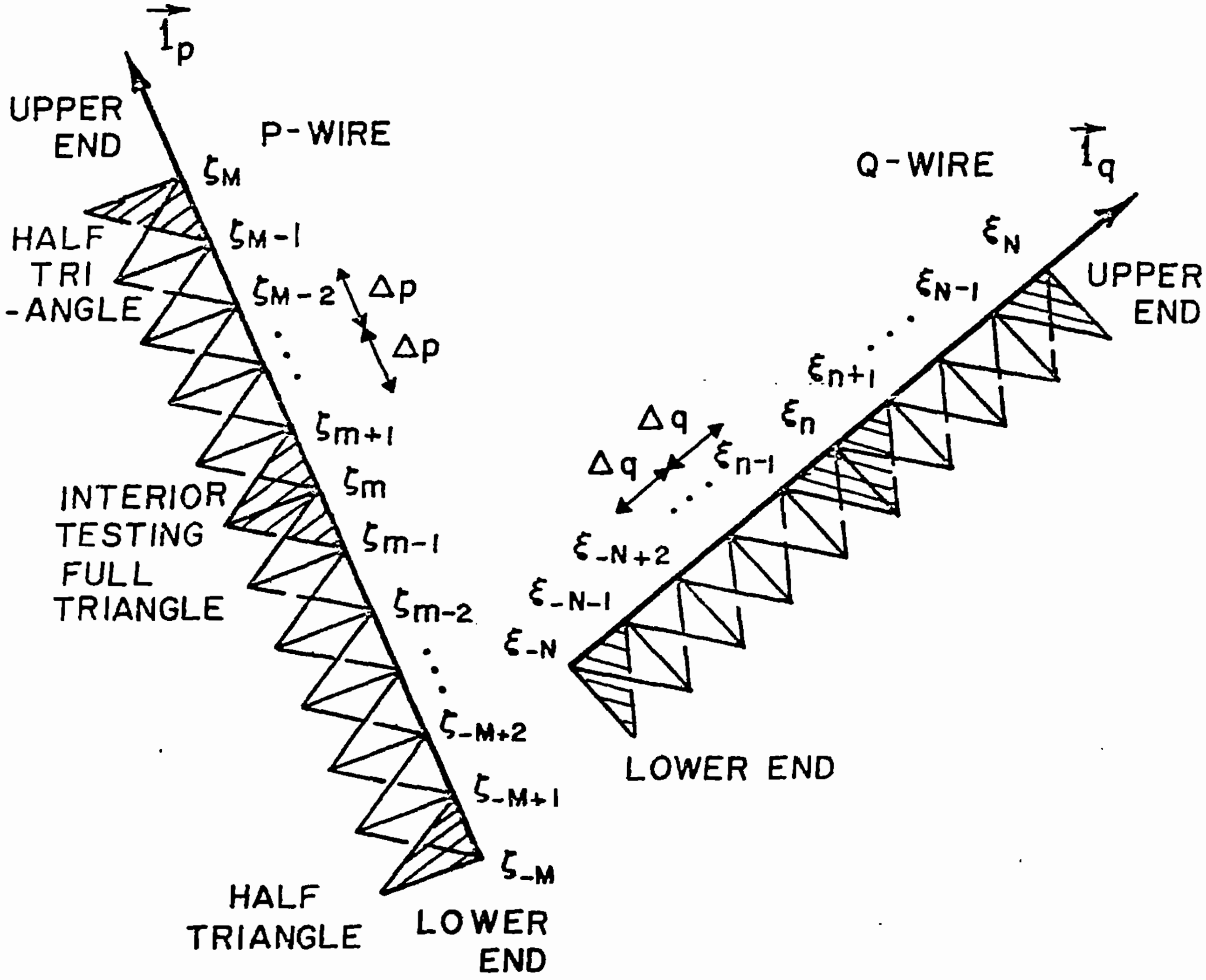

Figure 3.3 Testing Triangles on Two Coupled p and q Wires

potential, would be inappropriate; however, in (3.12) the relationship between $\tilde{\Phi}_q$ and $\tilde{A}_q$ is not invoked directly. In view of the heterogeneous application above of the relationship between vector and scalar potential under the Lorentz gauge, one must exercise care to avoid violation of the continuity equation, when he calculates Φ_q from the charge on the q^{th} wire. When this wire joins others, as is anticipated by the expression (3.6), special heed must be given to this caution.

B. Numerical Examples of Wire Structures

As an example of the application[23] of the integral equation (3.12) to general wire structures above a ground plane, numerical results are presented for biconical wire structures. The expression (3.12) is converted into a matrix equation, similar to the equation (1.25) based on the method of moments.[16] The effect of the ground plane is taken into account by introducing the wire images and invoking the symmetry of the geometry. In figure 3.4 is shown the geometry of a wire biconical antenna[23] in free space, and in figures 3.5 and 3.6 are shown the distribution of the current on the structure and the far-field radiation pattern for some specific geometries. Further the geometry of a wire biconical antenna above and perpendicular to the ground plane is shown in figure 3.7 and the corresponding current induced in figure 3.8. Similarly, figure 3.10 gives the current induced on a wire biconical antenna above and parallel to a ground plane geometry shown in figure 3.9. For these geometries, symmetry allows one to reduce the partitioned matrix size to a smaller number of unknowns in the matrix evaluation.

C. Two-Dimensional Conducting Scatterer Above a Ground Plane

In the formulation of the problem of determining the current distribution on finite cylindircal structures, it is usually necessary to assume that the cylinder is thin so that the current density around the circumference of the cylinder is uniform. When this is not the case, one must solve a coupled set of integral

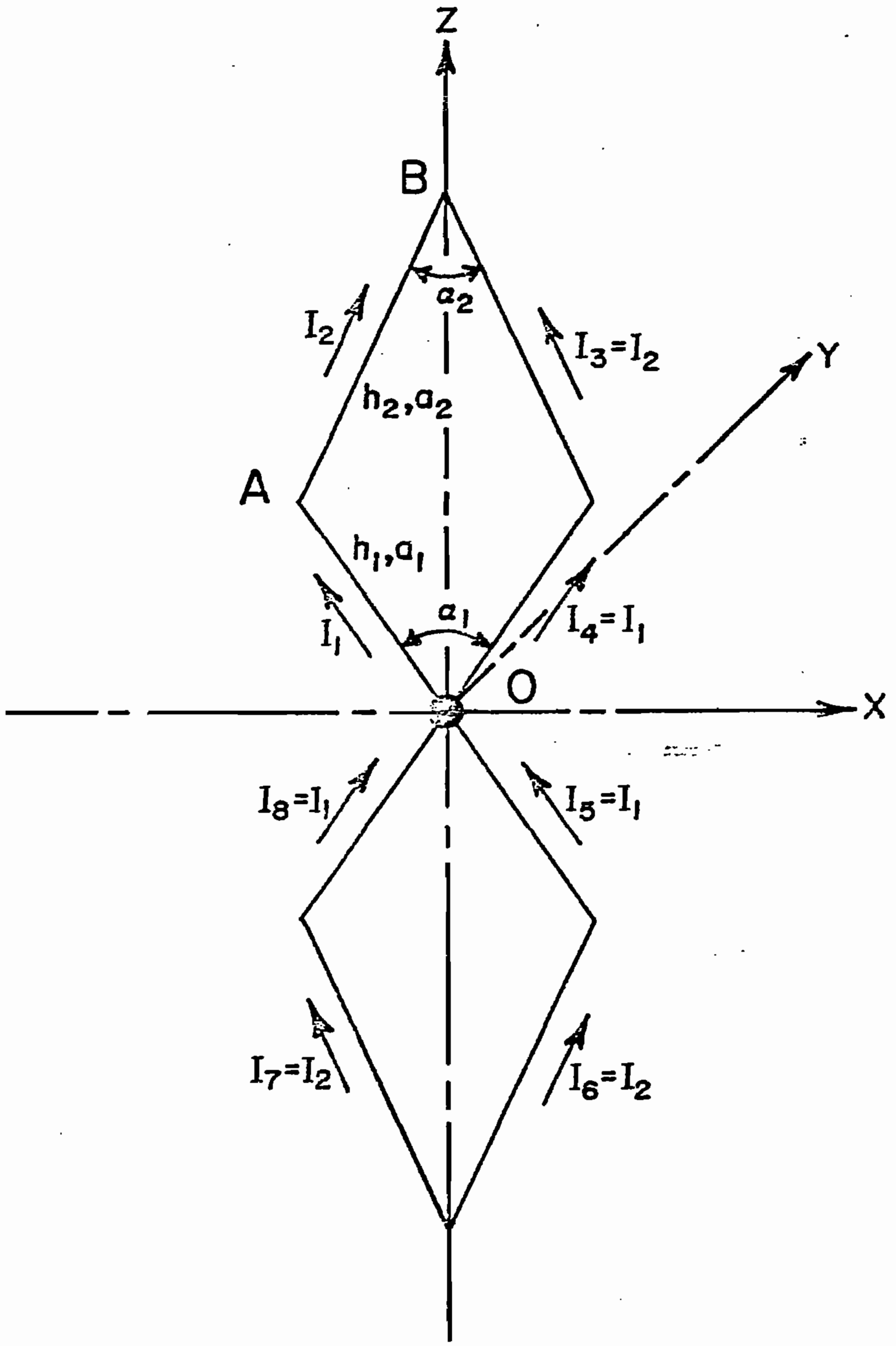

Figure 3.4 Wire Biconical Antenna in Free Space

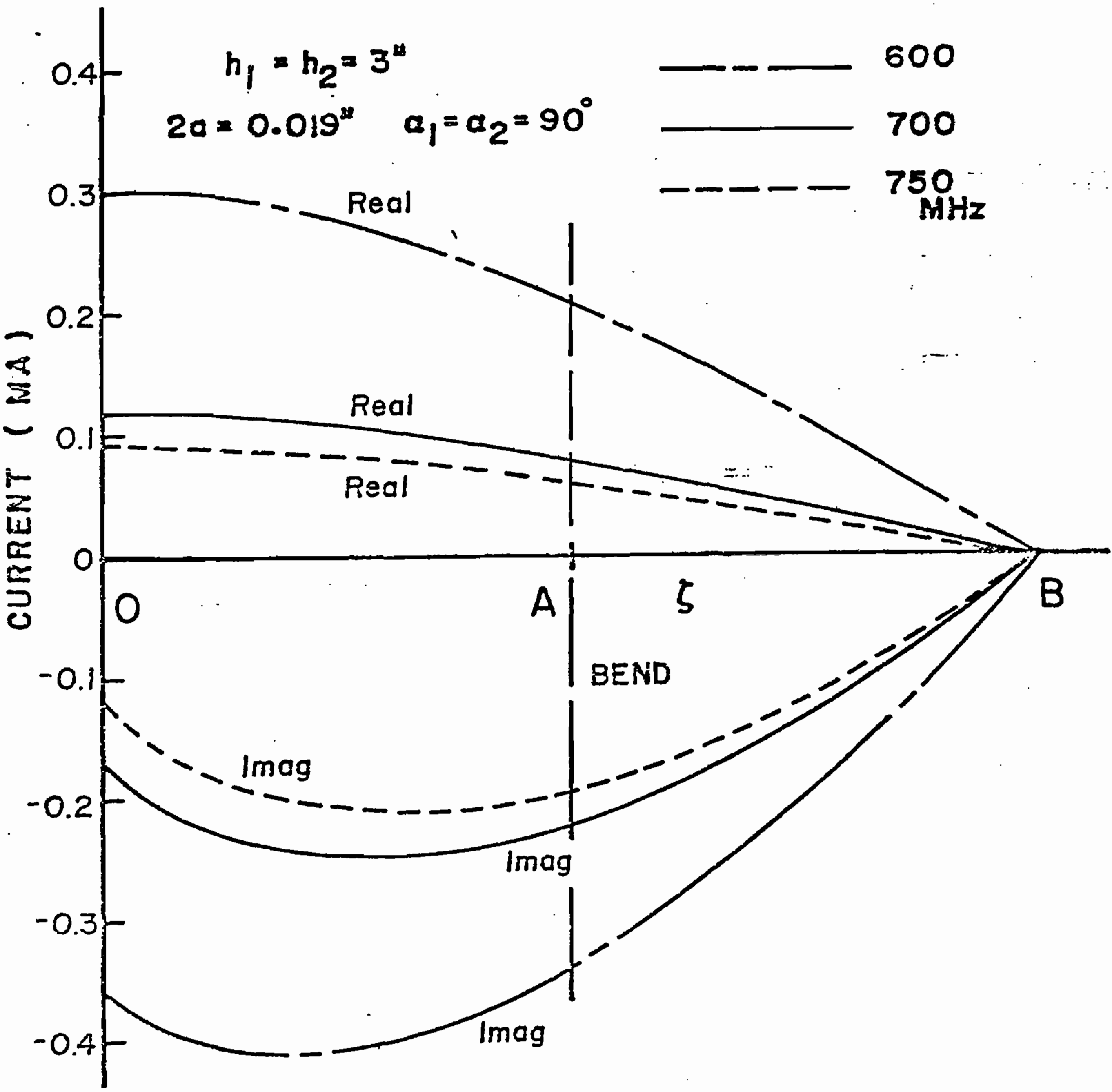

Figure 3.5 Currents I_1 and I_2 on Wire Biconical Antenna in Free Space

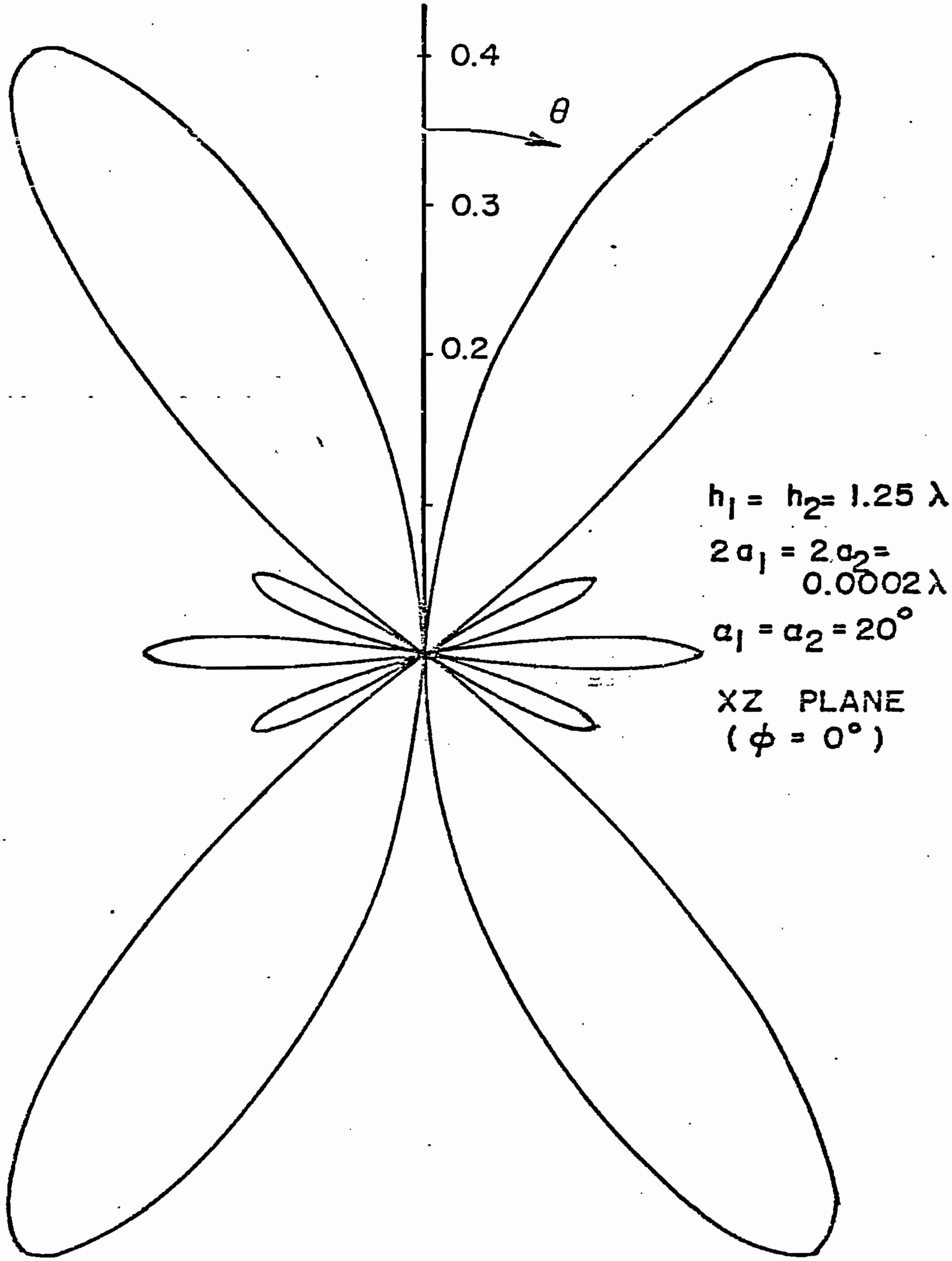

Figure 3.6 Far Field Pattern of Wire Biconical Antenna in Free Space, E_θ-Component

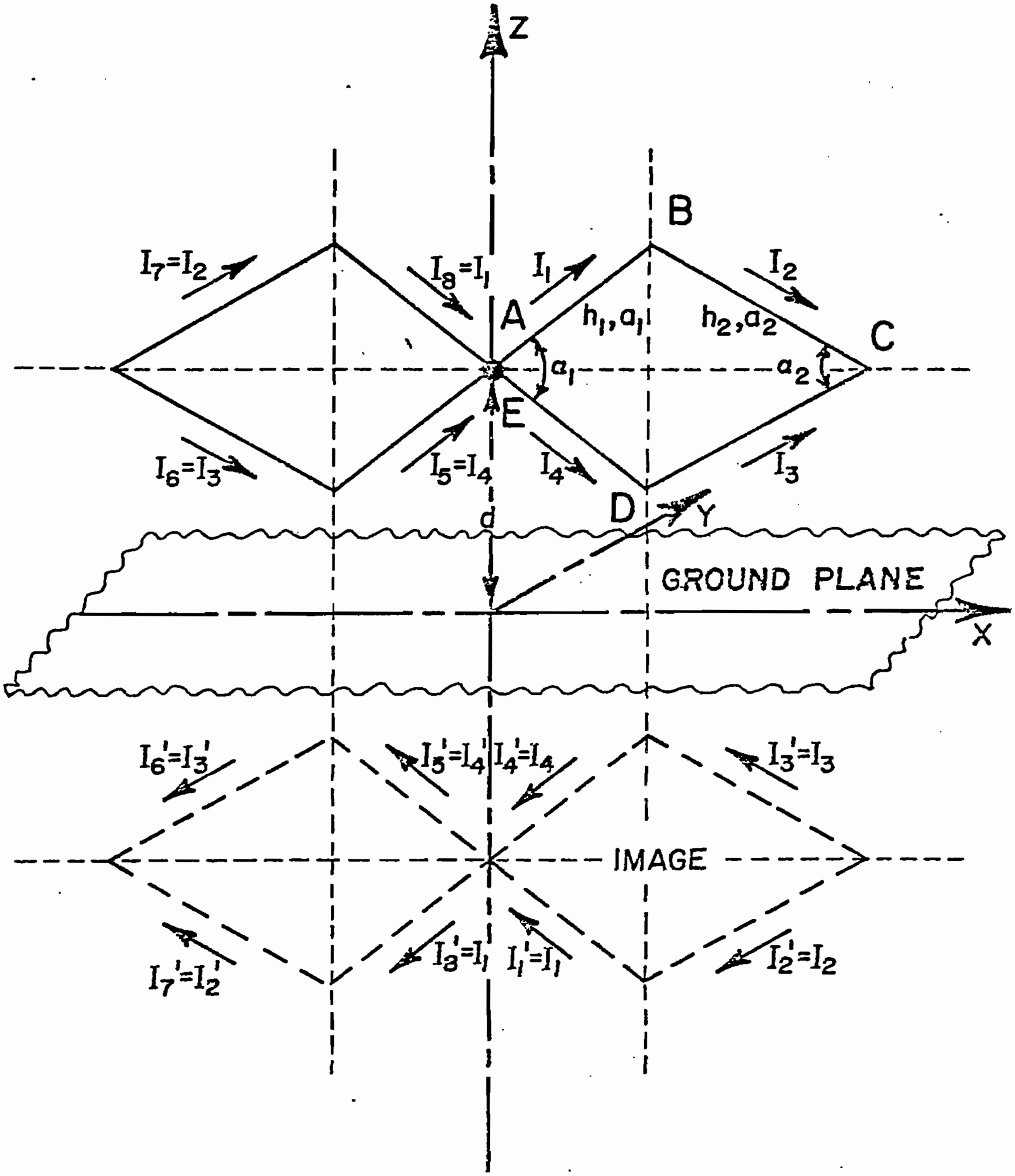

Figure 3.7 Wire Biconical Antenna Above and Perpendicular to Ground Plane

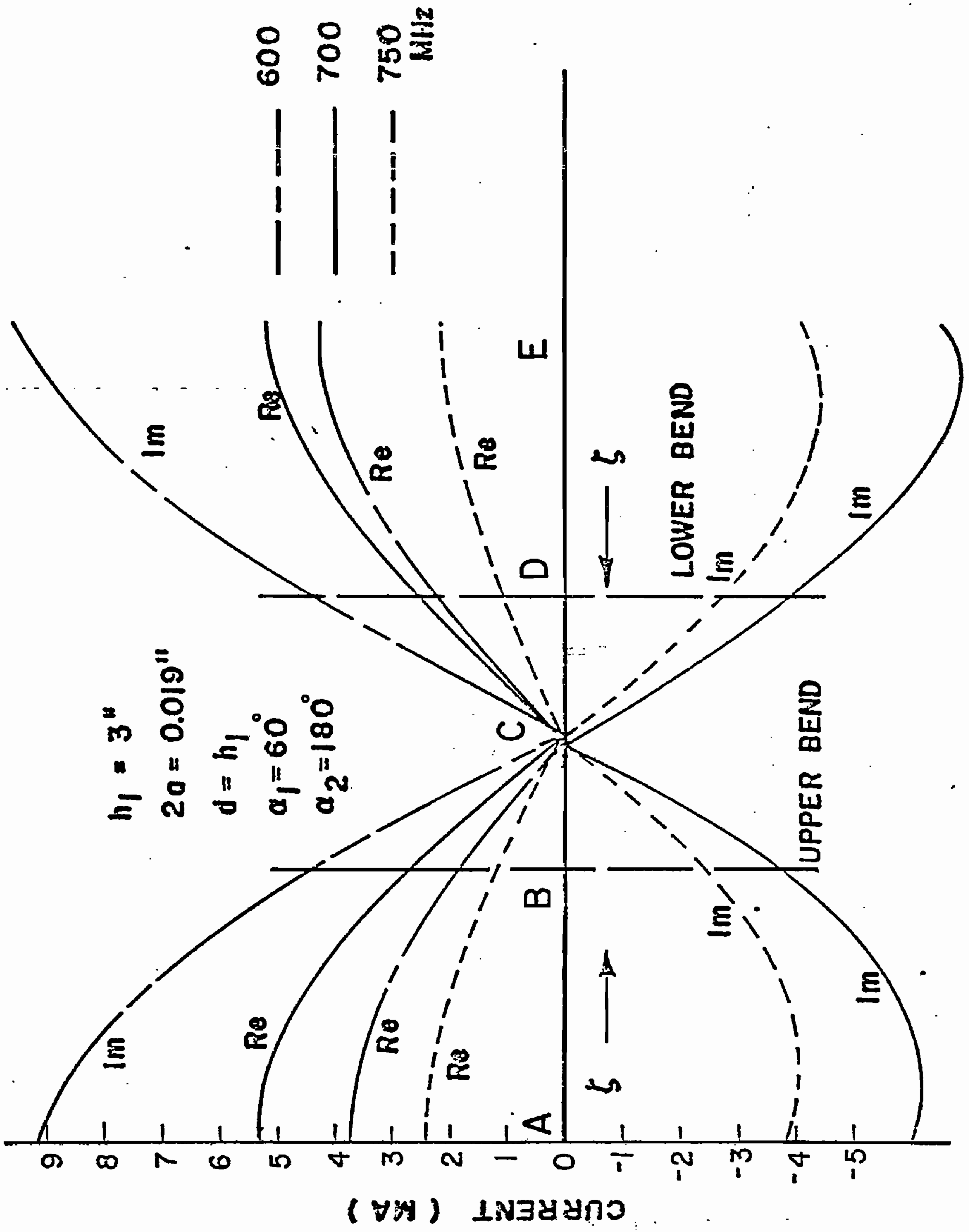

Figure 3.8 Currents I_1, I_2 and I_3, I_4 on Wire Biconical Antenna Above and Perpendicular to Ground Plane

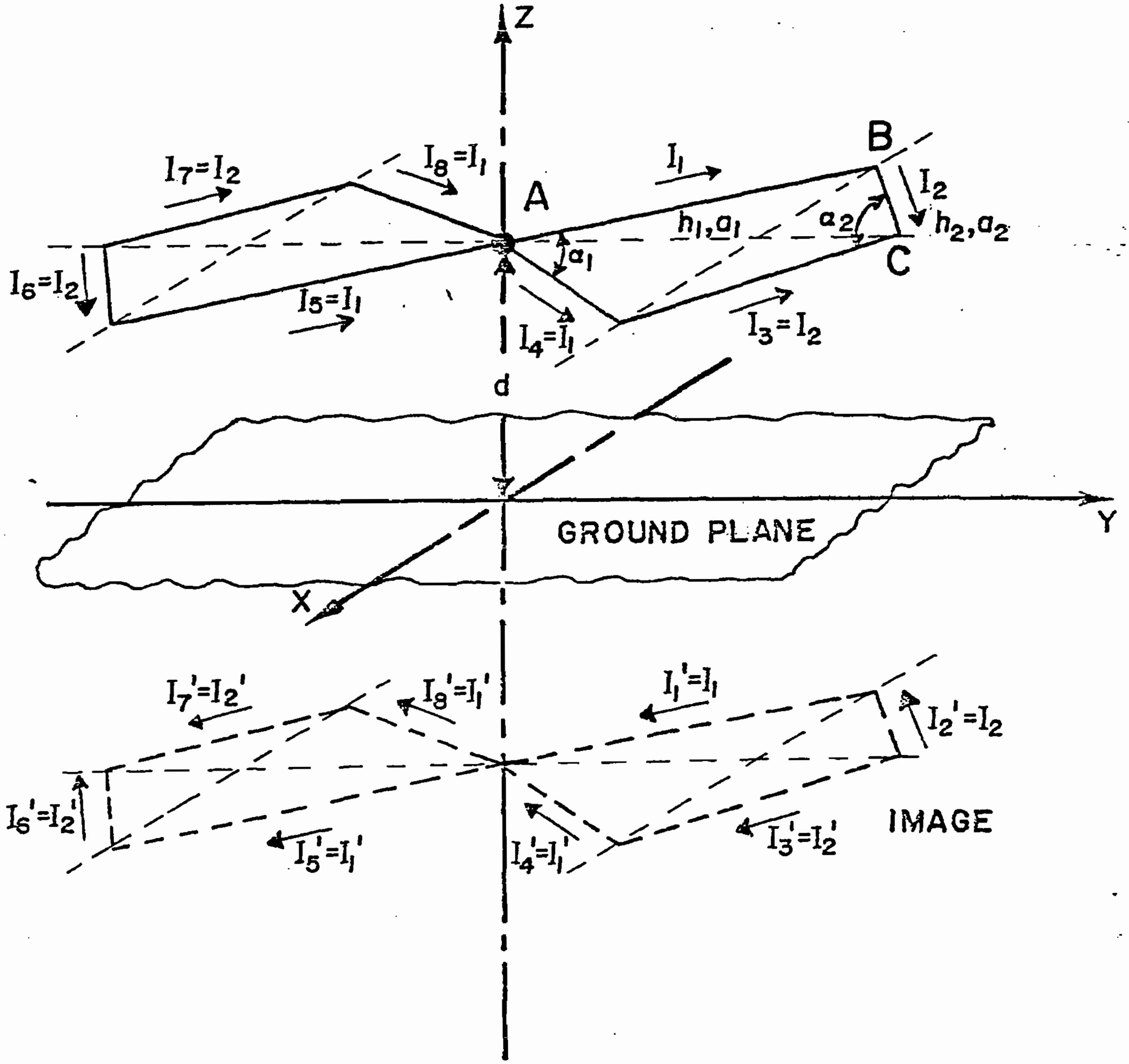

Figure 3.9 Wire Biconical Antenna Above and Parallel to Ground Plane

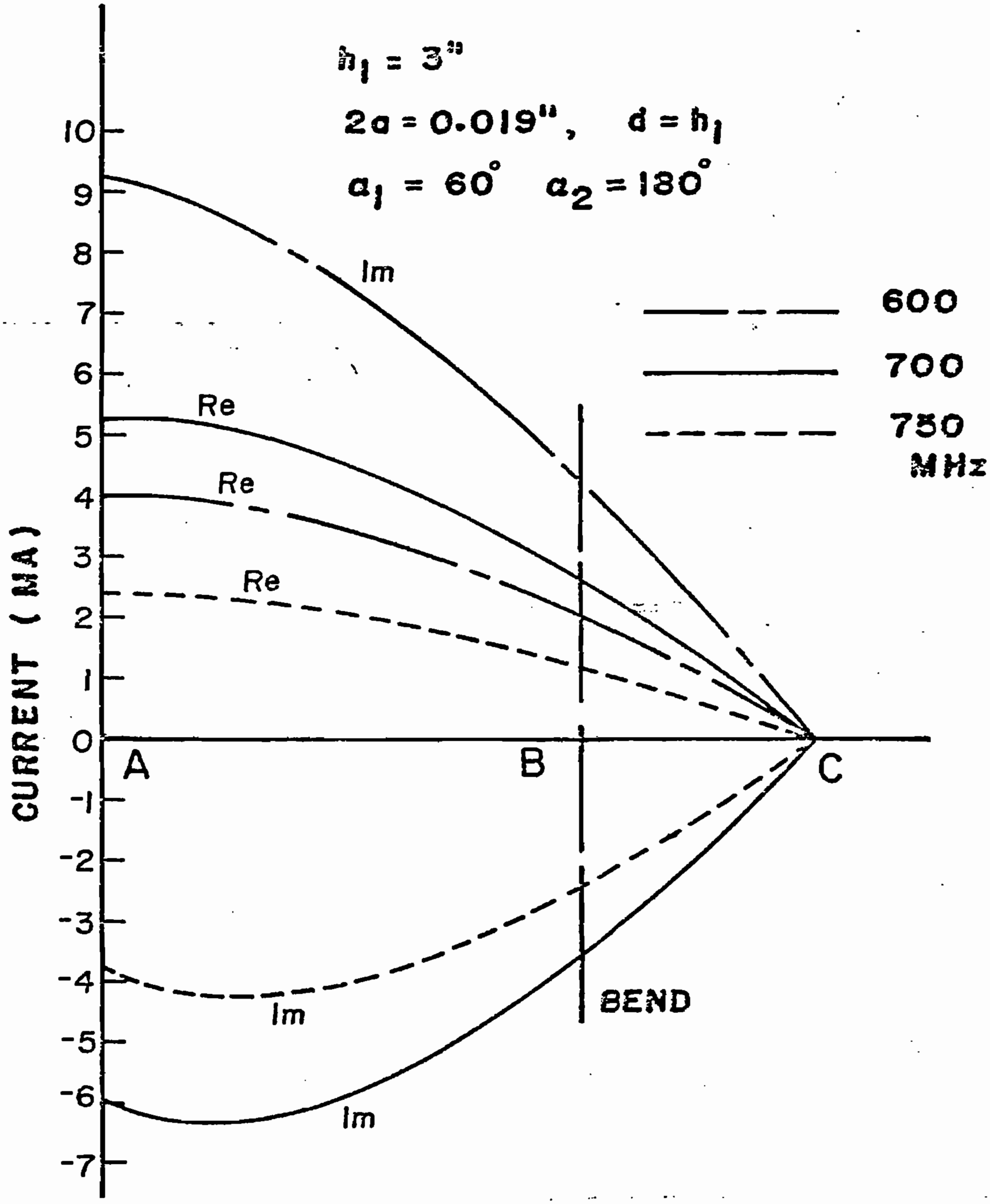

Figure 3.10 Currents I_1 and I_2 on Wire Biconical Antenna Above and Parallel to Ground Plane

equations as has been done by Kao.[24-26] This method is impractical for very long cylinders, however, as one is limited by the storage capacity of the computer. Harrison[27] has shown that at least the qualitative features of the circumferential variation of the axial component of current on a cylinder in free space may be obtained quite simply by treating the infinite cylinder. He points out that for the infinite cylinder with an incident electric field polarized parallel to the axis of the cylinder, there exists no mechanism for the excitation of circumferentially directed currents, thus decoupling the set of integral equations. Furthermore, since the cylinder is infinite, the current distribution is the same at any cross-section and the integral equation becomes one-dimensional. Harrison shows that for circular cylinders in free space is it not necessary to solve an integral equation at all, but simply solve the boundary value problem using cylindrical wavefunctions.

If the cylinder lies parallel to an infinite perfectly conducting ground as in figure 3.11, one may employ image theory and replace the ground by equivalent image currents as shown in figure 3.12. Again, to attack the problem rigorously is a formidable task for long cylinders. However, if the cylinder is of infinite extent, then for the polarization shown in figure 3.11 (termed TM polarization) a rather simple integral equation for the surface current density $\tilde{J}_z$ can be derived.

In this section, the resulting integral equation is solved for the current distribution with a plane wave incident perpendicular to the cylinder axis. It is noted that the problem could be treated alternatively as a boundary value problem using cylindrical wavefunctions similar to the methods used by Row[28] and Olaofe[29] in the scattering by parallel cylinders. With either approach, however, one must solve a linear system of equations, but the integral equation approach has the advantage that it is also applicable to cylinders of arbitrary cross-section.

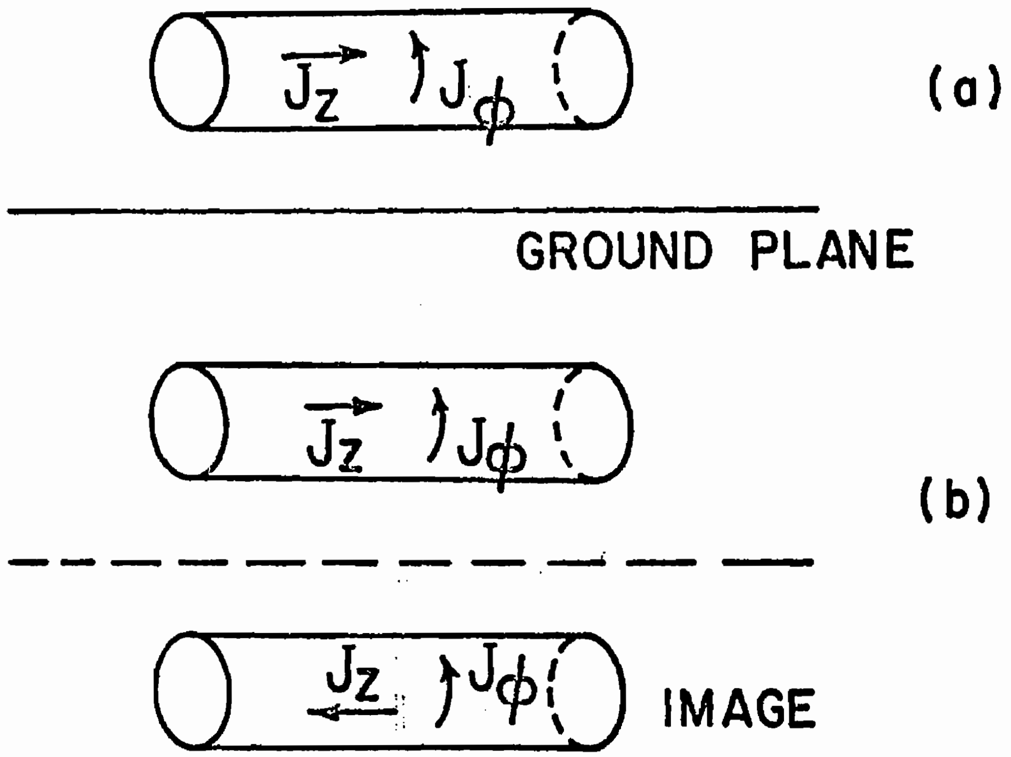

Figure 3.11 (a) Conducting Cylinder Above a Ground Plane
(b) Ground Plane Replaced by a Cylinder Image

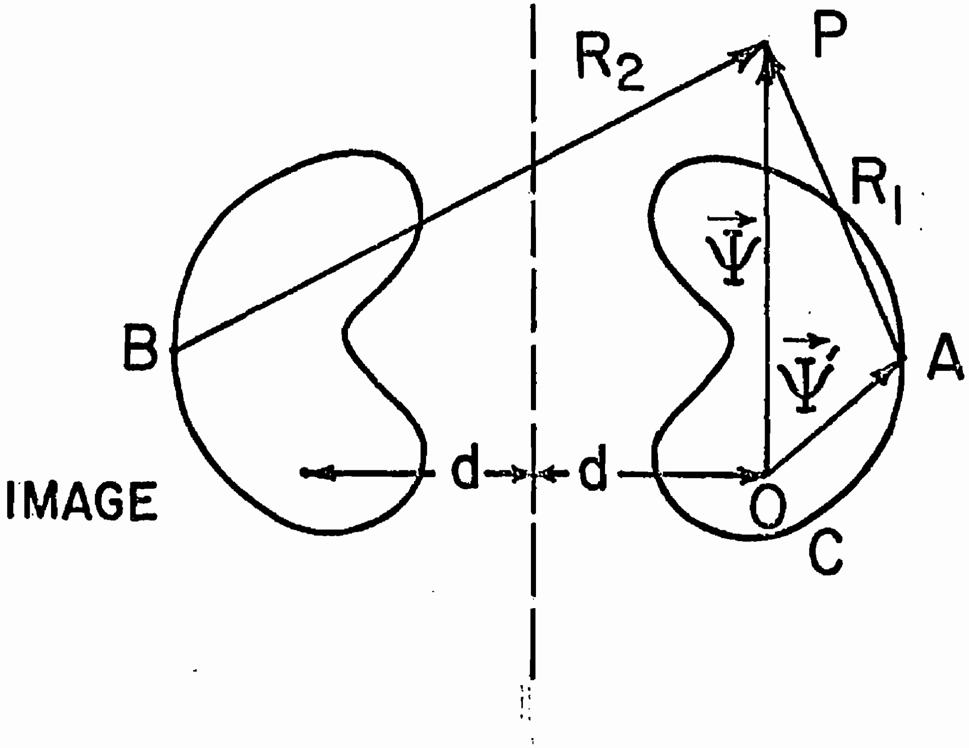

Figure 3.12 Geometry for the TM Scattering of an Infinite Cylinder and Its Image

Referring to figure 3.12, a general observation point P in space is located in cylindrical coordinates by the vector $\vec{r} = (\Psi, \phi, z=0)$ with respect to the origin O located inside the cylinder with boundary C. The cylinder lies parallel to and a distance d above the ground plane. By image theory, the axial current density $\tilde{J}_z$ on the body at point A located by $\vec{r}\,' = (\Psi', \phi', z'=0)$ is the negative of the current at the corresponding image point B which is found by reflection in the ground plane. Thus, the scattered electric field at point P may be written from the surface current on the cylinder and its image as

$$\tilde{E}_z^s(\Psi, j\omega) = -\frac{k\eta}{4} \int_C \tilde{J}_z(\vec{\Psi}\,', j\omega)\left[H_o^{(2)}(kR_1) - H_o^{(2)}(kR_2)\right] d\ell' \tag{3.13}$$

where

$$R_1 = \left[\Psi^2 + \Psi'^2 - 2\Psi\Psi' \cos(\phi - \phi')\right]^{\frac{1}{2}} \tag{3.14}$$

$$R_2 = \left[\Psi^2 + \Psi'^2 + 2\Psi\Psi' \cos(\phi + \phi') + 4d(\Psi \cos\phi + \Psi' \cos\phi') + 4d^2\right]^{\frac{1}{2}} \tag{3.15}$$

In the expression (3.13), k is the free space wave number and Z_o the corresponding characteristic free space impedance. The first term in the brackets is the contribution due to the current on the cylinder whereas the second term corresponds to the fields produced by the image. Boundary conditions require, expression (1.14), tangential electric field to be zero on the surface of the cylinder along the boundary C. Hence, we have the integral equation,

$$\frac{kZ_o}{4} \int_C \tilde{J}_z(\vec{r}\,', j\omega)\left[H_o^{(2)}(kR_1) - H_o^{(2)}(kR_2)\right] d\ell' = \tilde{E}_z^i(\vec{r}, j\omega) \ , \ \vec{\Psi} \text{ on } C \tag{3.16}$$

in which for a plane wave incident at an angle ϕ^i,

$$\tilde{E}_z^i(\vec{r}, j\omega) = \tilde{E}_o^i\left[e^{jk\Psi\cos(\phi-\phi^i)} - e^{-jk\{2d\cos\phi^i + \Psi\cos(\phi+\phi^i)\}}\right] \tag{3.17}$$

D. Numerical Results for Circular Cylinder

The basic advantage in the formulation of the integral equation (3.16) is that one can analyze general arbitrary-cross-section, two-dimensional geometries. Based on the matrix method[17] discussed in Chapter I, the numerical results are obtained for an infinitely long circular cylinder. In the figures 3.13 and 3.14 are shown the magnitude and phase of the surface current distribution on a circular cylinder placed above a ground screen and illuminated by a plane wave incident at an angle of 45^o. Curves are also shown for few values of d. It is noted that the variation of the incident field normal to the conducting ground plane is that of a standing wave, while along the ground plane it is a traveling wave. Thus the illumination on the cylinder is stronger on the side of the cylinder away from the ground plane causing some of the asymmetry in the current distribution.

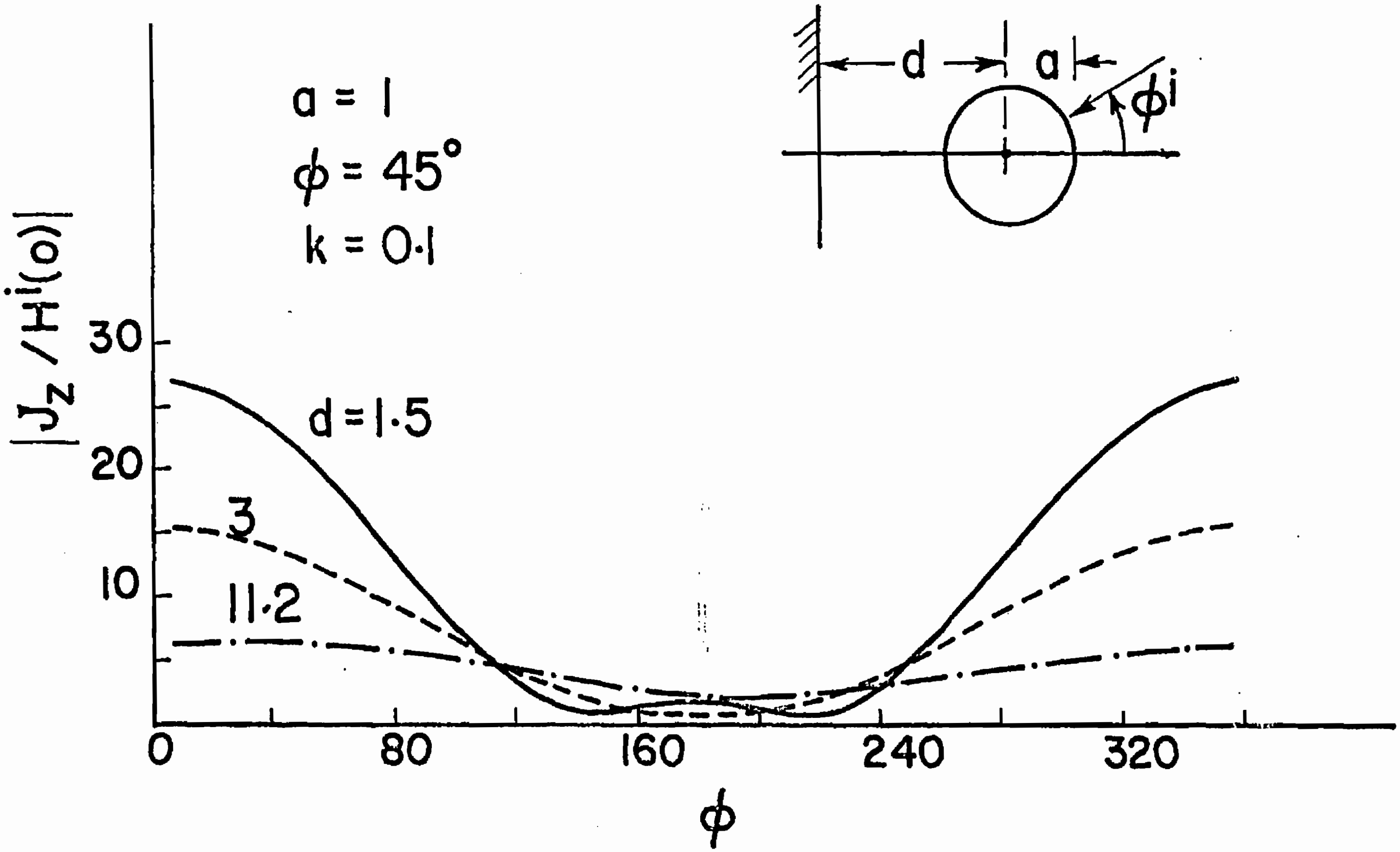

Figure 3.13 Magnitude of the Current (TM) on Infinite Cylinder Above Ground Plane

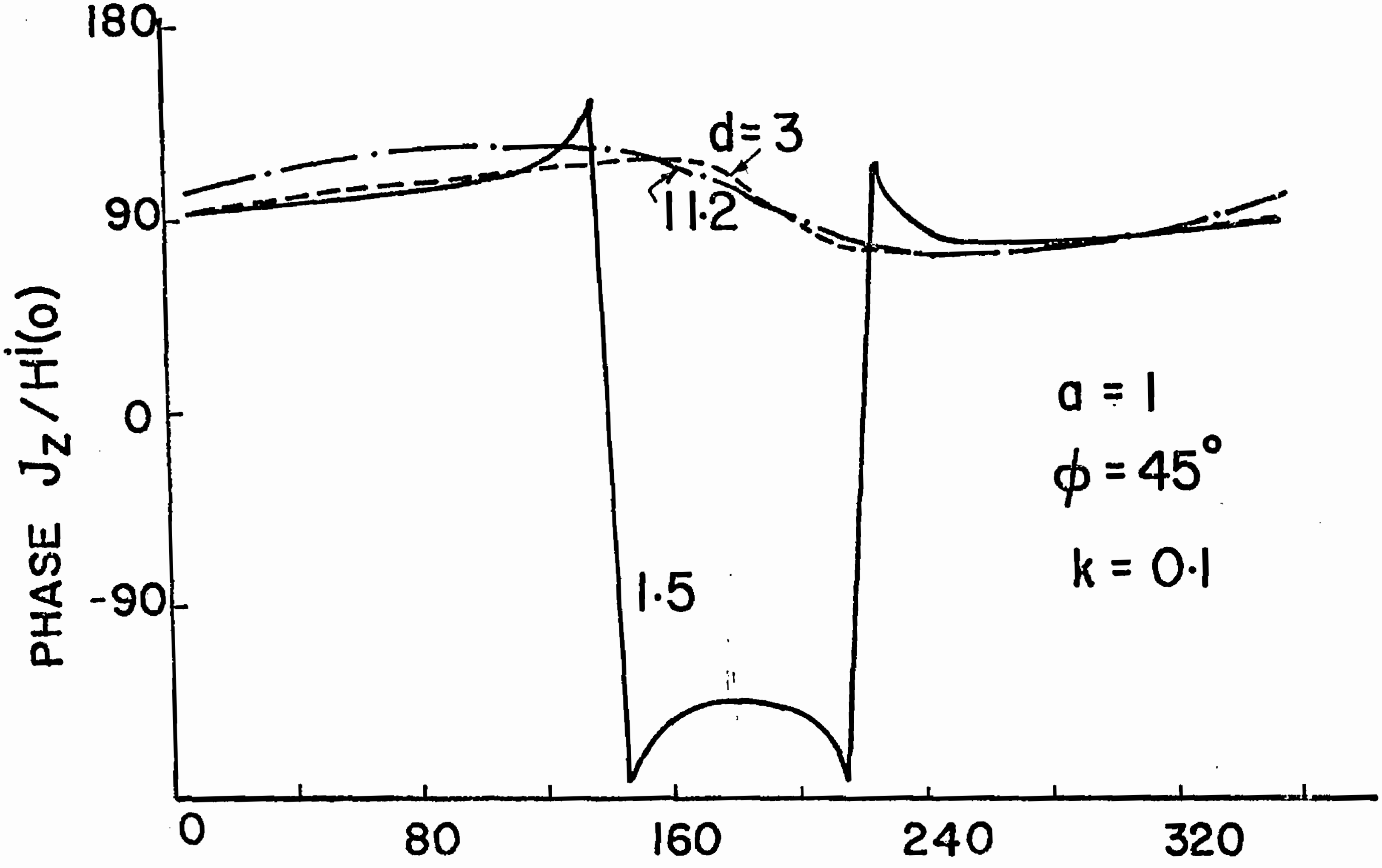

Figure 3.14 Phase of the Current (TM) on Infinite Cylinder Above Ground Plane

CHAPTER IV

Characterization of Bodies Behind Aperture-Perforated Screen

The general interaction problem of electromagnetic excitation of arbitrarily shaped conducting bodies through an aperture-perforated conducting screen is discussed in Chapter I and the coupled set of integro-differential equations (1.15) and (1.16), if solved for specific geometries, explain completely the interaction involved. As pointed out earlier, one has to resort to numerical methods[16] for solution to the integral equations. In the previous sections, few specific cases are discussed as special geometries, individually aperture alone with no scatterers nearby (Chapter II), and also conducting wire geometries in the presence of ground screen with apertures shorted (Chapter III). These cases do explain the complexities involved in the numerical solution procedure, and the responses thus far obtained give some insight into understanding the general aperture-scatterer coupling problem. In the following sections, some specific coupled aperture-scatterer geometries of practical interest are discussed. The general integral equations (1.15) and (1.16) are specialized and both the frequency domain and the time domain responses are obtained.

A. Finite Wire Scatterer Behind a Rectangular Aperture

The geometry of a finite length wire excited through a slotted screen is shown in figure 4.1. The finite length wire is oriented arbitrarily along the unit vector $\vec{1}$ with its center at (x_c, y_c, z_c). L is the total length of the wire and a its radius. The origin of the coordinate system coincides with the center of the rectangular aperture of total length ℓ and width w. The incident field $(\tilde{\vec{E}}^i, \tilde{\vec{H}}^i)$ impinging on the aperture, penetrates and couples to the wire. The treatment of this boundary value problem[9] is similar to the theory discussed in Chapter I, and the following integral equations result from the expressions (1.15) and (1.16) for the coupled geometry

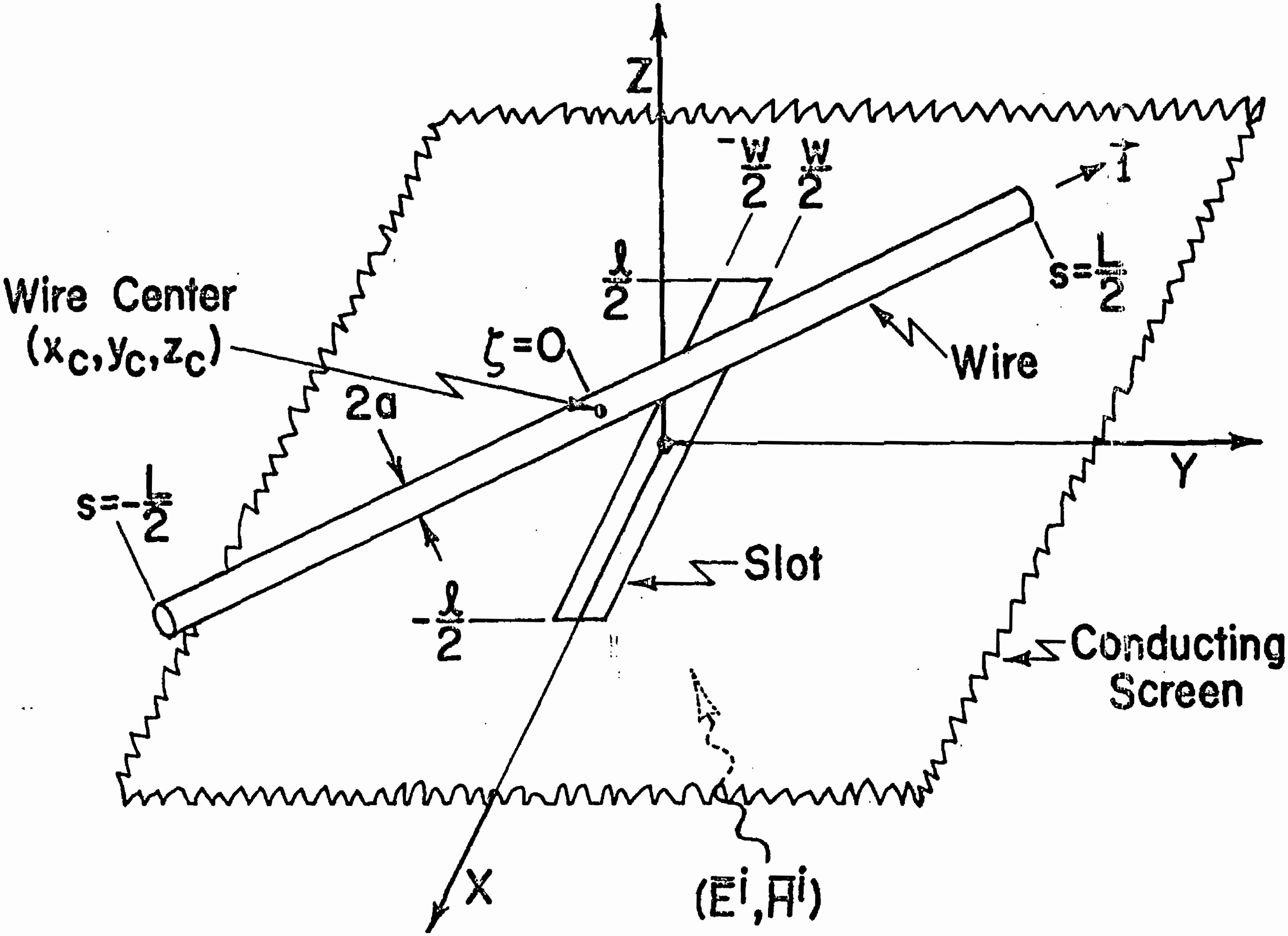

Figure 4.1 Finite Wire Scatterer Behind Narrow Slot Conducting Screen

shown in figure 4.1. It is further assumed that both sides of the media separated by the screen have the same free-space characteristics:

$$\left(\frac{\partial^2}{\partial x^2} - \gamma^2\right)\tilde{A}_{m_x}(x,y,s) + \frac{\partial^2}{\partial x \partial y}\tilde{A}_{m_y}(x,y,s) + \frac{s\varepsilon}{2}\left[\frac{\partial}{\partial z}\tilde{A}_y(x,y,s) - \frac{\partial}{\partial y}\tilde{A}_z(x,y,s)\right] = -\frac{\gamma^2}{s}\tilde{H}^i_x(x,y,s) \quad , \quad (x,y) \in S_a \tag{4.1}$$

$$\left(\frac{\partial^2}{\partial y^2} - \gamma^2\right)\tilde{A}_{m_y}(x,y,s) + \frac{\partial^2}{\partial y \partial x}\tilde{A}_{m_x}(x,y,s) + \frac{s\varepsilon}{2}\left[\frac{\partial}{\partial x}\tilde{A}_z(x,y,s) - \frac{\partial}{\partial z}\tilde{A}_x(x,y,s)\right] = -\frac{\gamma^2}{s}\tilde{H}^i_y(x,y,s) \quad , \quad (x,y) \in S_a \tag{4.2}$$

In the expressions, $\tilde{A}_{m_x}$ and $\tilde{A}_{m_y}$ are the x and y components of the electric vector potentials and are defined in the expression (2.6). Further the bracketed terms due to presence of the wire are given by

$$\frac{s\varepsilon}{2}\left[\frac{\partial}{\partial z}\tilde{A}_y(x,y,s) - \frac{\partial}{\partial y}\tilde{A}_z(x,y,s)\right]_{z=0} = -\frac{s\mu\varepsilon}{4\pi}\int_{\zeta'=-L/2}^{L/2}\tilde{I}(\zeta') \cdot \left[z_c \cos\beta + (y - y_c)\cos\nu\right]\tilde{g}_1(x,y;\zeta')\,d\zeta' \tag{4.3}$$

and

$$\frac{s\varepsilon}{2}\left[\frac{\partial}{\partial x}\tilde{A}_z(x,y,s) - \frac{\partial}{\partial z}\tilde{A}_x(x,y,s)\right]_{z=0} = \frac{s\mu\varepsilon}{4\pi}\int_{\zeta'=-L/2}^{L/2}\tilde{I}(\zeta') \cdot \left[z_c \cos\alpha + (x - x_c)\cos\nu\right]\tilde{g}_1(x,y;\zeta')\,d\zeta' \tag{4.4}$$

The kernel term $\tilde{g}_1$ in (4.3) and (4.4) is given by

$$\tilde{g}_1(x,y;\zeta') = -\left(\frac{\gamma}{D^2} + \frac{1}{D^3}\right)e^{-\gamma D} \tag{4.5}$$

$$D = \left[[x - (x_c + \zeta' \cos\alpha)]^2 + [y - (y_c + \zeta' \cos\beta)]^2 + [z_c + \zeta' \cos\nu]^2\right]^{\frac{1}{2}} \tag{4.6}$$

and the current on the wire $\tilde{I}(\zeta')$ is assumed to be directed along unit vector $\vec{i}$ along the wire axis, and

$$\vec{i} = \cos\alpha \; \vec{i}_x + \cos\beta \; \vec{i}_y + \cos\nu \; \vec{i}_z \tag{4.7}$$

Based on the expression (1.16), satisfying the boundary condition on the wire, one obtains the following integral equation

$$\left(\frac{\partial^2}{\partial\zeta^2} - \gamma^2\right) \int_{\zeta'=-L/2}^{L/2} \tilde{I}(\zeta') \, \tilde{K}(a,\zeta,\zeta') \, d\zeta' - \gamma^2(2\cos^2\nu - 1) \cdot \int_{\zeta'=-L/2}^{L/2} \tilde{I}(\zeta') \, \tilde{g}(\zeta,\zeta') \, d\zeta' - \frac{\partial}{\partial\zeta} \int_{\zeta'=-L/2}^{L/2} \frac{\partial}{\partial\zeta'} \tilde{I}(\zeta') \, \tilde{g}(\zeta,\zeta') \, d\zeta'$$

$$= 4\pi s \left[\frac{\partial}{\partial z} \tilde{A}_{m_x}(\zeta) \cos\beta - \frac{\partial}{\partial z} \tilde{A}_{m_y}(\zeta) \cos\alpha + \left(\frac{\partial}{\partial x} \tilde{A}_{m_y}(\zeta) - \frac{\partial}{\partial y} \tilde{A}_{m_x}(\zeta)\right) \cos\nu\right]$$

$$\text{on the wire} \tag{4.8}$$

where

$$\tilde{K}(a,\zeta,\zeta') = \frac{1}{2\pi} \int_{-\pi}^{\pi} \frac{e^{-\gamma r_s}}{r_s} \, d\psi \tag{4.9}$$

$$r_s = [(\zeta - \zeta')^2 + 4a^2 \sin^2 \tfrac{\psi}{2}]^{\frac{1}{2}} \tag{4.10}$$

and

$$\tilde{g}(\zeta,\zeta') = \frac{e^{-\gamma r_m}}{r_m} \tag{4.11}$$

$$r_m = [4z_c^2 + 4z_c(\zeta + \zeta') \cos\nu + 4\zeta\zeta' \cos^2\nu + (\zeta - \zeta')^2]^{\frac{1}{2}} \tag{4.12}$$

In fact the integral expressions (4.1), (4.2), and (4.8) form the coupled-coupled set of equations in terms of the unknown magnetic current distribution in the aperture and unknown induced electric current on the finite wire. Practically, one resorts to the numerical procedures in order to obtain solutions for the problem. Let us consider a further specialization of the problem under study, and make the rectangular aperture to be a narrow slot of finite length and orient the wire to be parallel to the screen containing the narrow slot.

B. Finite Wire Parallel to the Plane and Behind the Narrow Slot

This particular case introduces a simplification of the integral expressions (4.1) and (4.8). The integral expression (4.2) can be ignored for narrow slot since we have only the axial magnetic current distribution. Further the wire is parallel to screen so that $\cos\nu = 0$ and the z-component of the magnetic vector potential $\tilde{A}_z$ does not exist. Substituting the distribution for the narrow slot defined in (2.12) and (2.13), we have the following integral equations for the coupled problem of the finite length wire parallel and behind the narrow slot in a perforated conducting screen:

$$\left(\frac{\partial^2}{\partial x^2} - \gamma^2\right)\int_{x'=-\ell/2}^{\ell/2} \tilde{m}(x')\,\tilde{K}(x-x',\tfrac{w}{4})\,dx' + \frac{1}{2}\,s\mu z_c \cos\beta \int_{\zeta'=-L/2}^{L/2}$$

$$\cdot\ \tilde{I}(\zeta')\,\tilde{G}(R_1)\,d\zeta' = -\,2\pi s\mu\, H_x^i(x) \quad \text{on slot axis} \qquad (4.13)$$

$$-2s\varepsilon z_c \cos\beta \int_{x'=-\ell/2}^{\ell/2} \tilde{m}(x')\,\tilde{G}(D_1)\,dx' + \left(\frac{\partial^2}{\partial \zeta^2} - \gamma^2\right)\int_{\zeta'=-L/2}^{L/2}$$

$$\cdot\ \tilde{I}(\zeta')[\tilde{K}(\zeta-\zeta',a) - \tilde{K}(\zeta-\zeta',2z_c)]\,d\zeta' = 0 \quad \text{on wire} \qquad (4.14)$$

In the above equations, the kernel terms are

$$\tilde{K}(\zeta,a) = \frac{1}{2\pi}\int_{\psi=-\pi}^{\pi} \frac{e^{-\gamma r_1}}{r_1}\,d\psi \qquad (4.15)$$

$$r_1 = [\zeta^2 + 4a^2 \sin^2 \tfrac{\psi}{2}]^{\frac{1}{2}} \qquad (4.16)$$

$$\tilde{G}(R_1) = \left[\frac{1}{R_1^3} + \frac{\gamma}{R_1^2}\right] e^{-\gamma R_1} \tag{4.17}$$

$$R_1 = \left[[x - (x_c + \zeta' \cos\alpha)]^2 + [y_c + \zeta' \cos\beta]^2 + z_c^2\right]^{\frac{1}{2}} \tag{4.18}$$

$$D_1 = \left[[(x_c + \zeta\cos\alpha) - x']^2 + [y_c + \zeta\cos\beta]^2 + z_c^2\right]^{\frac{1}{2}} \tag{4.19}$$

In the integral expression (4.13), the component $\tilde{H}_x^i$ is the incident magnetic field in the illuminated side $z < 0$, with electric vector polarized transverse to the slot axis, and if θ is the angle which the direction of propagation of the incident field makes with the axis of the slot, then $\tilde{H}_x^i(x)$ can be written for a plane wave as,

$$\tilde{H}_x^i(x) = \tilde{H}_{xo}^i \sin\theta \; e^{-\gamma\cos\theta x} \tag{4.20}$$

$\tilde{H}_{xo}^i$ is the amplitude factor of the plane wave.

C. Numerical Results

The integral equations (4.13) and (4.14) can be solved based on the method of moments[16] and representative results for the coupled geometry, figure 4.1, is shown in figures 4.2 and 4.3 for a narrow slot of length $\ell = \lambda/2$, width $w = \lambda/20$ in the presence of a finite length wire of length $L = \lambda/2$ and radius $\lambda/1000$. The wire is parallel to the screen containing the narrow slot with its center at $(x_c, y_c, z_c) = (0, 0, \lambda/4)$. The incident field is normal on the narrow slot. In figure 4.2 is indicated the wire current for various values of $\cos\beta$, where $\beta = 0$ corresponds to maximum coupling between slot and wire and $\beta = 90^\circ$ give zero coupling in which case axis of the wire is parallel to the axis of the narrow slot. In figure 4.3, is indicated the slot axial magnetic current distribution for various values of $\cos\beta$. One notes the changes in the magnitude and distribution of the slot field due to reflection of the wire back to the slot. The results of figures 4.2 and 4.3 are extended in figures 4.4 and 4.5 respectively as a function of

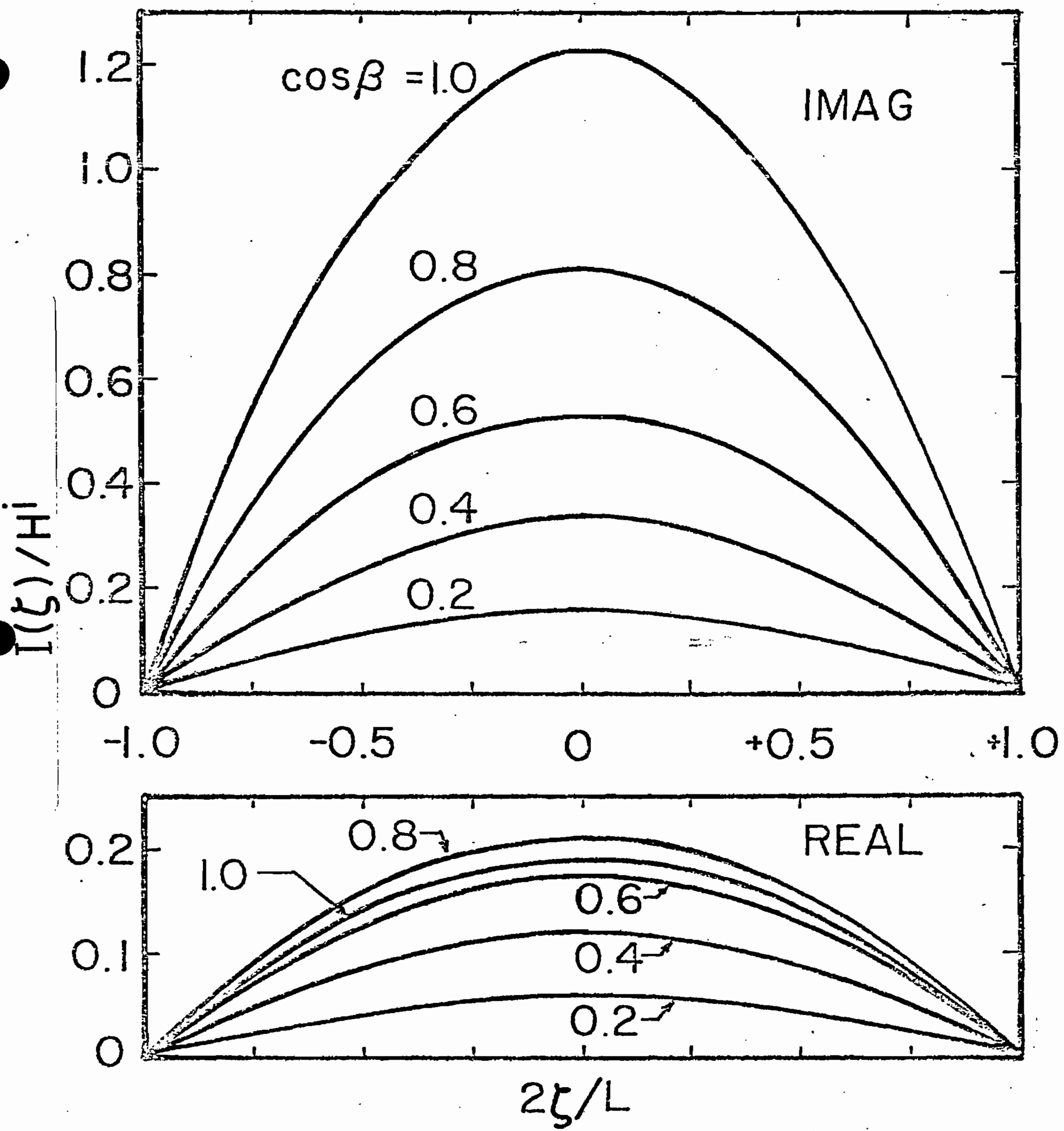

Figure 4.2 Electric Current Distribution on Finite Wire Scatterer in the Presence of Slot, L=0.5, a=0.001, ℓ=0.5, w=0.05, (x_c,y_c,z_c)=(0,0,0.5) at Frequency 300 MHz

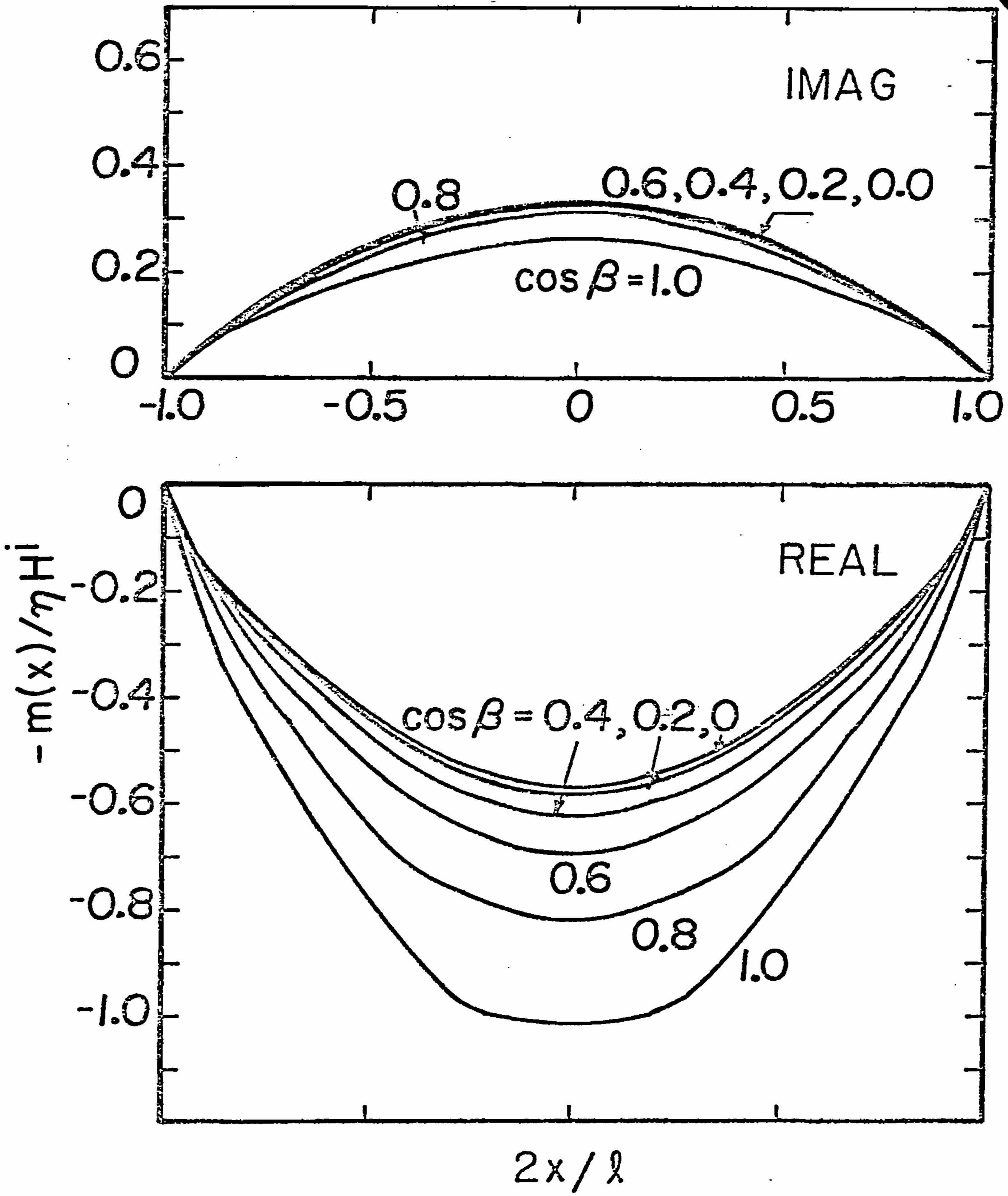

Figure 4.3 Axial Magnetic Current Distribution in a Narrow Slot in the Presence of Wire, L=0.5, a=0.001, ℓ=0.5, w=0.05, $(x_c, y_c, z_c)=(0,0,0.5)$ at Frequency 300 MHz

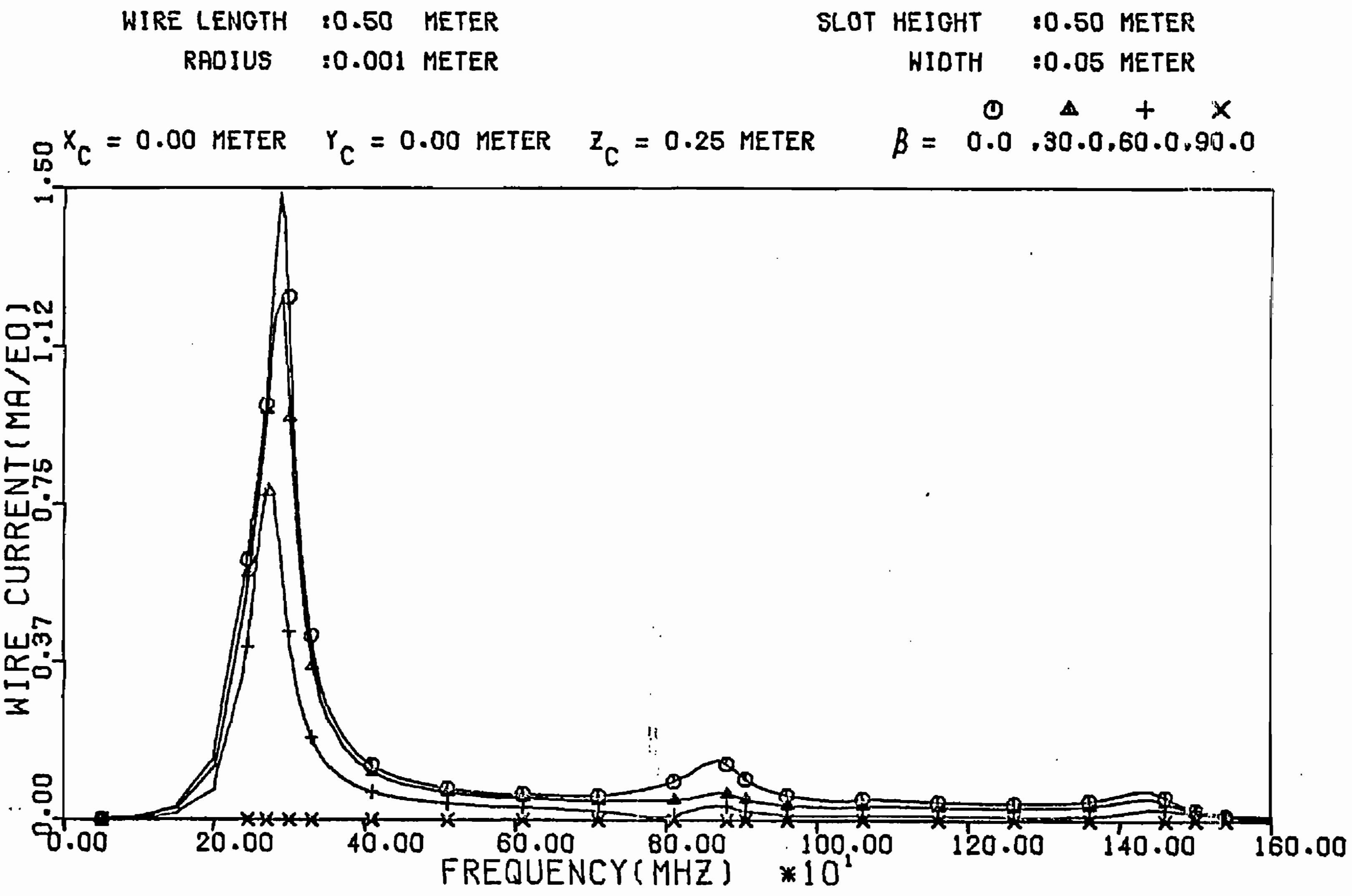

Figure 4.4 Electric Current on Finite Wire at Its Center in the Presence of Slot as a Function of Frequency

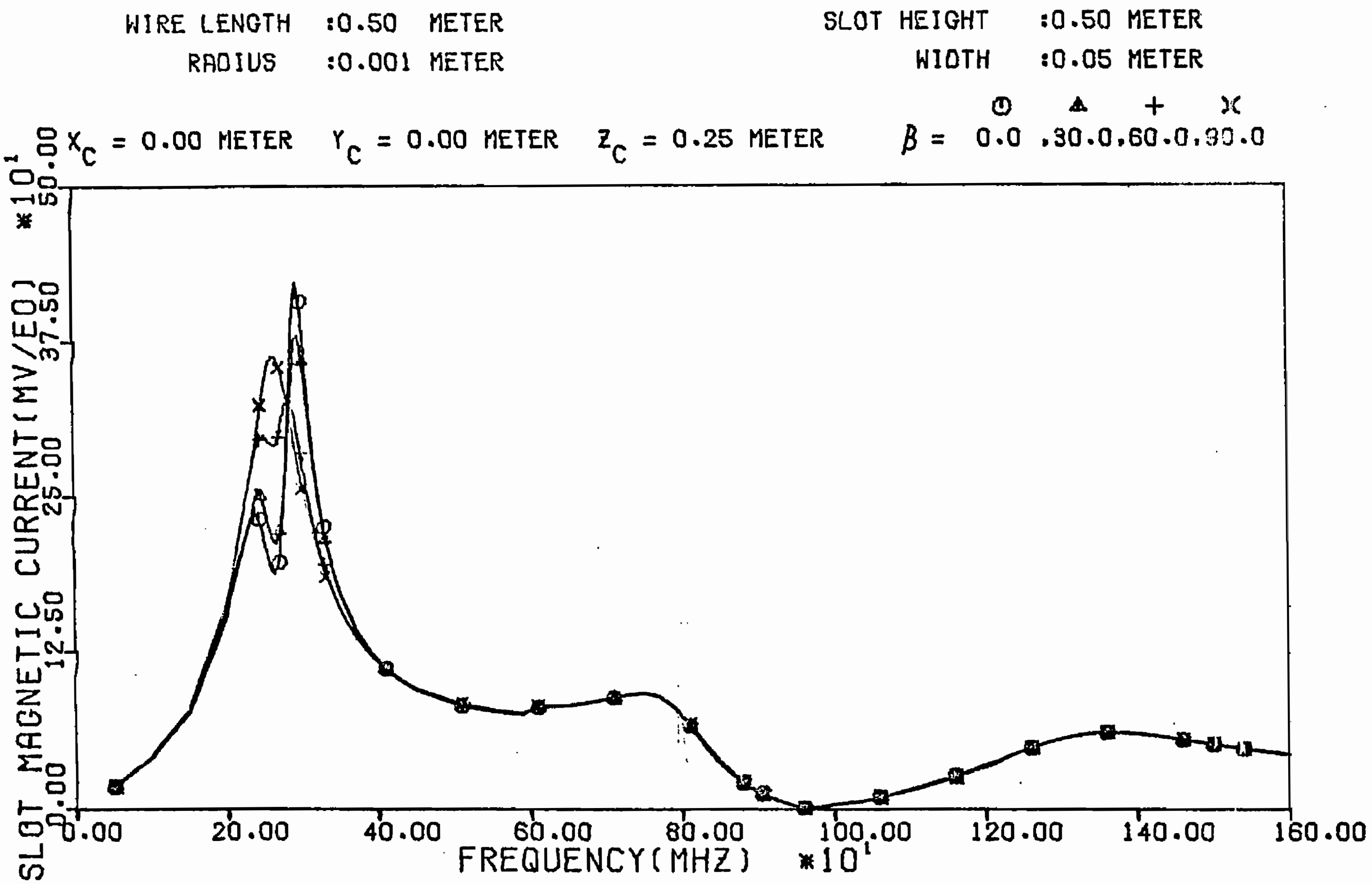

Figure 4.5 Axial Magnetic Current in Narrow Slot at Its Center in the Presence of Wire as a Function of Frequency

frequency. The case of $\beta = 90^o$ in figure 4.4 is an uncoupled case and no currents are induced on the wire. The frequency responses of wire and also that of narrow slot do exhibit peaks corresponding to their natural resonant frequencies which actually are a basis for SEM characterization as discussed in Chapter I.

D. SEM Characterization

The general formalism of SEM[2,18,19] in regard to parameterization and subsequent transient characterization is briefly discussed in Chapter I, expressions (1.30) to (1.35). Accordingly, one can determine the complex natural frequencies, modal current distributions, coupling vectors and coupling coefficients. Even though this approach seems to be a direct numerically oriented procedure, care should be exercised and the problem should be analyzed step by step.

(i) Natural resonance of narrow slot

Suppose the finite length wire is completely removed, and we have only an isolated narrow slot, the equation to be analyzed is comparatively simple one, expression (2.14). There exists only axial distribution of the magnetic current, and numerically the expression (2.14) is efficient to analyze. Based on the condition (1.31), the natural frequencies or poles of the isolated narrow slot can be determined. In figure 4.6 is indicated the location of few of the poles in the complex s plane for the narrow slot dimension $\ell/w = 20$. In fact, they exist in complex conjugate pairs and only the upper half ones are shown. These natural resonant frequencies lie in layers parallel to the $j\omega$-axis. The layer very close to the $j\omega$-axis is very important in the sustained transient responses. Suppose the slot dimension ratio w/ℓ is increased; the poles close to the $j\omega$-axis move away from the $j\omega$-axis exhibiting the damping behavior associated with the radiation of the slot. In figure 4.7 is shown the pole trajectory of s_{11}, the first-layer first pole close to the $j\omega$-axis as a function of w/ℓ. It is also academic at this stage to look at resonances of an isolated thin

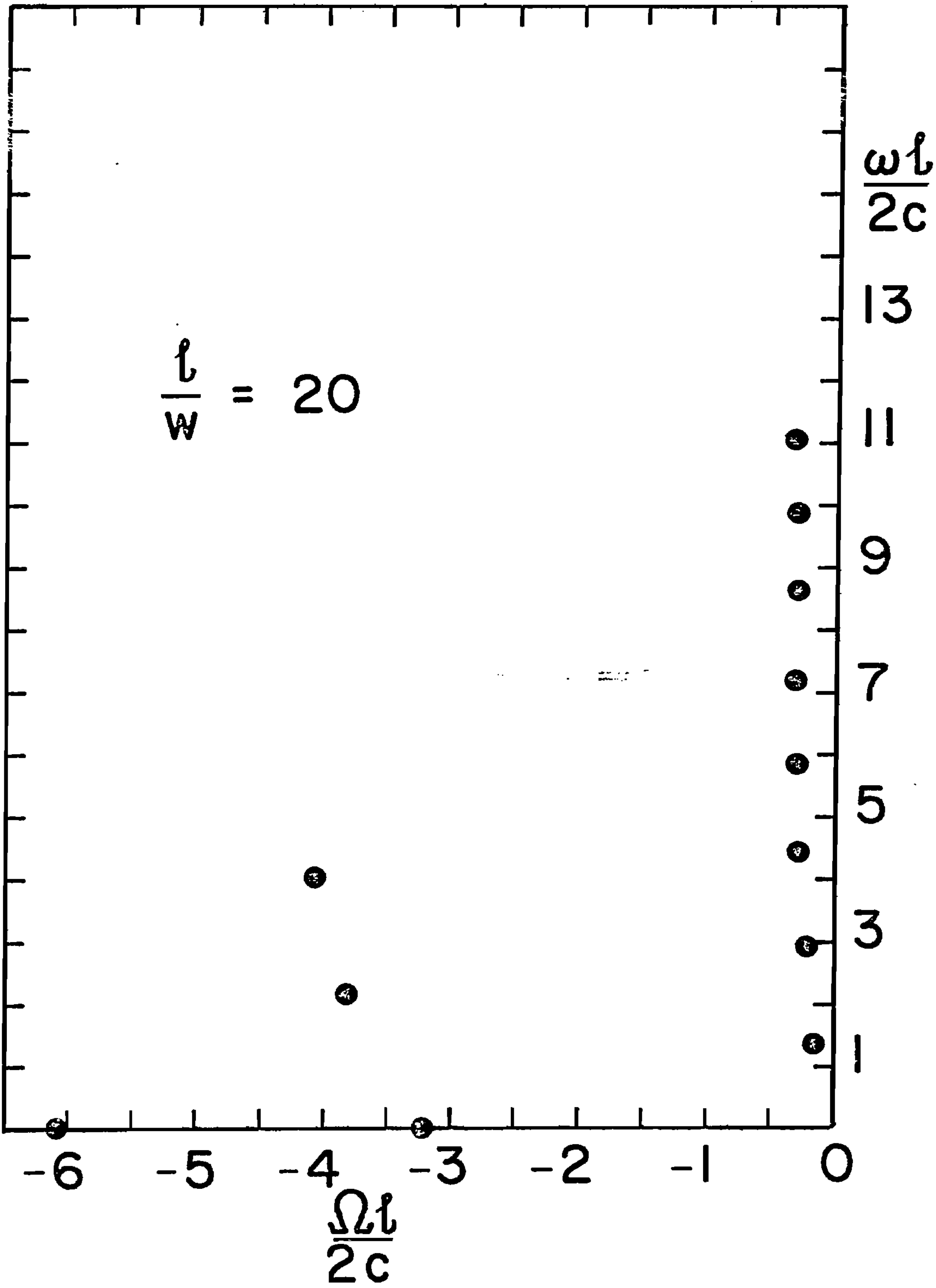

Figure 4.6 Natural Resonance of Isolated Narrow Slot, $\ell=2$, w=0.1

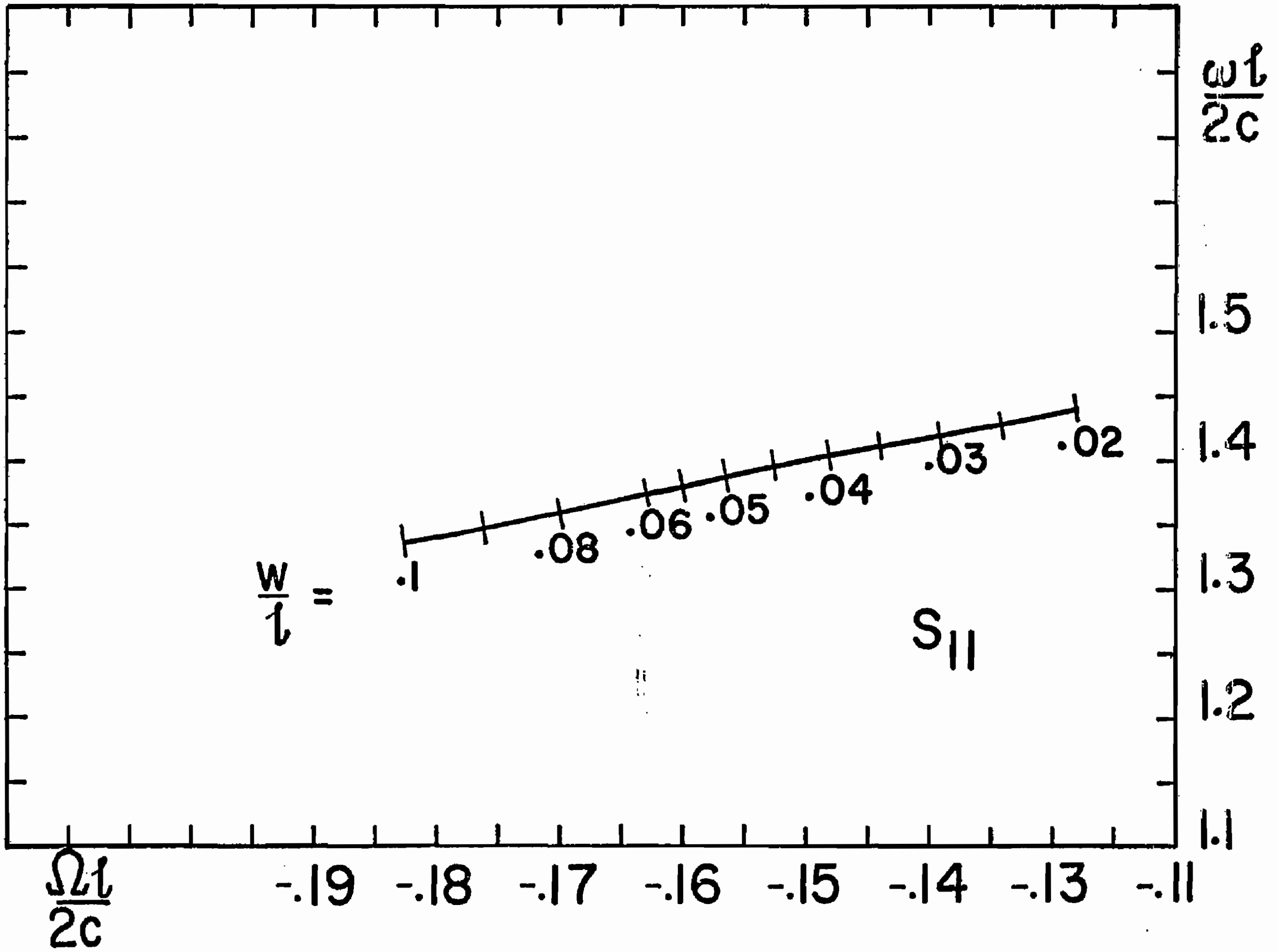

Figure 4.7 Trajectory of s_{11} as a Function of w/ℓ of Isolated Narrow Slot

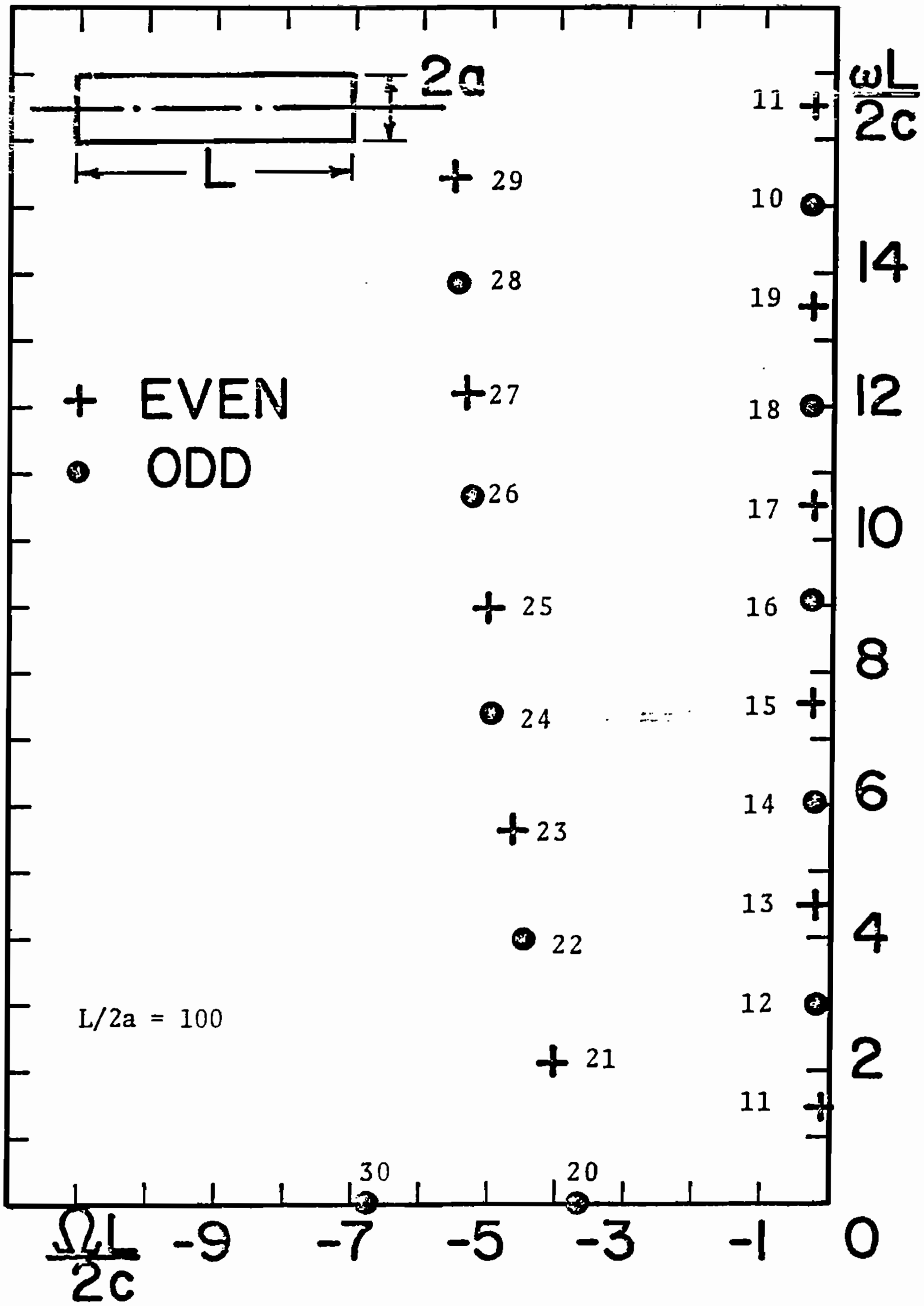

Figure 4.8 Natural Resonance of Isolated Finite Wire, L=2, a=0.01

finite wire.[18] After all, the integral equation (2.14) is the dual of the integral equation for a narrow strip of same dimensions, and further there exists equivalence between the narrow strip and thin finite wire. If the radius of the wire $a = \frac{w}{4}$, the resonances of the narrow slot are the same as its dual narrow strip and that of a finite thin wire of radius a. In figure 4.8 is shown the various pole locations[18] for an isolated finite thin wire. Thus one can also look into various trajectory plots of finite wire as a function of radius, to estimate the actual resonances of the narrow slot.

(ii) Natural resonance of finite wire over ground plane

We shall now consider a finite thin wire placed parallel and above a ground screen[18] with no perforated slot. This particular problem is the special case of a more general problem of coupling between two finite wires in free space as indicated in figure 4.9, wherein two finite thin wires of lengths L_p and L_q, radii a_p and a_q are oriented in YZ at an angle ν with respect to their axis. The mutual coupling between the two wires can be studied based on the integral equation (3.12), and forming the matrix equation by applying method of moments. This procedure yields a generalized system partitioned matrix of two by two,

$$[Z_{pq}] = \begin{bmatrix} [S_p] & [C_p^q] \\ [C_q^p] & [S_q] \end{bmatrix} \tag{4.21}$$

where $[S_p]$ and $[S_q]$ are the self-partitioned matrices of p^{th} and q^{th} wires and, $[C_p^q]$ and $[C_q^p]$ are the mutual partitioned matrices corresponding to the coupling between the p^{th} and q^{th} wires. Based on the condition (1.31) the determinant of (4.21) gives the natural resonances; we expect to obtain the perturbed self-natural resonances of the p^{th} wire, the self-natural resonances of the q^{th} wire and also the mutual natural resonances between the p^{th} and q^{th} wires.

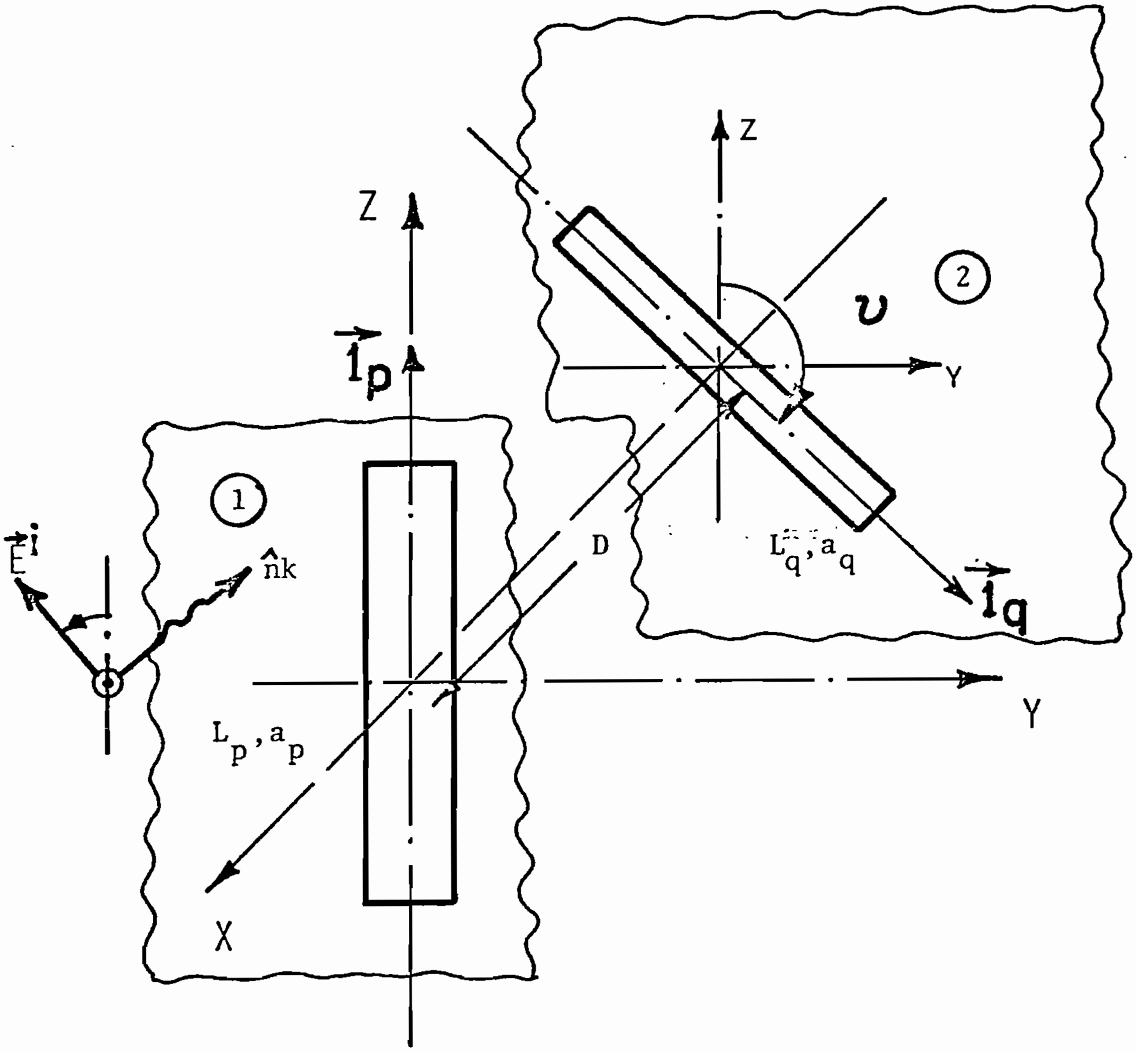

Figure 4.9 Geometry of Two Coupled Wires

These mutual resonances are in fact dependent on the relative orientation $\vec{1}_p \cdot \vec{1}_q$ of the two wires and the distance D apart. The coupling between the two wires is maximum when they are parallel and minimum or completely uncoupled when they are perpendicular. Particularly when their axes are parallel one has two different problems, viz., introducting either a perfect electric ground plane (anti-symmetric case) or a perfect magnetic ground plane (symmetric case) with respect to the distribution of the induced electric current is concerned.

In figure 4.10 is shown the trajectory of the first natural resonance close to $j\omega$ - axis as a function of the angle ν between the axes of the two wires, p^{th} and q^{th}. When their axes are perpendicular, they are uncoupled and have their own self-resonances. But if the wires are identical their individual self-resonances coincide as indicated in figure 4.10 for $\nu = 90^o$. As ν is varied, for every ν there exists two poles corresponding to the symmetric and the anti-symmetric modes the wires can support. The extreme case $\nu = 180^o$ gives poles of the wire above the electric ground plane and also the wire above the magnetic ground plane. It is possible to split the determinant of the expression (4.21) so that poles can be categorized according to their types in the complex s-plane,

$$\begin{vmatrix} [S_p] & [C_p^q] \\ [C_q^p] & [S_p] \end{vmatrix} \equiv \underset{\substack{\text{Symmetric Case} \\ \text{(PMC)}}}{|\{[S_p] + [C_p^q]\}|} \cdot \underset{\substack{\text{Anti-Symmetric} \\ \text{Case}}}{|\{[S_p] - [C_p^q]\}|} \qquad (4.22)$$

Based on the expression (4.22), the anti-symmetric poles ($\nu = 180^o$ corresponds to the case of wire over the electric ground plane) are traced as a function of the angle ν. In figure 4.11, the first three trajectories of the poles close to the $j\omega$-axis are shown, for a fixed value of distance $D = 2.0$ between the two wires. For $\nu = 180^o$, the various natural resonances are obtained for the

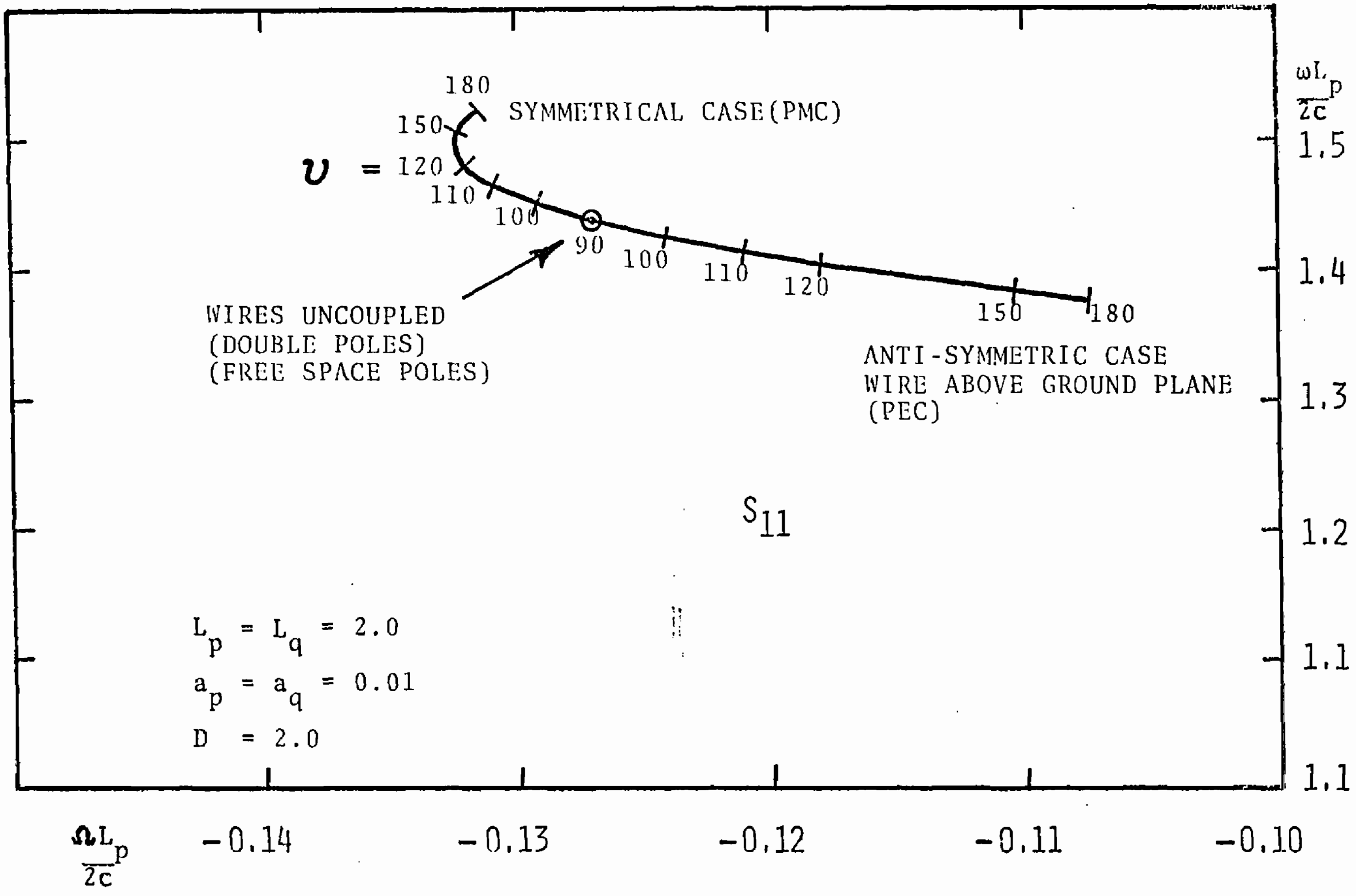

Figure 4.10 Trajectory of the First Set of Poles s_{11} as a Function of ν

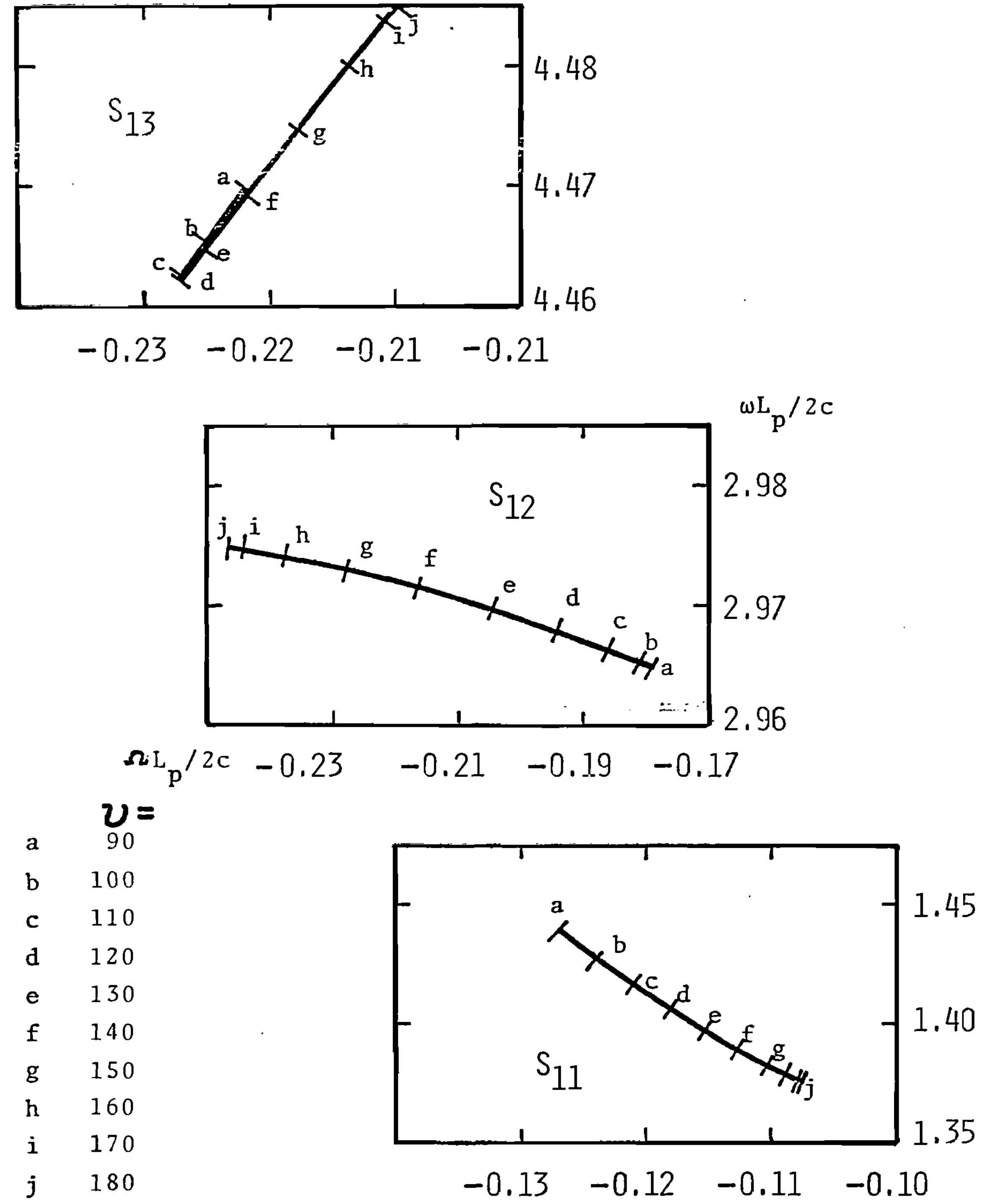

	$\nu =$
a	90
b	100
c	110
d	120
e	130
f	140
g	150
h	160
i	170
j	180

Figure 4.11 Trajectory of the First Three Anti-Symmetry Poles s_{11}, s_{12}, and s_{13} as a Function of ν

wire over a perfect electric ground plane (with no perforated narrow slot) and are shown in figure 4.12. The layer close to the jω-axis represents the self-resonances and these are in a way similar to the isolated case, figure 4.8, but are slightly perturbed from their position depending upon their distance above the ground plane. The location of the poles shown in other layers correspond to the mutual interaction with respect to the ground plane or with respect to the image of the wire. The trajectory of the s_{11} first pole close to the jω-axis as a function of distance over the ground plane is shown in figure 4.13, where the trajectory spirals[18] around the pole of the isolated case and takes off when a pole from the other layer enters into the path. This repeats[18] so that there exists always only one pole in the trajectory near s_{11}.

One can best explain the mutual interaction effects depending upon whether the incident field excites a particular natural mode or not. This is depicted in coupling coefficients[2] and referring to the expression (1.30) the coupling coefficient for a particular mode α is given by

$$C_\alpha = \beta_\alpha [\tilde{\nu}]_\alpha \cdot [\tilde{\mu}]_\alpha^T \qquad (4.23)$$

For the two wire problem shown in figure 4.9, based on the expression (4.23), the coupling coefficient for the first pole s_{11} close to jω-axis are calculated as a function of the angle ν for a plane wave incident normally on the p^{th} wire. In figures 4.14 and 4.15 the coupling coefficients are plotted as a function of ν for the anti-symmetric pole and the symmetric pole, respectively. The results shown clearly exhibit the coupling of the incident field to the corresponding natural mode excited. With above natural resonance and coupling coefficient results, it is possible to construct the time domain response based on the expression (1.35), for the geometry of figure 4.16, a finite wire parallel to a ground plane. In figure 4.17 is shown the transient response of the

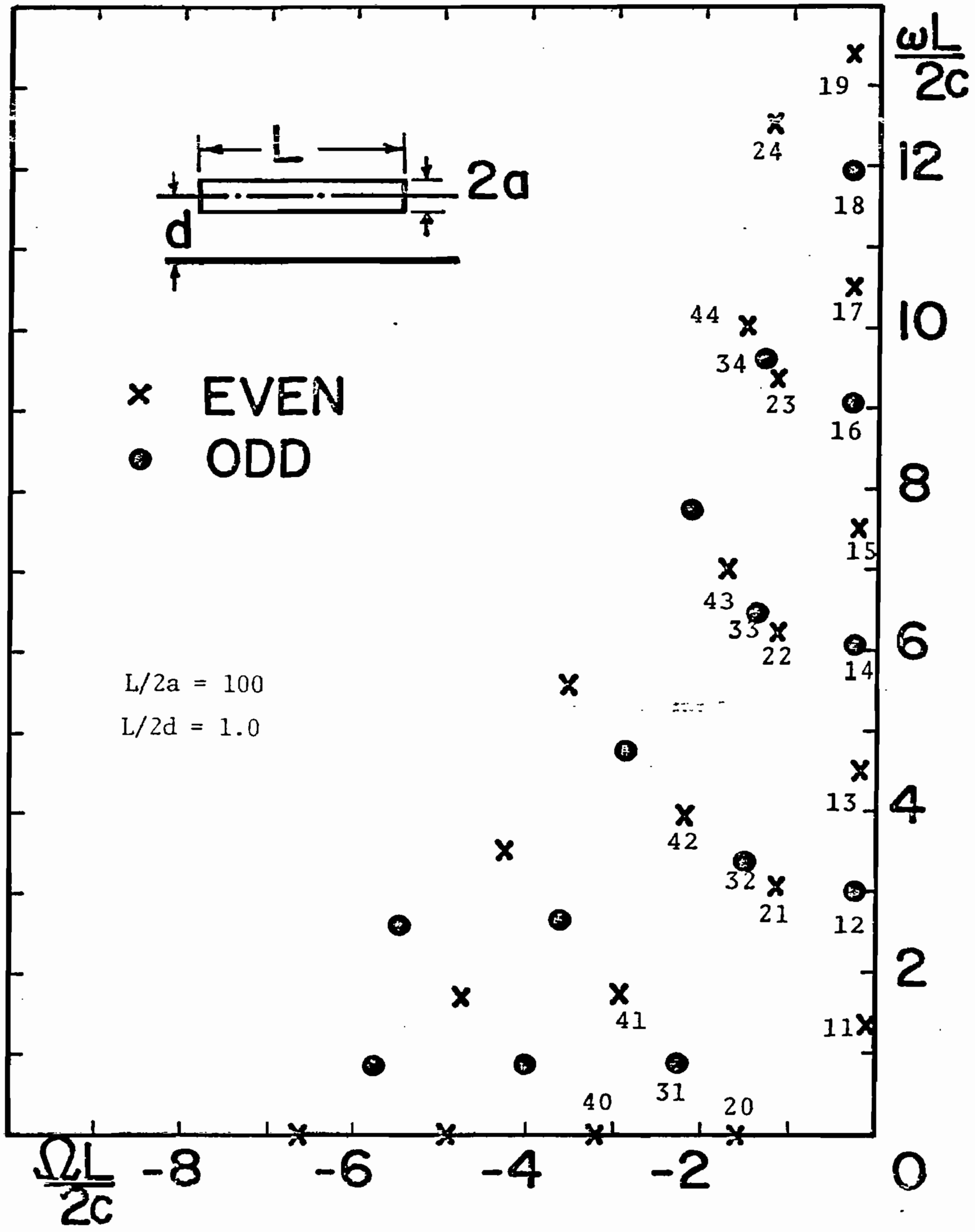

Figure 4.12 Natural Resonance of Finite Wire Placed Parallel Over a Perfect Electric Ground Plane

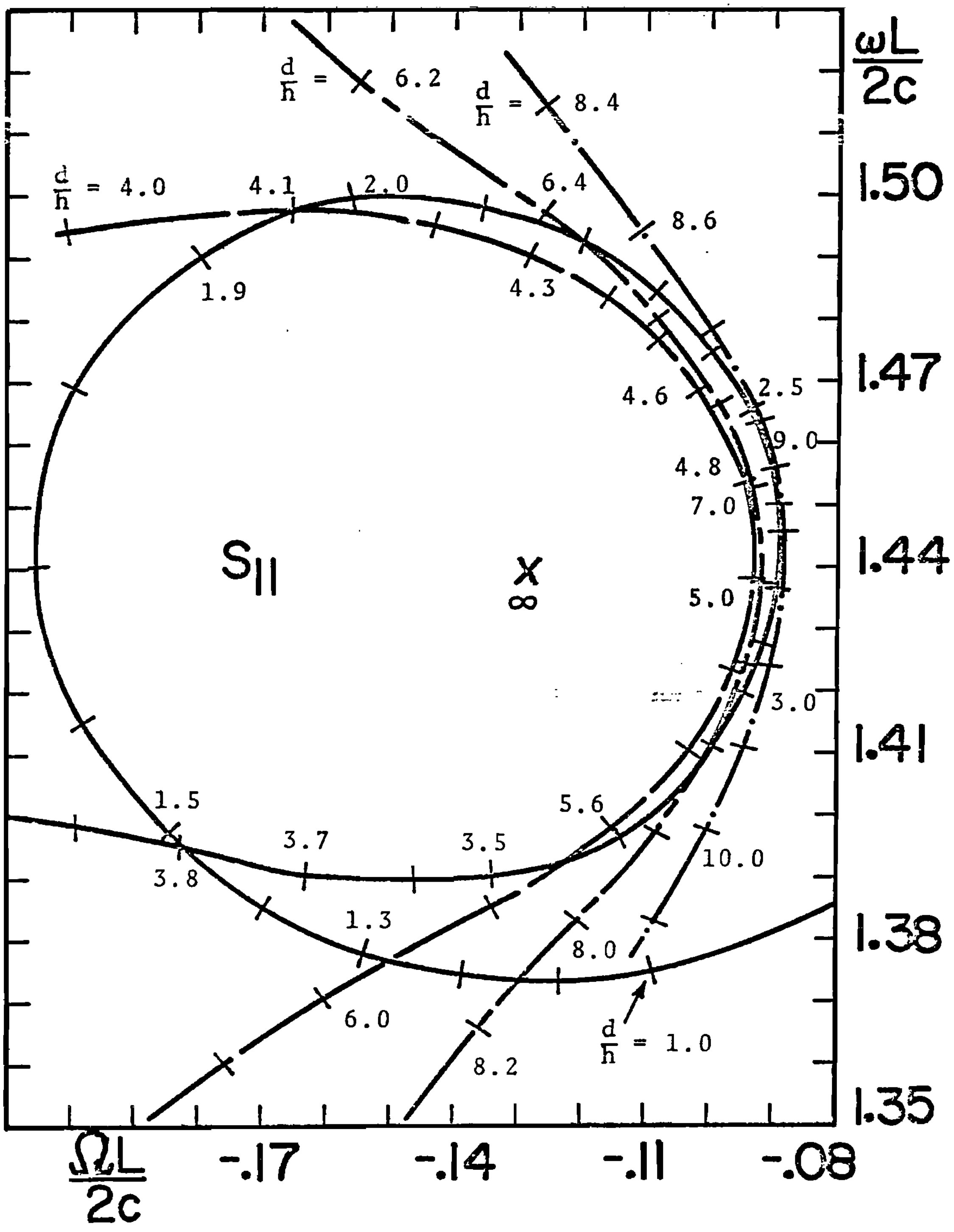

Figure 4.13 Trajectory of First Pole s_{11} as a Function of Distance Over the Ground Plane

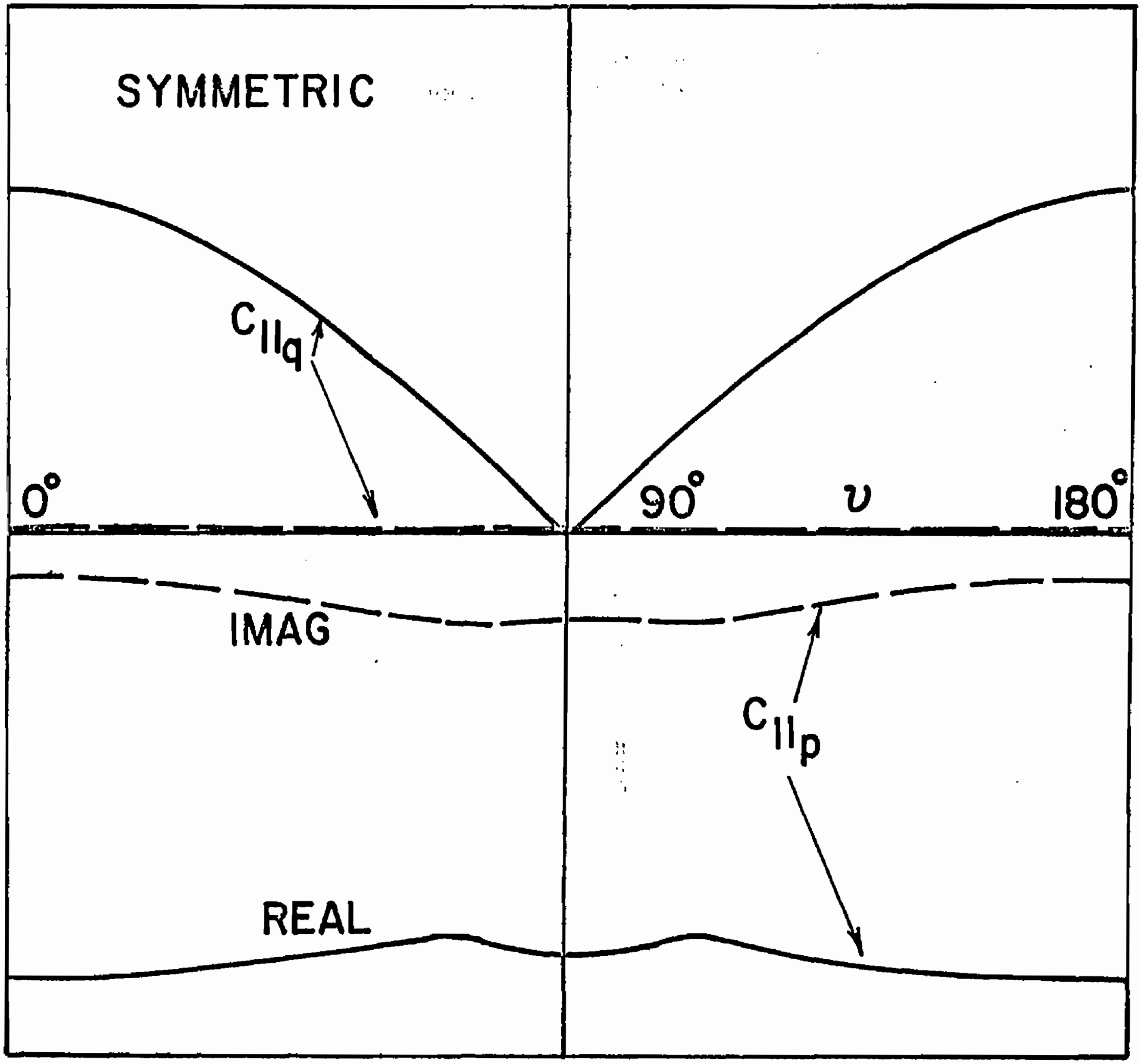

Figure 4.14 Coupling Coefficient Corresponding to First Symmetric Pole s_{11} as a Function of ν

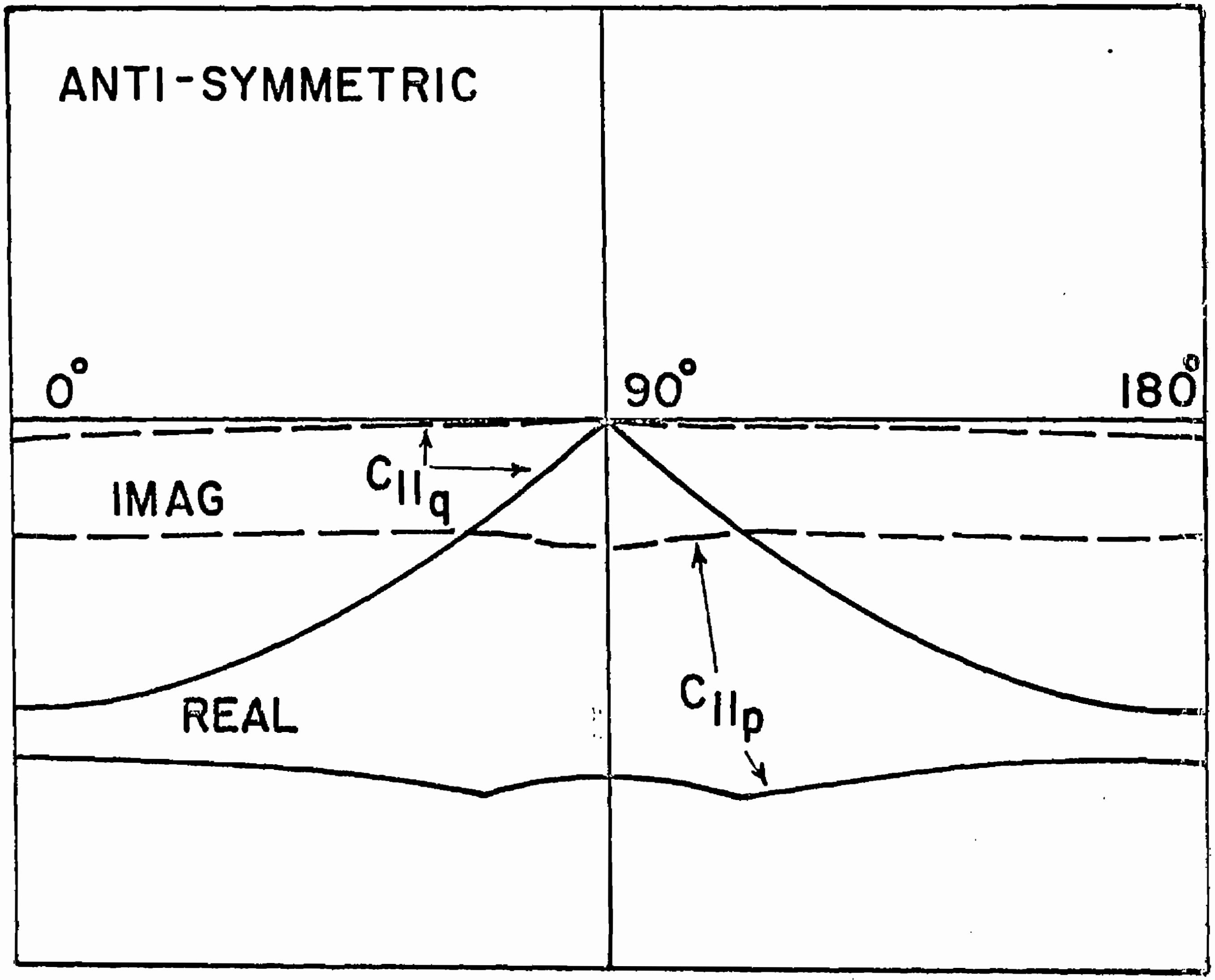

Figure 4.15 Coupling Coefficient Corresponding to First Anti-Symmetric Pole s_{11} as a Function of ν

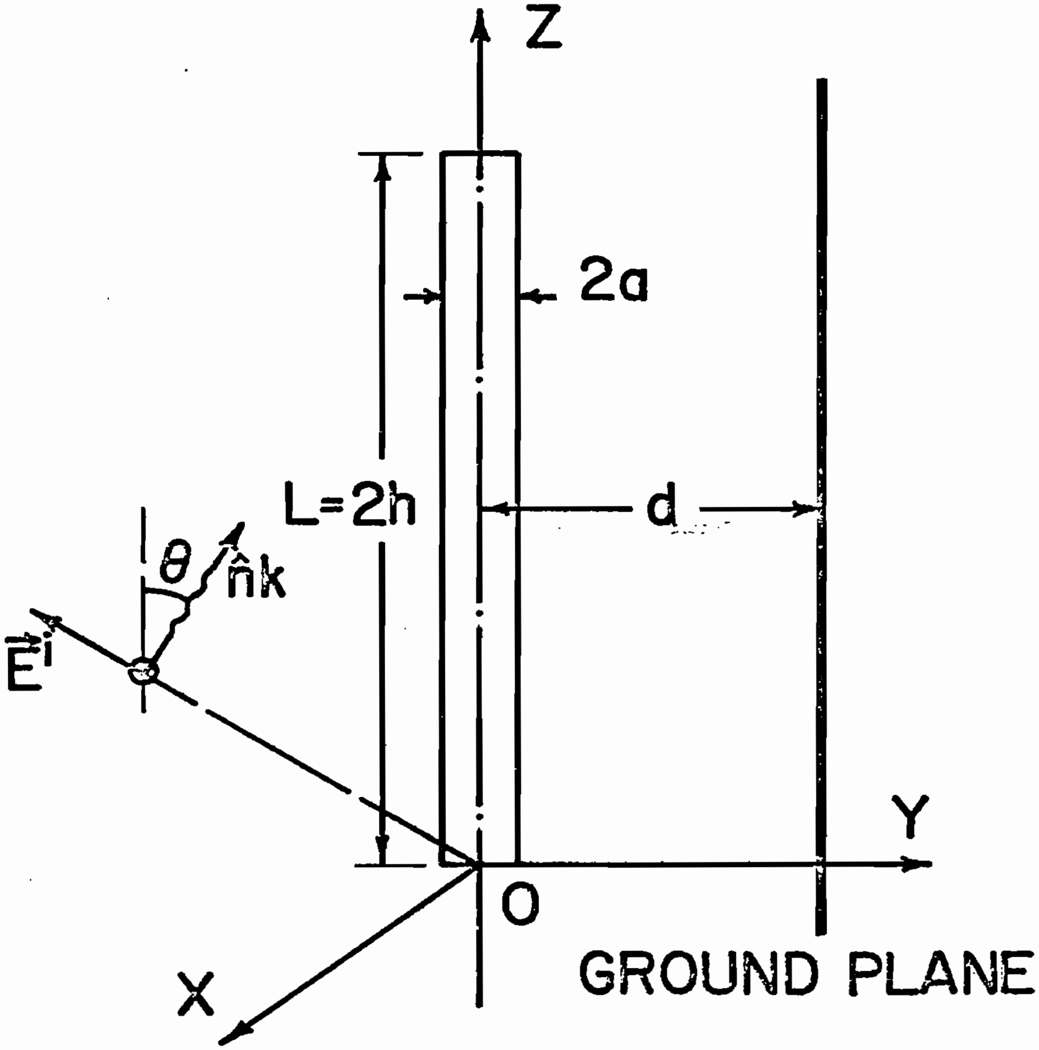

Figure 4.16 Geometry of Finite Wire Over Ground Plane with No Slot Perforated

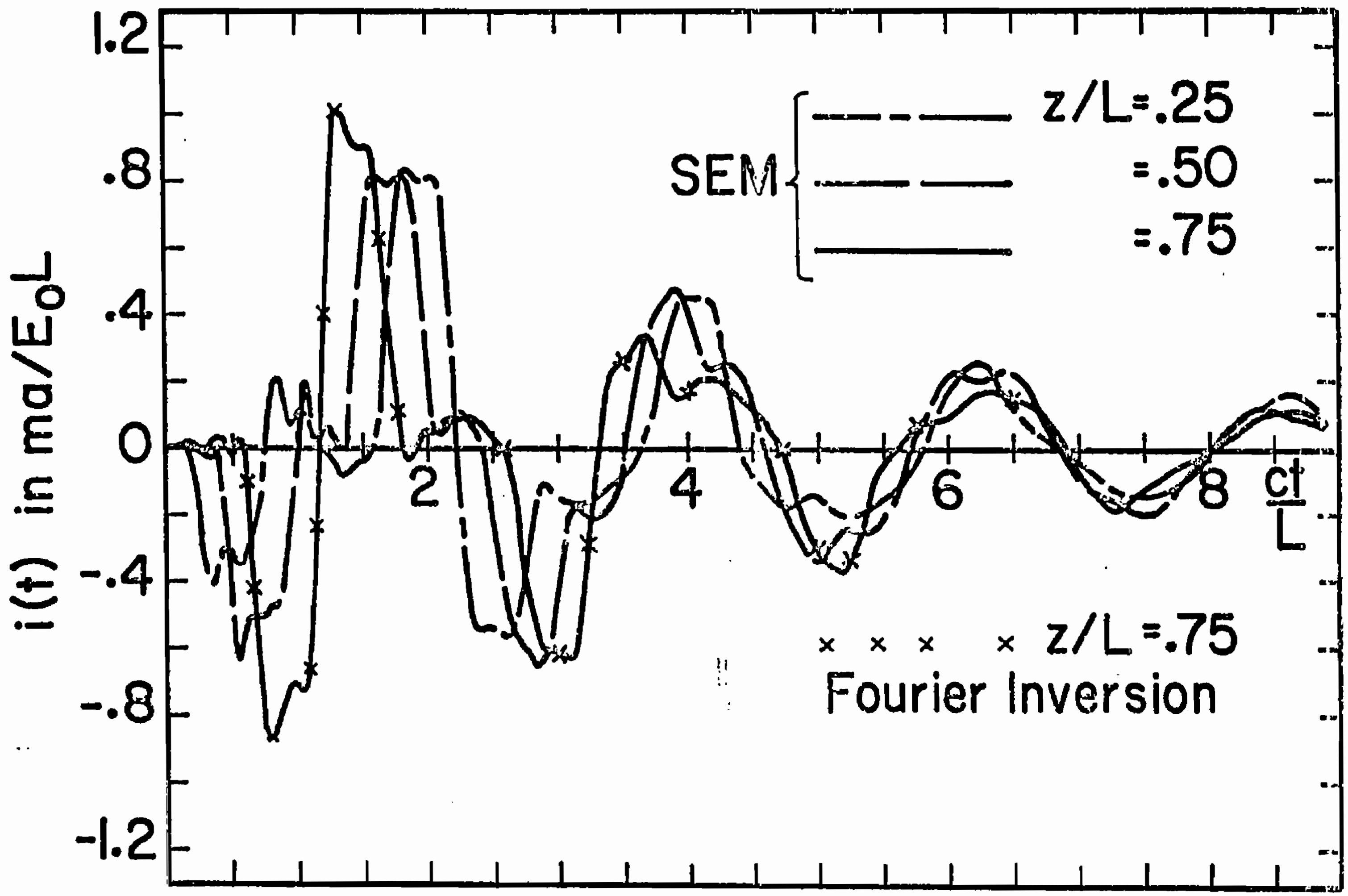

Figure 4.17 Time Domain Solution of Wire Over Ground Plane Based on SEM with Step Plane Wave Incident, t=0 at z=0

finite wire over the perfect electric ground plane, $\nu = 180^\circ$. The electric current induced is plotted as a function of time at different locations on the p^{th} wire for a step function plane wave incident at an angle of 30° to the axis of the wire. The delay in the initial response is obvious due to the delay of the step wave front excited by the wire. The time domain response gradually decays for large values of the time.

(iii) Finite wire scatterer behind a narrow-slot-perforated screen

Let us now return to the original problem of interaction with the finite wire behind a narrow slot perforated conducting screen, figure 4.1. The transient characterization and the corresponding natural resonance results obtained in section D-(i) for isolated narrow slot and in section D-(ii) for wire above ground plane are quite useful to understand and predict the results of the scatterer and narrow-slot interaction problem. Based on the coupled integro-differential equations (4.13) and (4.14), and further matrix formulation using the moment-method, a matrix equation similar to the expression (1.25) is first derived. Then the various natural resonances for the coupled geometry are obtained by numerically solving the determinant equation (1.31). For this coupled problem, the natural resonances can be separated into two parts. One set of natural resonances belongs to the narrow slot geometry in the presence of the wire scatterer and the other set belongs to the finite wire scatterer over the ground plane in the presence of the narrow slot. The first set of the natural resonant frequencies belonging to the narrow slot are similar to the ones depicted in the figure 4.6, but are perturbed from their locations depending on the orientation of the wire axis with respect to the slot and distance of the wire over the ground plane. The results of the pole plot shown in figure 4.6 are for the limiting uncoupled case of $\cos\beta = 0.0$. Similarly, the second set of natural resonant frequencies belong to the finite wire scatterer parallel and above the ground screen in the presence of the narrow slot are similar to the ones depicted in the figure 4.12, but are perturbed from their locations depending on the wire distance above the ground plane and the orientation of the wire axis with respect to the slot. The results of the figure 4.12 correspond to the uncoupled case $\cos\beta = 0.0$, so that for any other '$\cos\beta$' orientation of the wire with respect to the slot axis, the new location of the poles should be determined by solving the determinant of the partitioned matrix equation obtained from the equations (4.13) and (4.14).

In figure 4.18 is shown the natural resonant frequencies of the finite wire scatterer and narrow slot geometry, figure 4.1, for the maximum coupling $\cos\beta = 1.0$. Only the first four sets of the pole locations of the first layer close to $j\omega$-axis are indicated. The pole locations are indeed perturbed to the maximum extent from their uncoupled values. The trajectory of the first set of poles close to $j\omega$-axis are shown in figure 4.19 as a function of coupling factor $\cos\beta$. The poles of the finite wire over the ground plane move away from the $j\omega$-axis while that of narrow slot move toward the $j\omega$-axis as the coupling between the wire and the slot is gradually increased. Figure 4.20 gives the trajectory results for the second set of poles close to the $j\omega$-axis. Obviously the path of the trajectory indirectly explains the coupling between the wire and the slot, and the corresponding radiation characteristics involved.

In figures 4.21 through 4.24 are shown the transient response of the wire scatterer and the narrow slot interaction problem under discussion. For the results of figures 4.21 and 4.22 a step plane wave is assumed to excite the slot normally and the origin of the coordinate system is taken as time reference $t = 0$. The same results are repeated in figures 4.23 and 4.24 but with the following EMP incident normally on the narrow slot

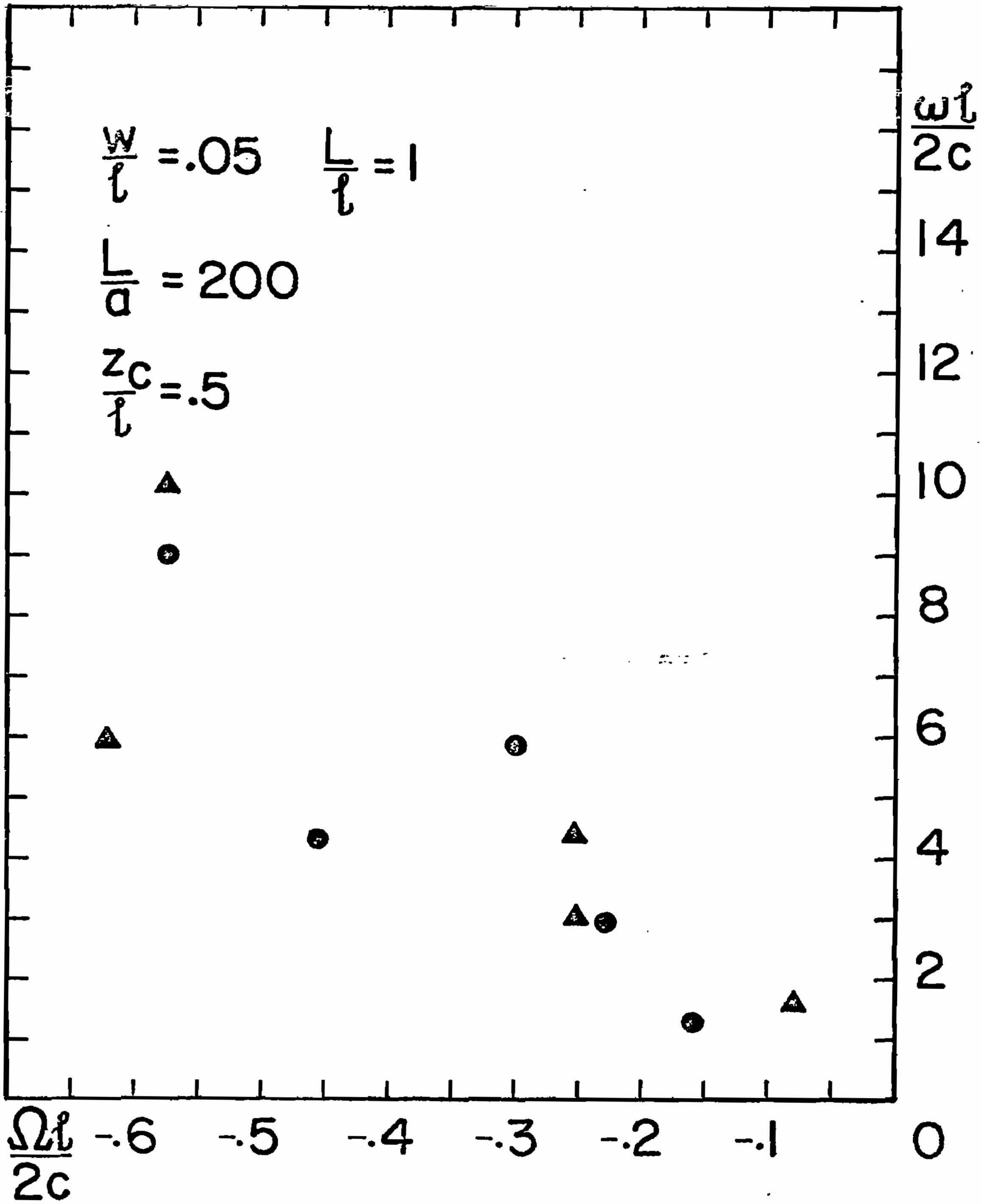

Figure 4.18 Natural Resonances of Finite Wire Behind a Narrow Slot Perforated Conducting Screen

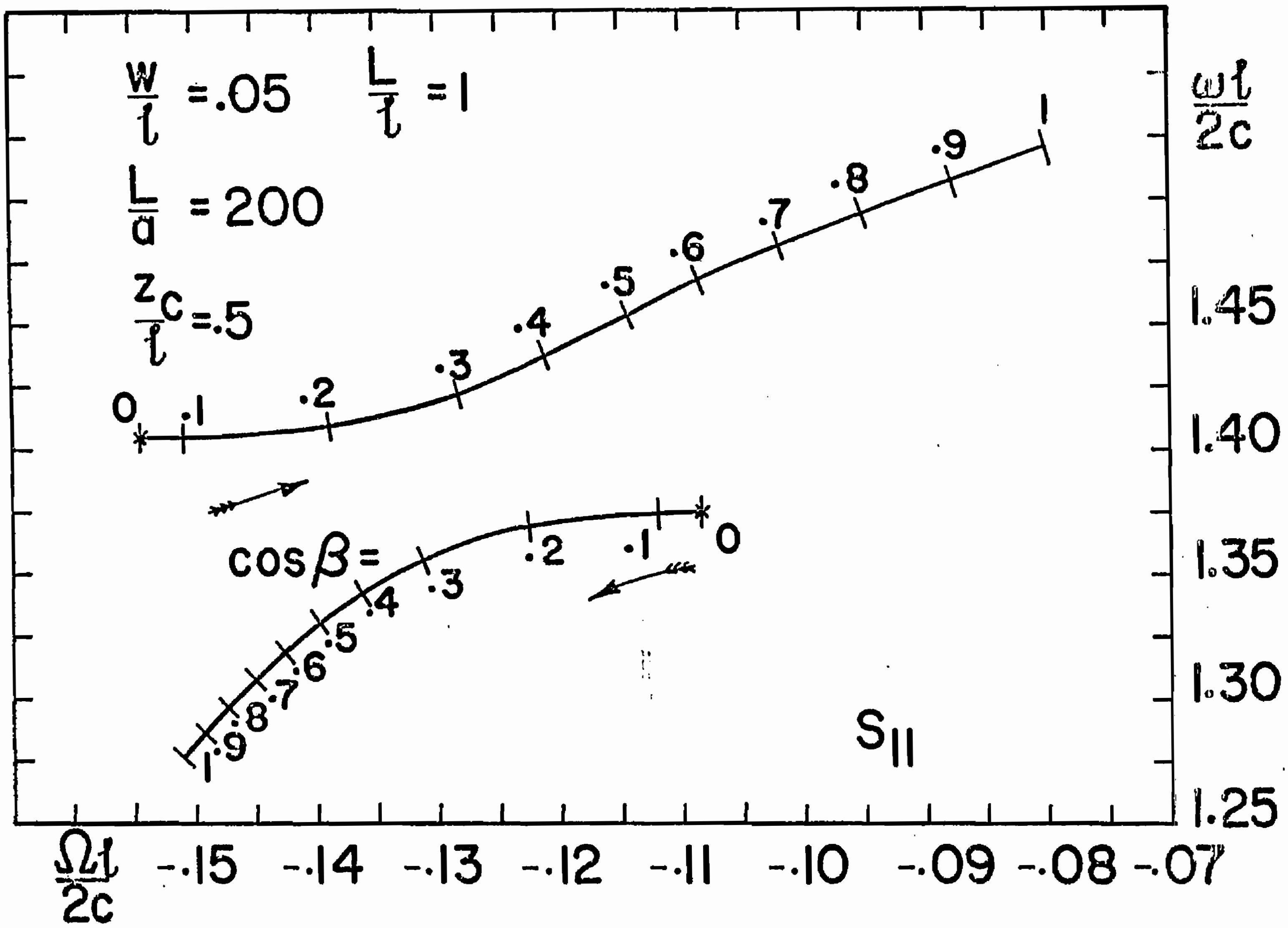

Figure 4.19 Trajectory of the First Set of Poles s_{11} as a Function of cosβ

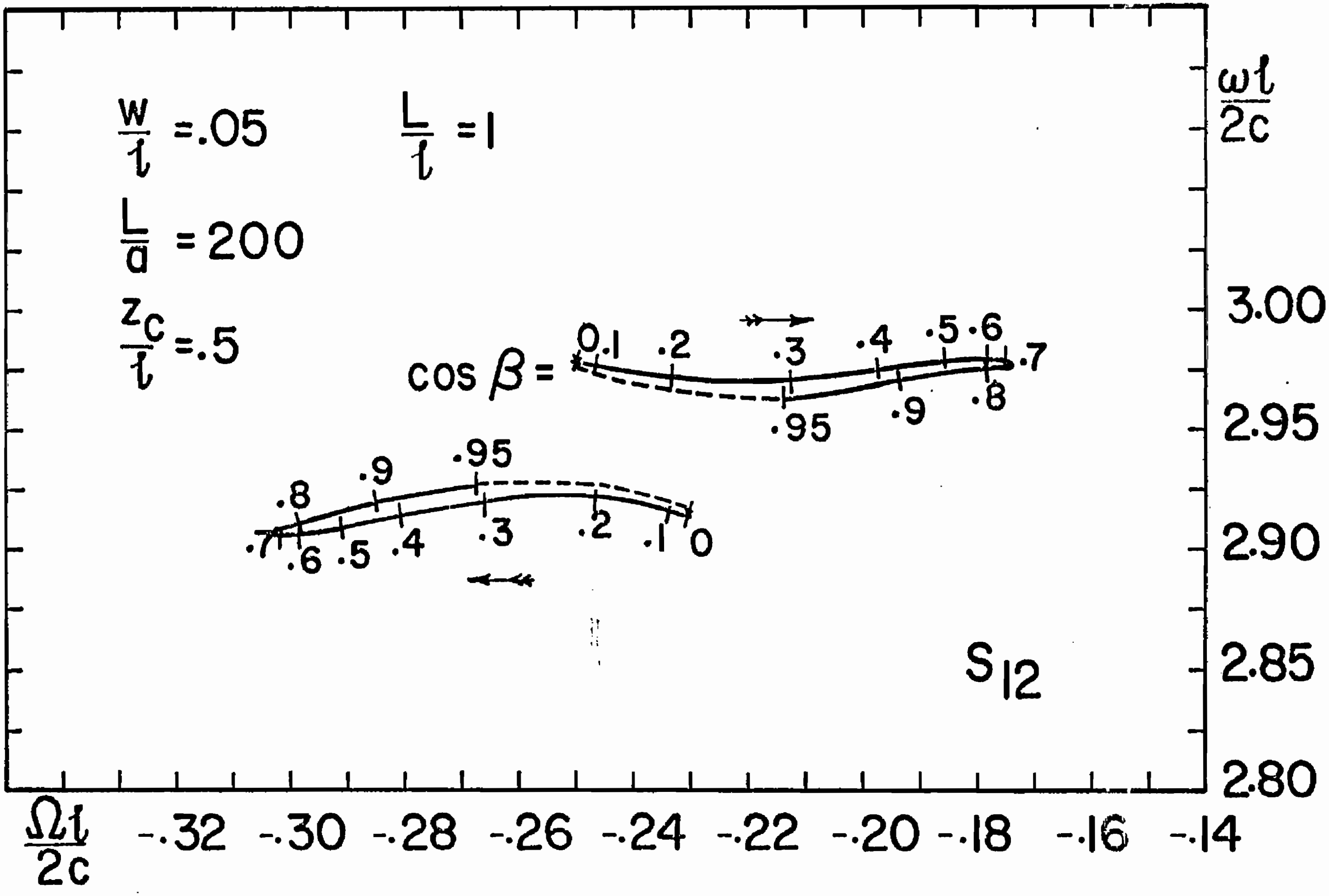

Figure 4.20 Trajectory of the Second Set of Poles s_{12} as a Function of cosβ

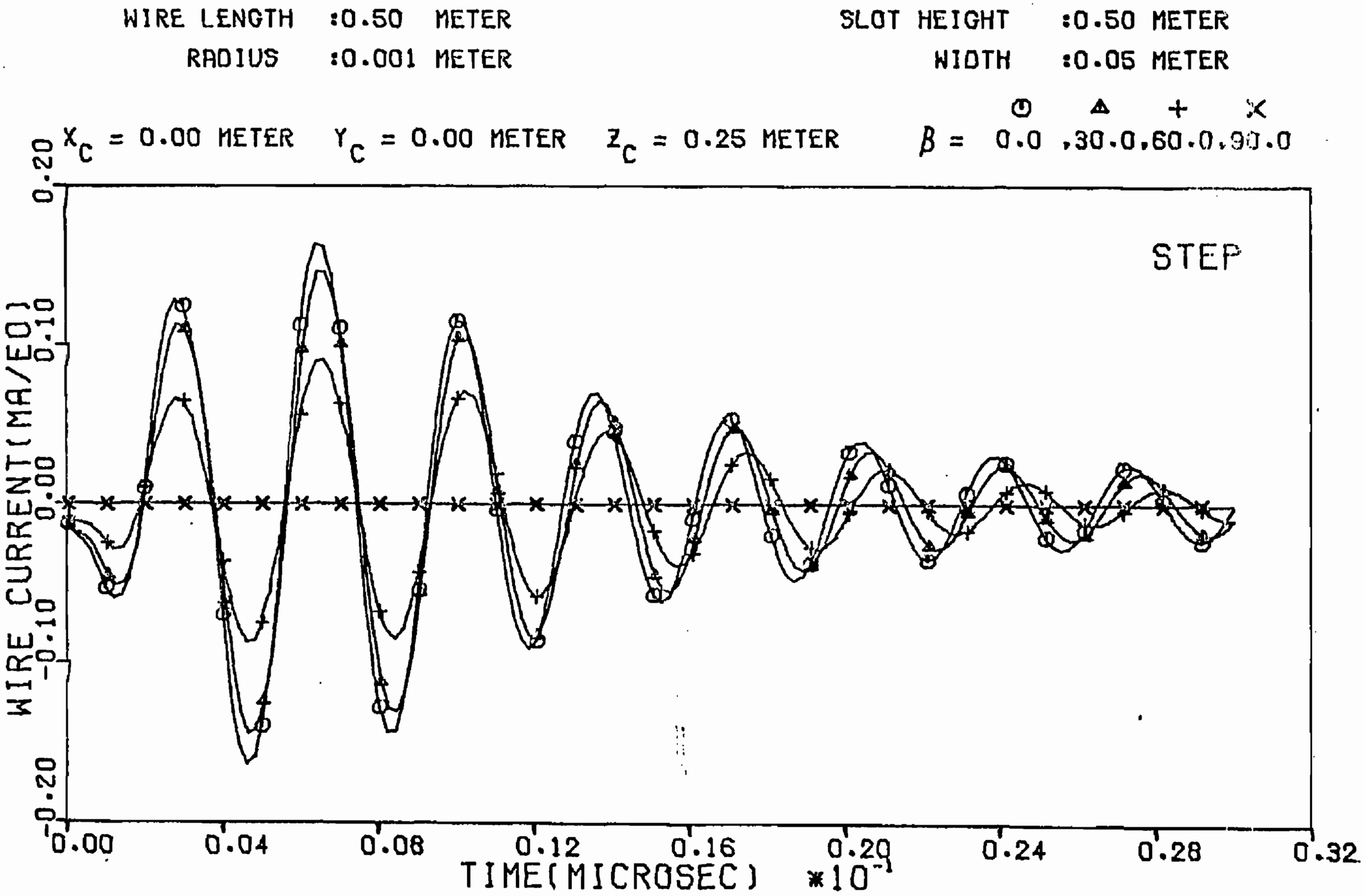

Figure 4.21 Time Domain Electric Current at the Center of Finite Wire in the Presence of Narrow Slot with Step Plane Wave Incident on Slot

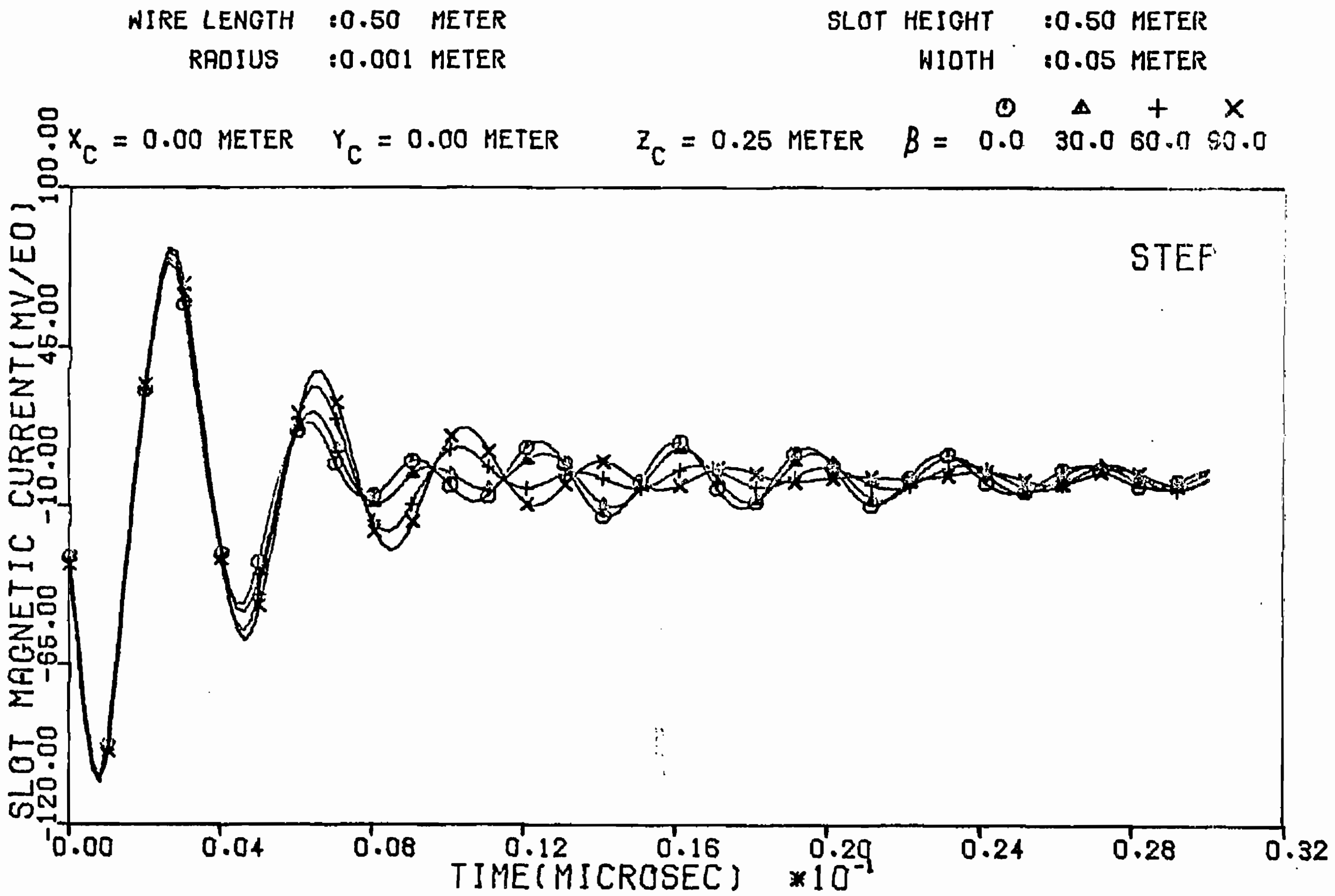

Figure 4.22 Time Domain Magnetic Current at the Center of Narrow Slot in the Presence of Finite Wire with Step Plane Wave Incident on Slot

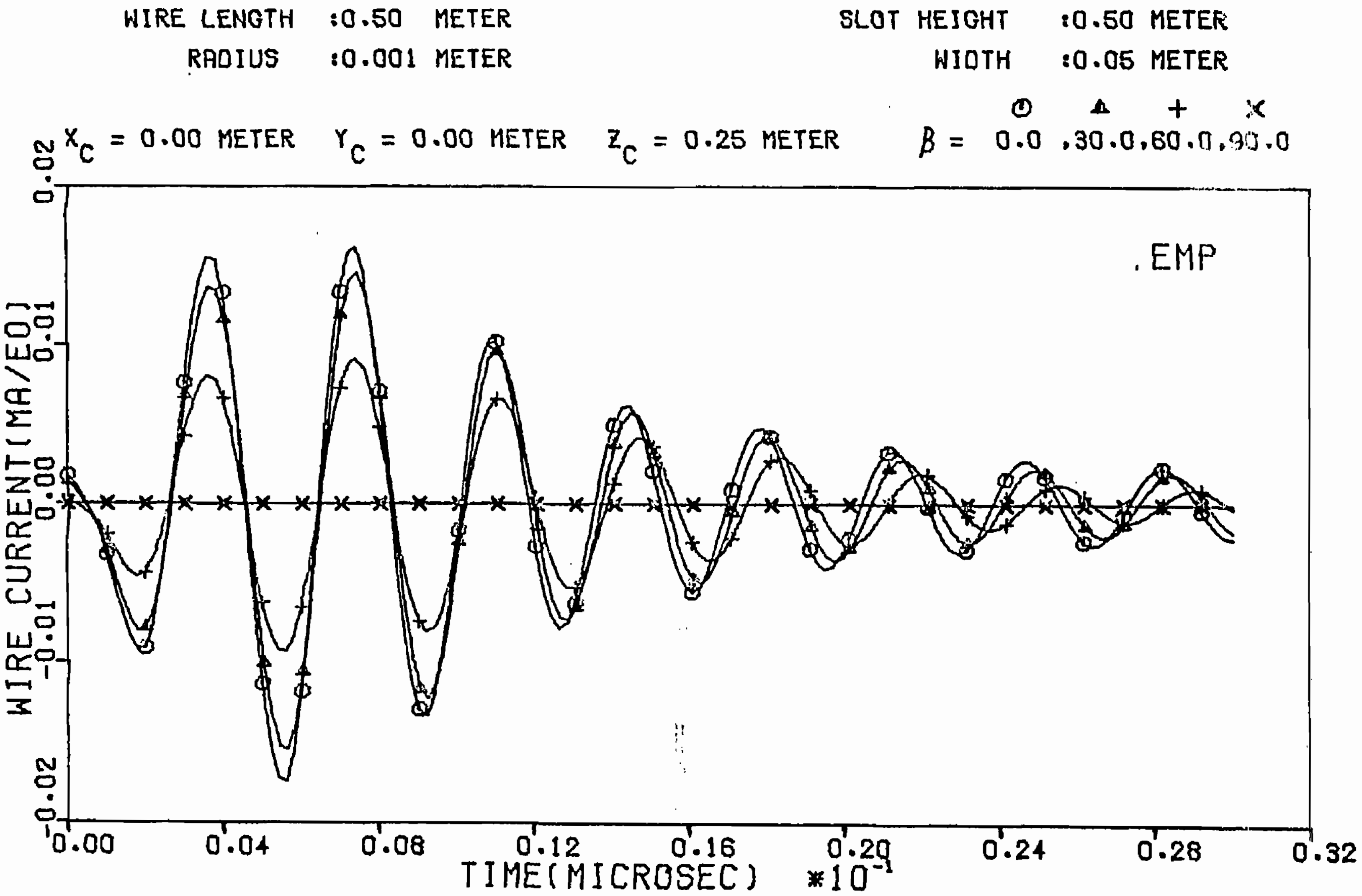

Figure 4.23 Time Domain Electric Current at the Center of Finite Wire in the Presence of Narrow Slot with EMP Incident on Slot

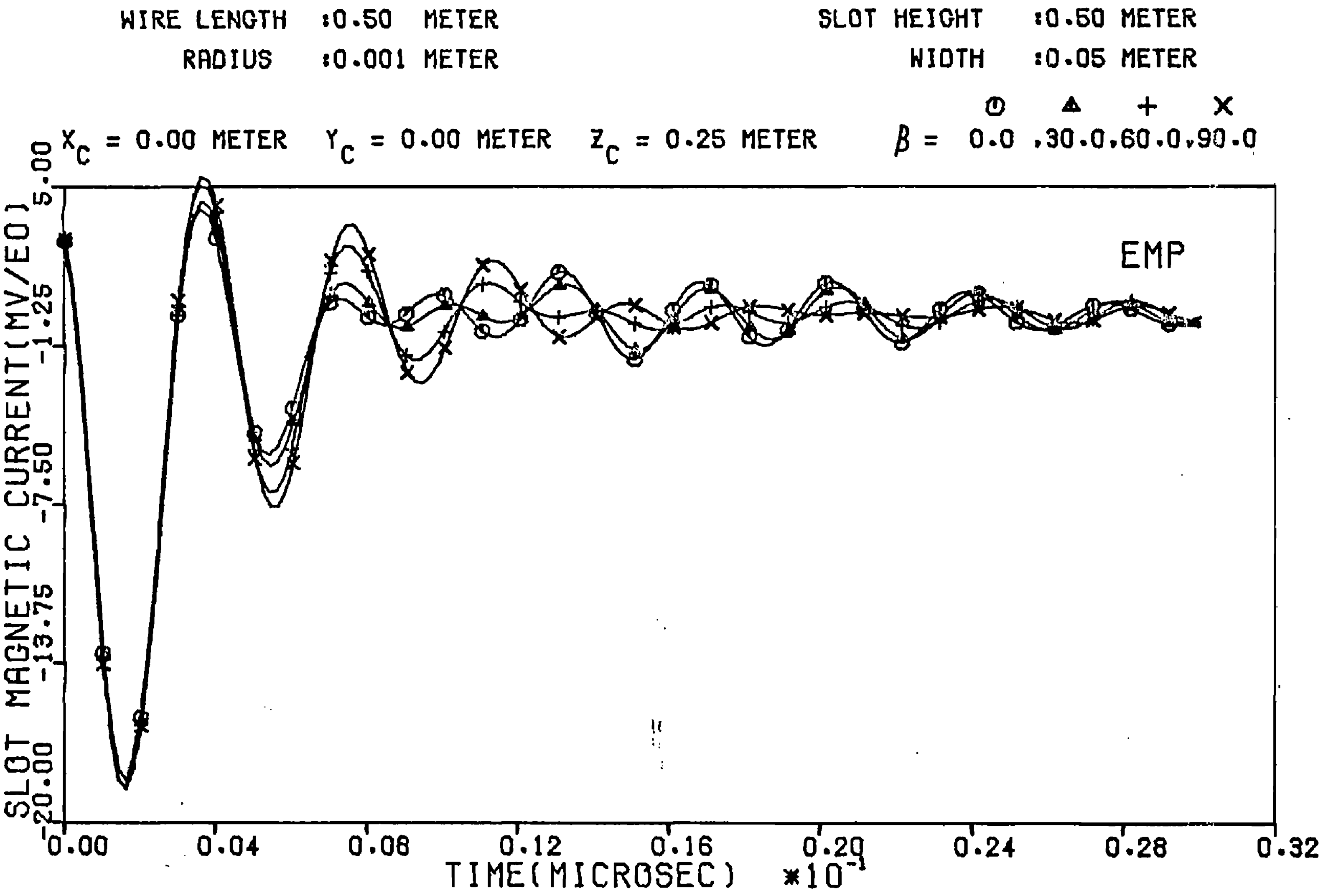

Figure 4.24 Time Domain Magnetic Current at the Center of Narrow Slot in the Presence of Finite Wire with EMP Incident on Slot

$$e^{i}(t) = E_o[-e^{-\alpha t} + e^{-\beta t}] \tag{4.24}$$

where

$$1/\alpha = 4.55 \text{ ns}$$
$$1/\beta = 300 \text{ ns}$$

E. Finite Wire Antenna Illuminating Narrow Slot Perforated Screen

This particular interaction problem is basically the same as the wire scatterer-slot case discussed previously except the slot is not excited any more by the incident field in the region $z < 0$, but is excited by the wire itself which is in turn excited by an ideal generator connected at $\zeta = 0$ as shown in figure 4.25. The coupled integral equations (4.13) and (4.14) still hold good for this problem with modification in the excitation terms. The right-hand side of the expression (4.13) is equated to zero, while the zero in the right-hand side of (4.14) is replaced by,

$$\tilde{V}(s) = -4\pi\gamma^2 V_o/s\mu \tag{4.25}$$

corresponding to the excitation of the ideal delta-gap generator at the center on the finite thin wire structure.

The natural resonant frequencies discussed previously apply for this geometry as well because the equations characterizing the coupling are the same.

In figures 4.26 and 4.27 are shown the frequency-domain response of the antenna current and the slot magnetic current distribution as a function of frequency. These results were obtained by directly solving the integral equations based on the method of moments in the real frequency domain with the substitution $s = j\omega$. Obviously, we observe the various resonances in the frequency response corresponding to the coupling.

In figures 4.28 and 4.29 are shown the corresponding transient response of the antenna current and the slot magnetic current respectively for a step input turned on at $t = 0$ across the antenna gap terminals.

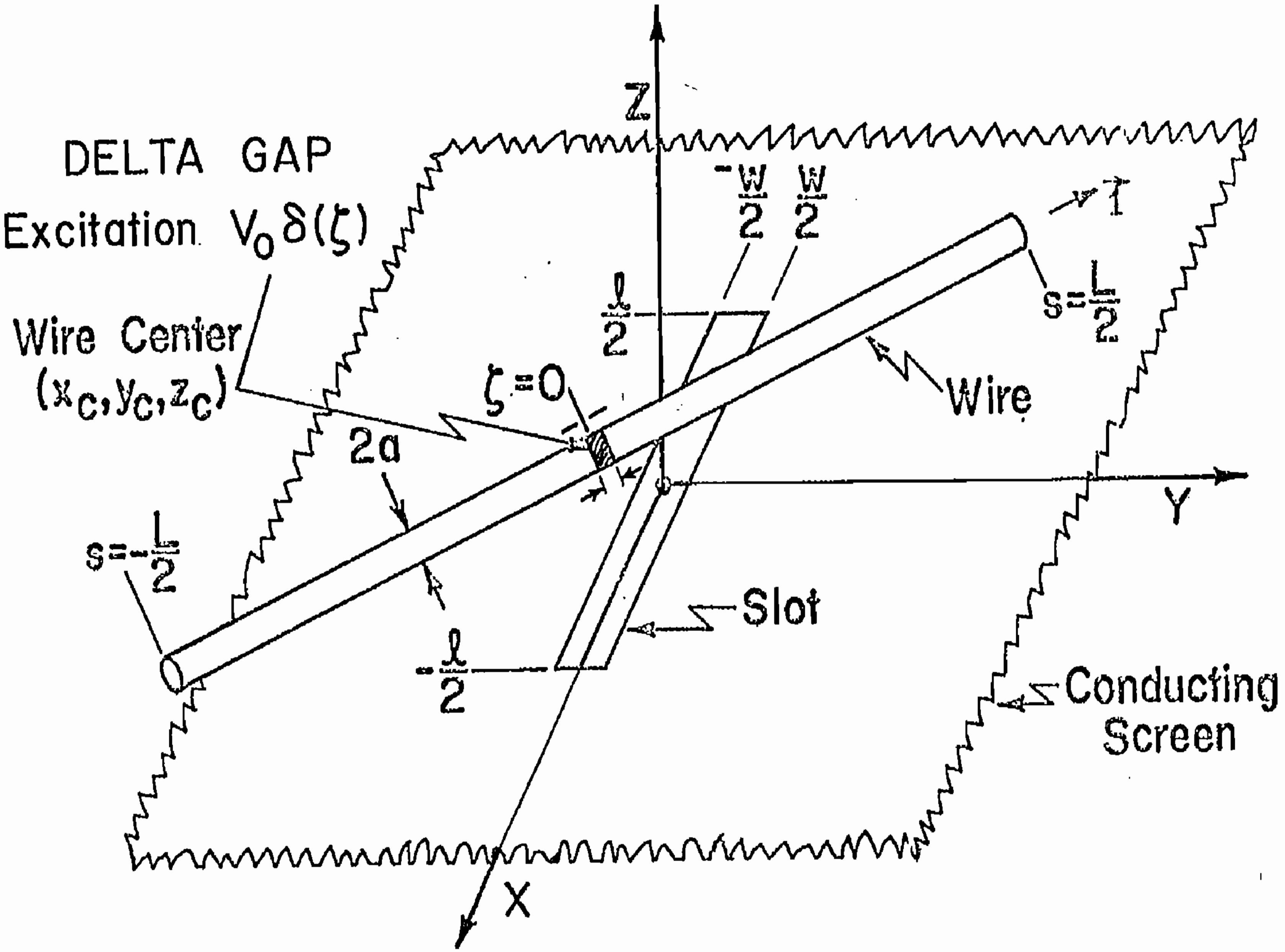

Figure 4.25 Finite Wire Antenna Behind Narrow Slot Conducting Screen

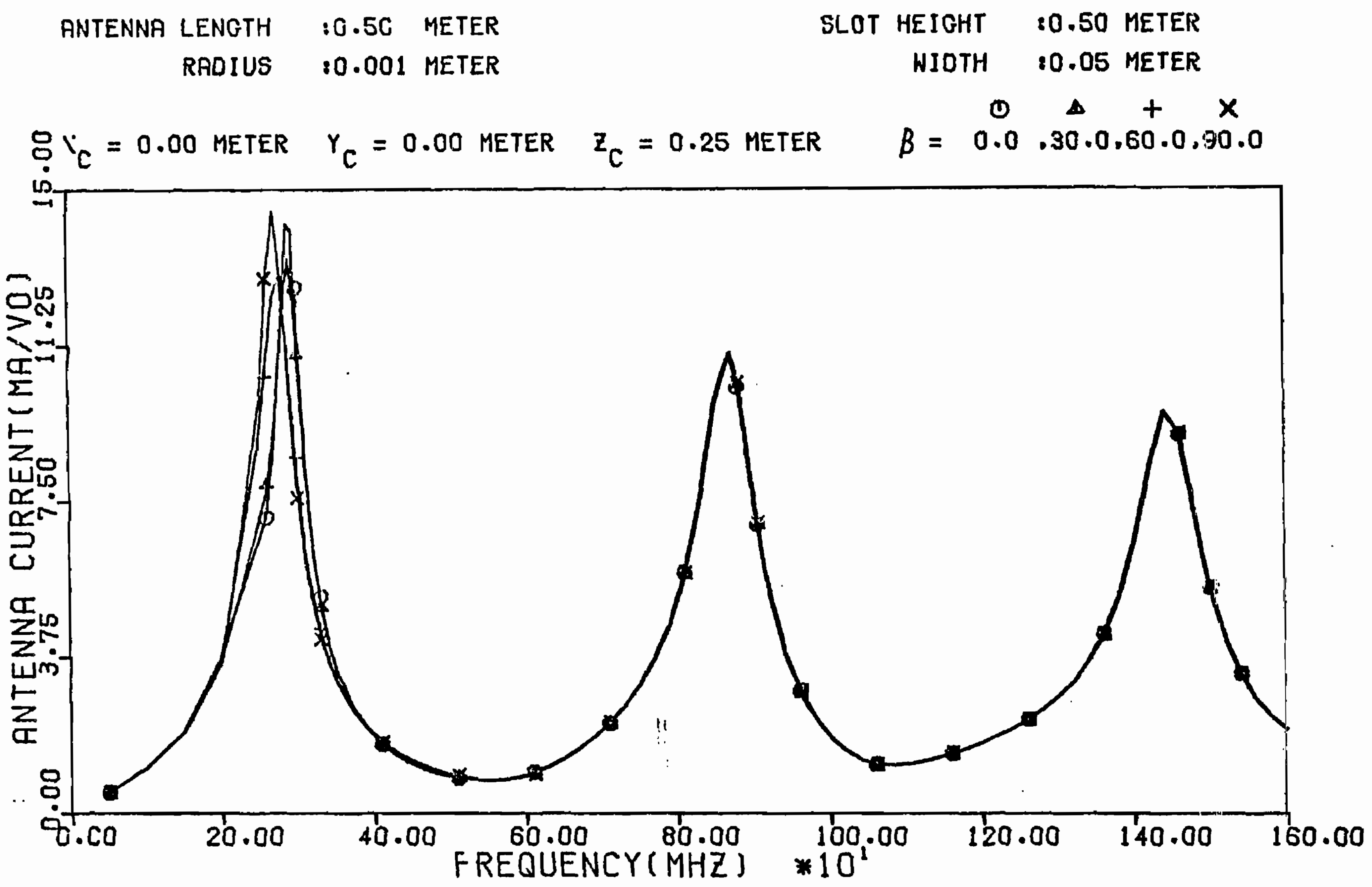

Figure 4.26 Electric Current on Finite Wire Antenna at Its Center in the Presence of Narrow Slot as a Function of Frequency

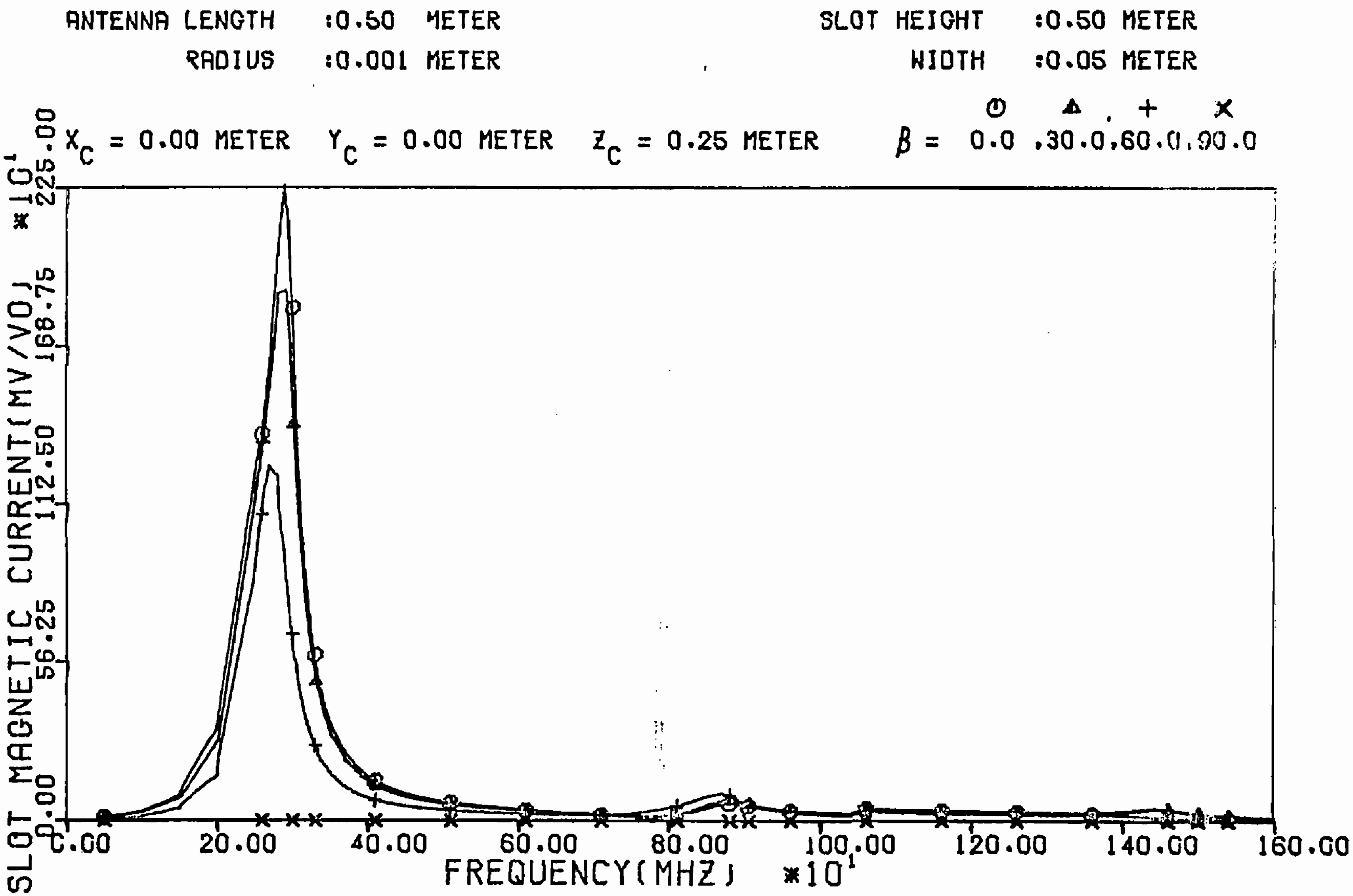

Figure 4.27 Axial Magnetic Current in Narrow Slot at Its Center in the Presence of Wire Antenna as a Function of Frequency

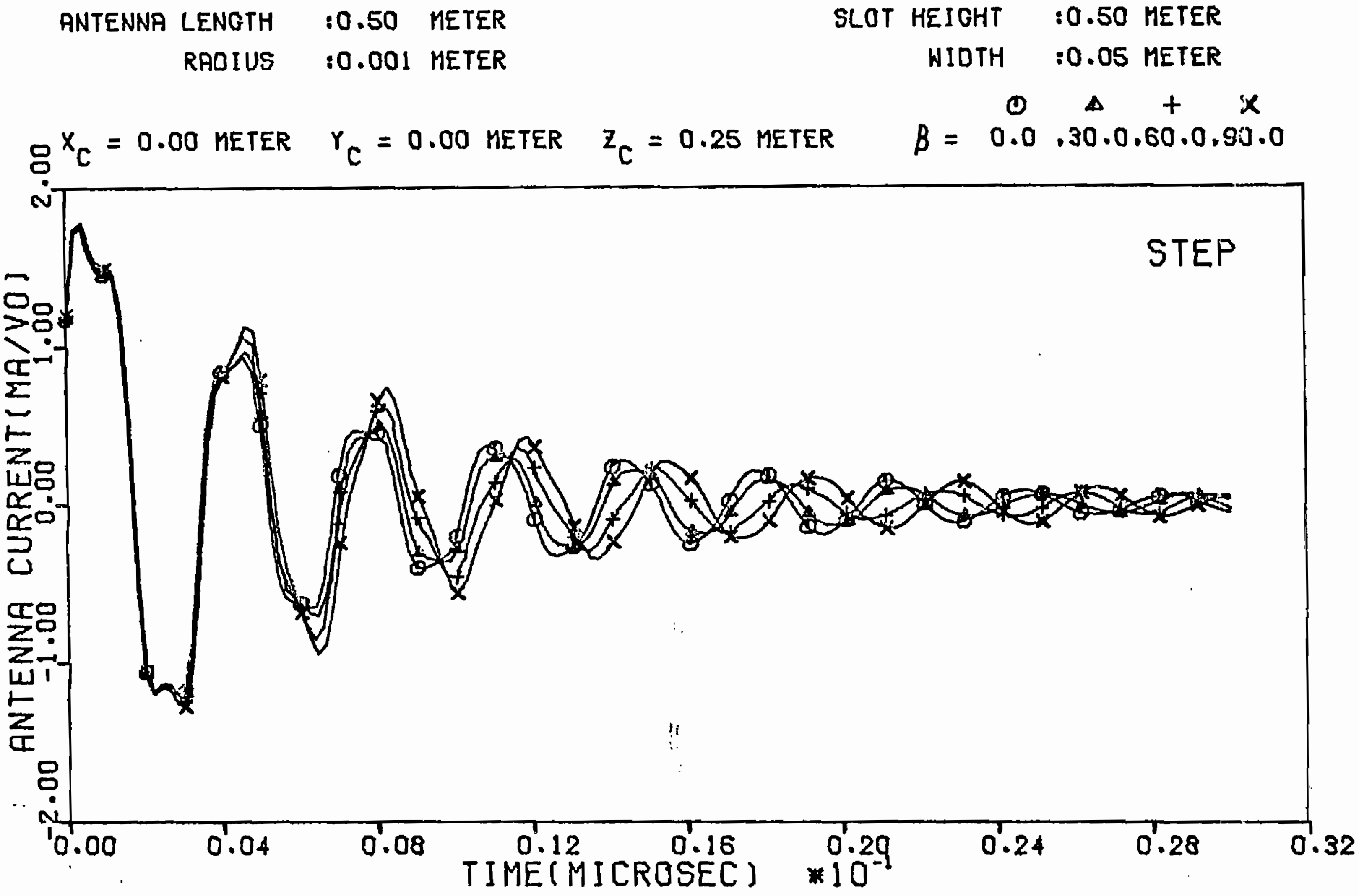

Figure 4.28 Time Domain Electric Current at the Center of Finite Wire Antenna in the Presence of Narrow Slot, with Step Excitation Turned on at t=0

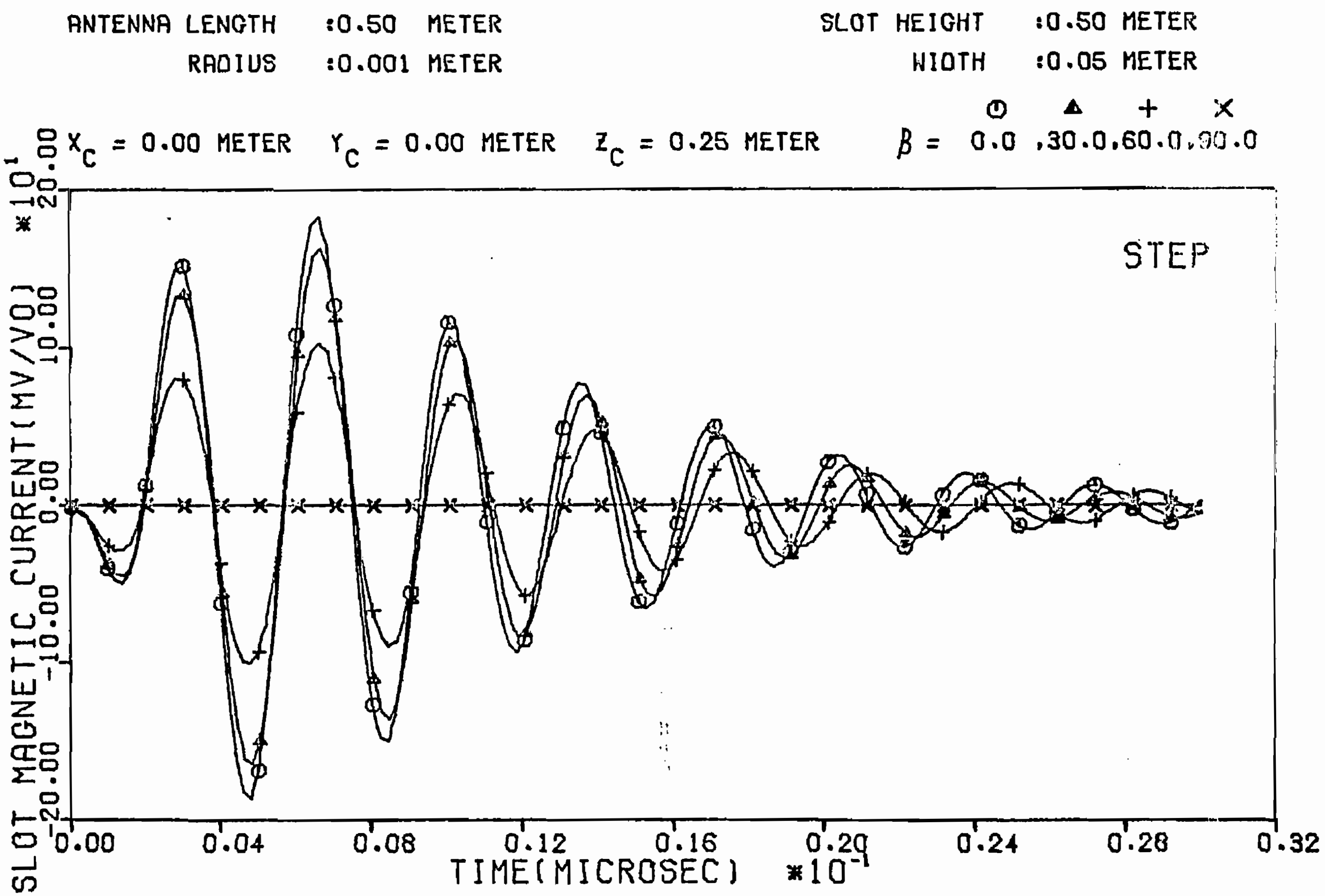

Figure 4.29 Time Domain Magnetic Current at the Center of Narrow Slot in the Presence of Wire Antenna, with Step Excitation Turned on at t=0

F. Equivalent Dipole Illuminating Narrow Slot in a Conducting Screen

This case is slightly different from the previous examples in that the finite wire was parallel to the screen containing the narrow slot. In the present problem the finite wire is perpendicular to the conducting screen and the excitation is by a delta gap generator at $z = 0$. The geometry of the interaction problem is shown in figure 4.30. The integral equations (1.15) and (1.18) can be specialized to the equivalent dipole slot geometry and the interaction is characterized by the following integral equations:

$$\left(\frac{\partial^2}{\partial z^2} - \gamma^2\right) \int_{z'=0}^{L/2} \tilde{I}(z') \, [\tilde{K}(z-z',a) + \tilde{K}(z+z',a)] \, dz'$$

$$+ 2s\varepsilon \int_{\zeta'=-\ell/2}^{\ell/2} \tilde{m}(\zeta') \, [-y_c \cos\alpha + x_c \cos\beta] \left(\frac{1}{r_2^3} + \frac{\gamma}{r_2^2}\right) e^{-\gamma r} \, d\zeta'$$

$$= -4\pi s\varepsilon V_o \, \delta(z) \qquad \text{on wire} \qquad (4.26)$$

$$- \frac{s\mu}{2} \int_{z'=0}^{L/2} \tilde{I}(z')[x_c \cos\beta - y_c \cos\alpha] \left(\frac{1}{R_2^3} + \frac{\gamma}{R_2^2}\right) e^{-\gamma R} \, dz'$$

$$+ \left(\frac{\partial^2}{\partial \zeta^2} - \gamma^2\right) \int_{\zeta'=-\ell/2}^{\ell/2} \tilde{m}(\zeta') \, \tilde{K}(\zeta-\zeta', \tfrac{w}{4}) \, d\zeta' = 0 \qquad \text{on slot} \quad (4.27)$$

where

$$r_2 = [z^2 + (x_c + \zeta' \cos\alpha)^2 + (y_c + \zeta' \cos\beta)^2]^{\frac{1}{2}} \qquad (4.28)$$

$$R_2 = [z'^2 + (x_c + \zeta \cos\alpha)^2 + (y_c + \zeta \cos\beta)^2]^{\frac{1}{2}} \qquad (4.29)$$

The above equations (4.26) and (4.27) are again reduced to matrix form and solved numerically. In figures 4.31 and 4.32 are shown the distribution of the induced electric current on the equivalent dipole in the presence of the narrow slot for a delta function excitation at $z = 0$. The distribution is similar to the one on an isolated equivalent dipole except for minor variation due to the

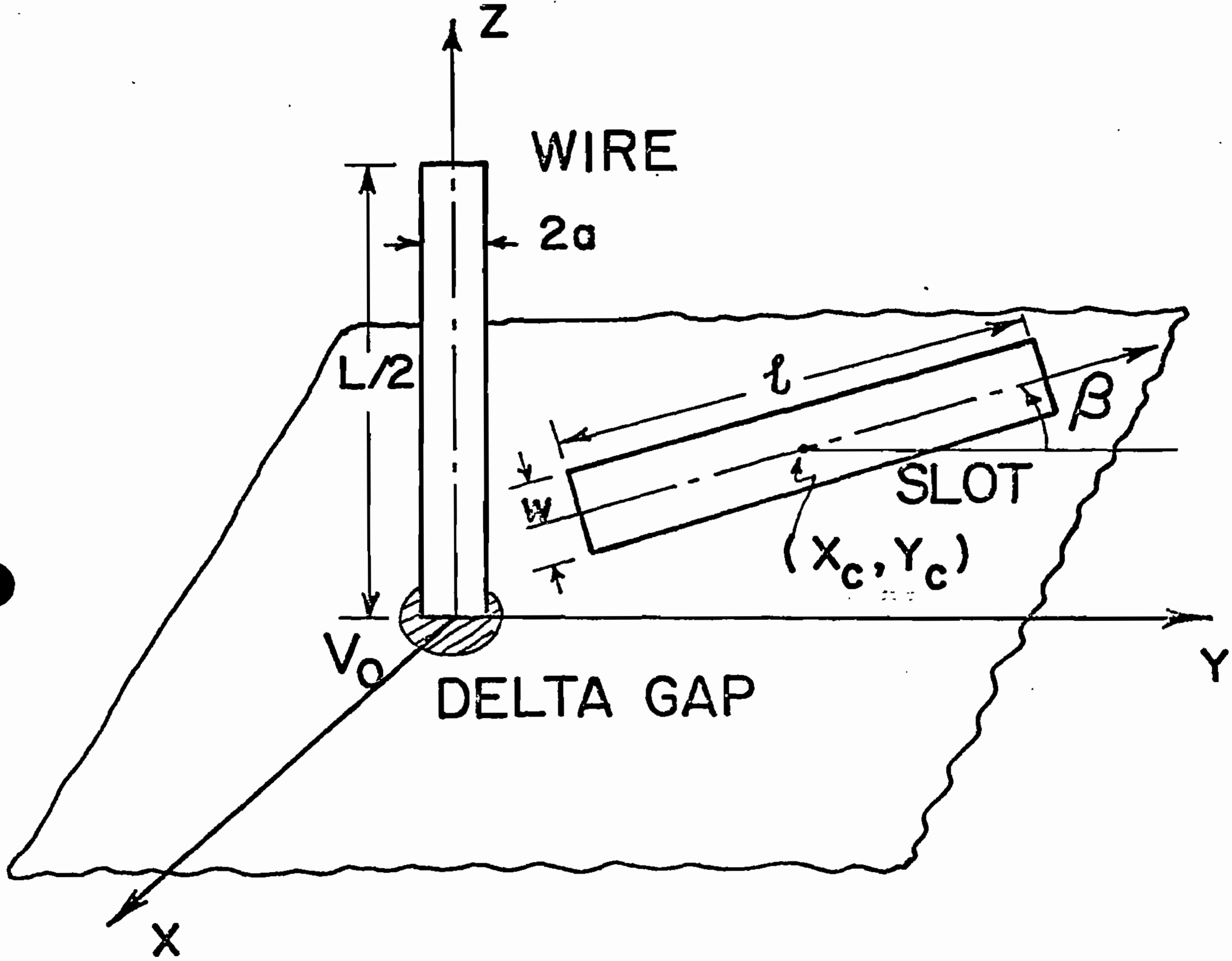

Figure 4.30 Equivalent Dipole Exciting Narrow Slot Perforated Conducting Screen

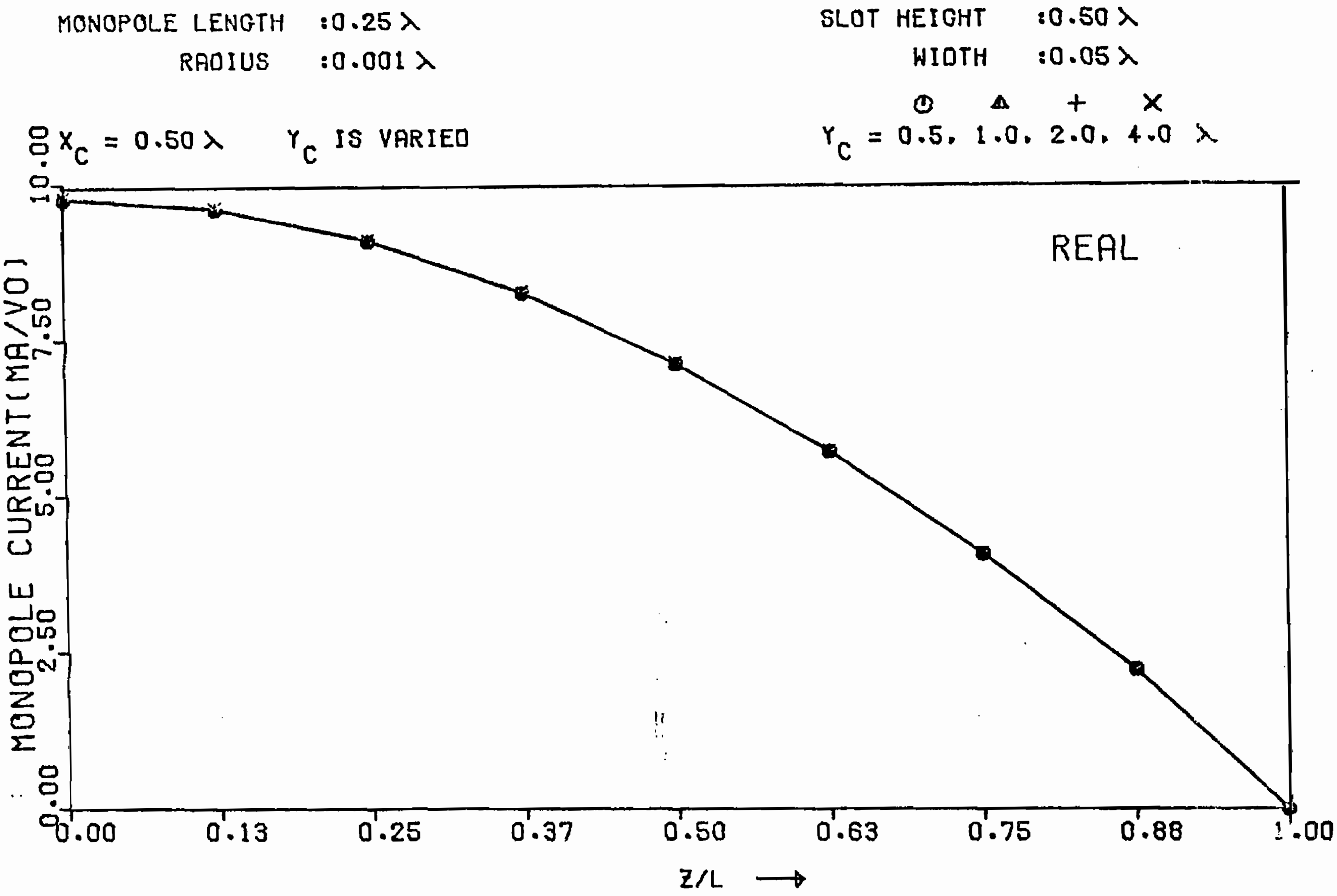

Figure 4.31 Real Part of the Electric Current on Equivalent Dipole in the Presence of Narrow Slot for cosβ=1

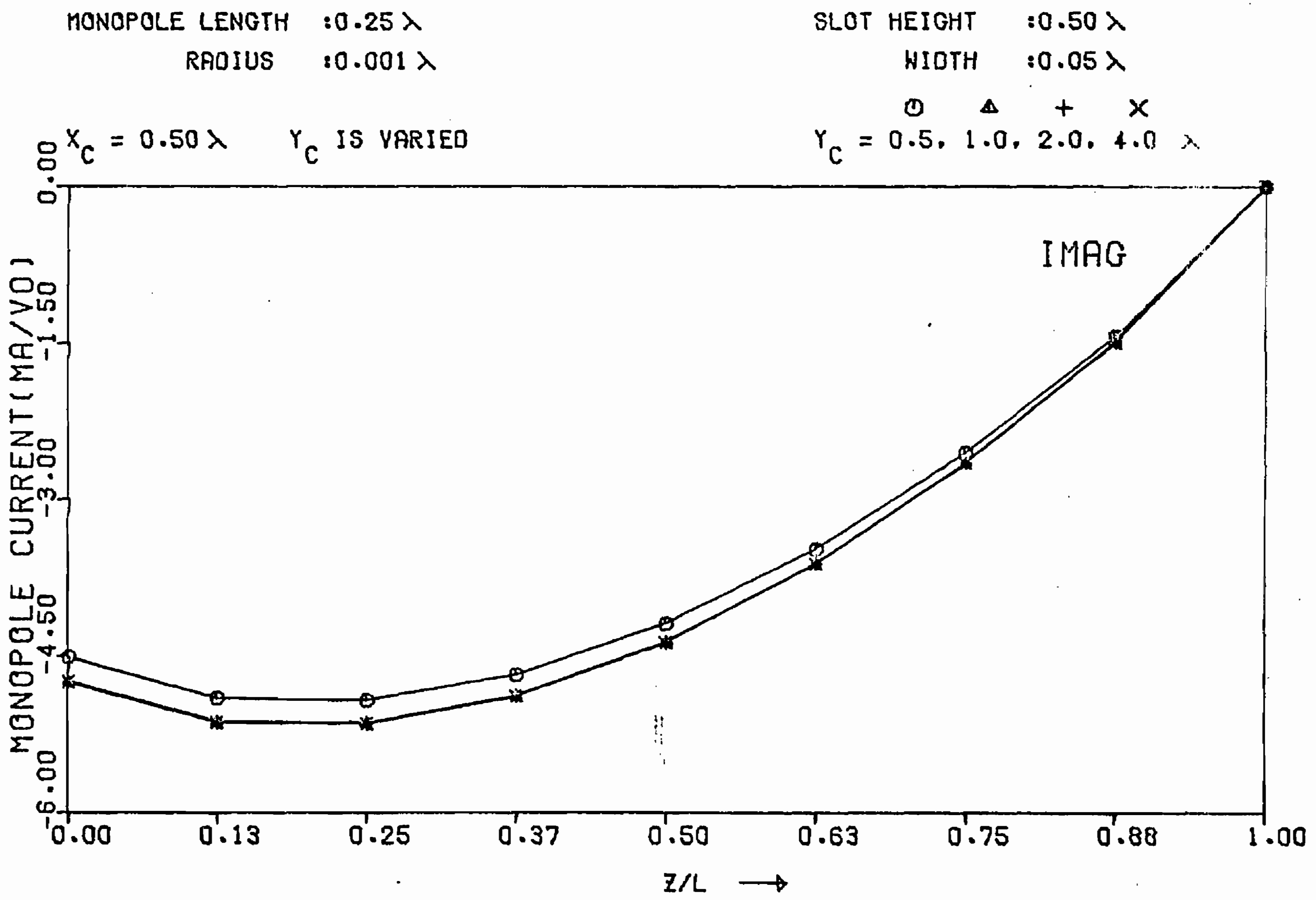

Figure 4.32 Imaginary Part of the Electric Current on Equivalent Dipole in the Presence of Narrow Slot for cosβ=1

presence of the slot. The corresponding slot axial magnetic current distributions are shown in figures 4.33 and 4.34 in the presence of the equivalent dipole. There is slight asymmetry in the slot distribution due to its orientation with respect to the monopole. In the figures 4.35 and 4.36 are shown the real and imaginary parts of the equivalent dipole input impedance calculated for the different locations of the narrow slot. As the slot is moved away, the effect on the impedance of the equivalent dipole is negligible for the resonant equivalent dipole.

The time-domain responses are shown in figures 4.37 through 4.40. Figure 4.37 gives the monopole current at the feed point as a function of time with unit step input turned on at t = 0, and the corresponding slot magnetic current at the center of the slot is shown in figure 4.38. As the slot position is varied the time response of the slot changes, but there is little effect on the monopole time domain response.

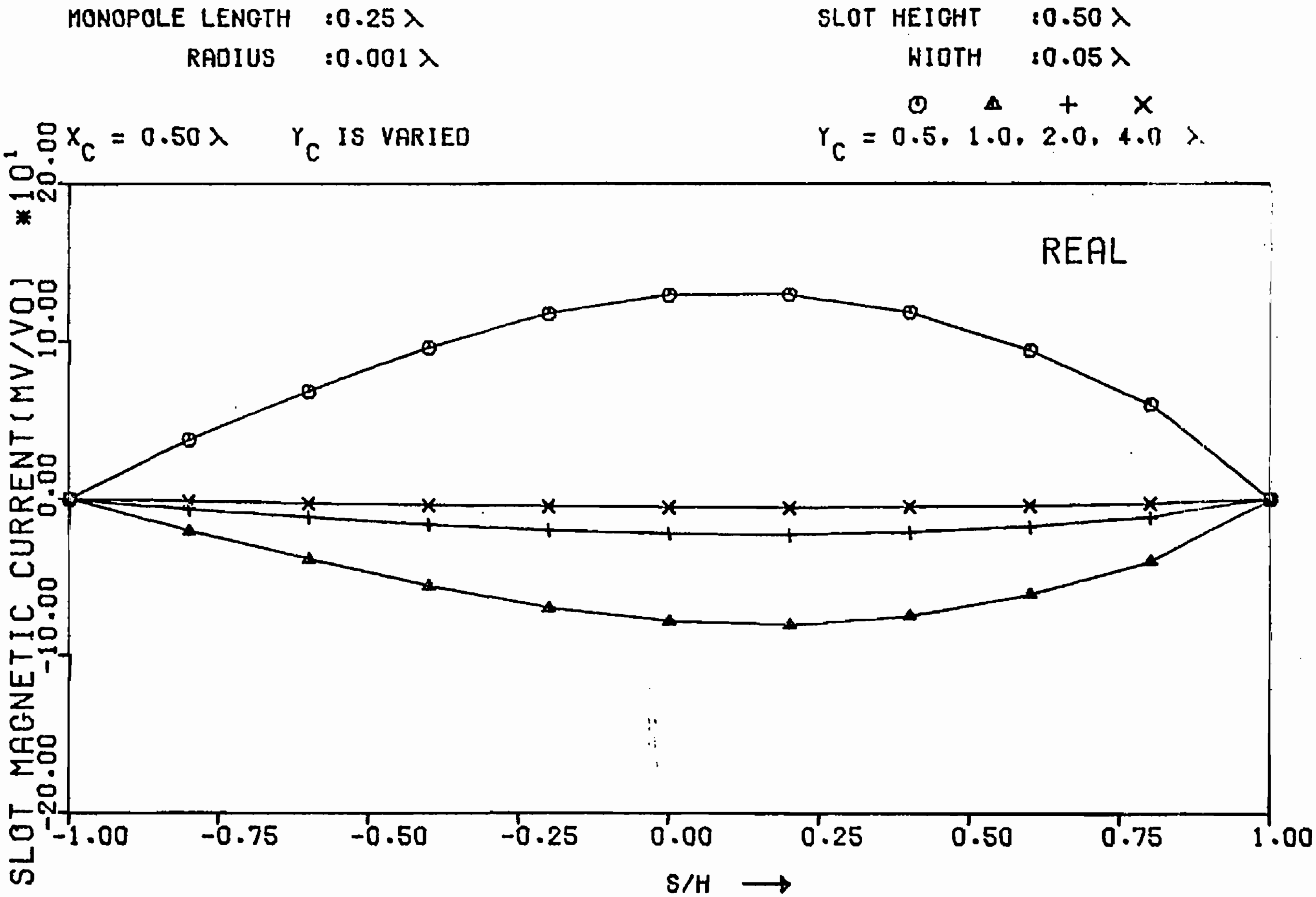

Figure 4.33 Real Part of the Axial Magnetic Current in Slot in the Presence of Equivalent Dipole for cosβ=1

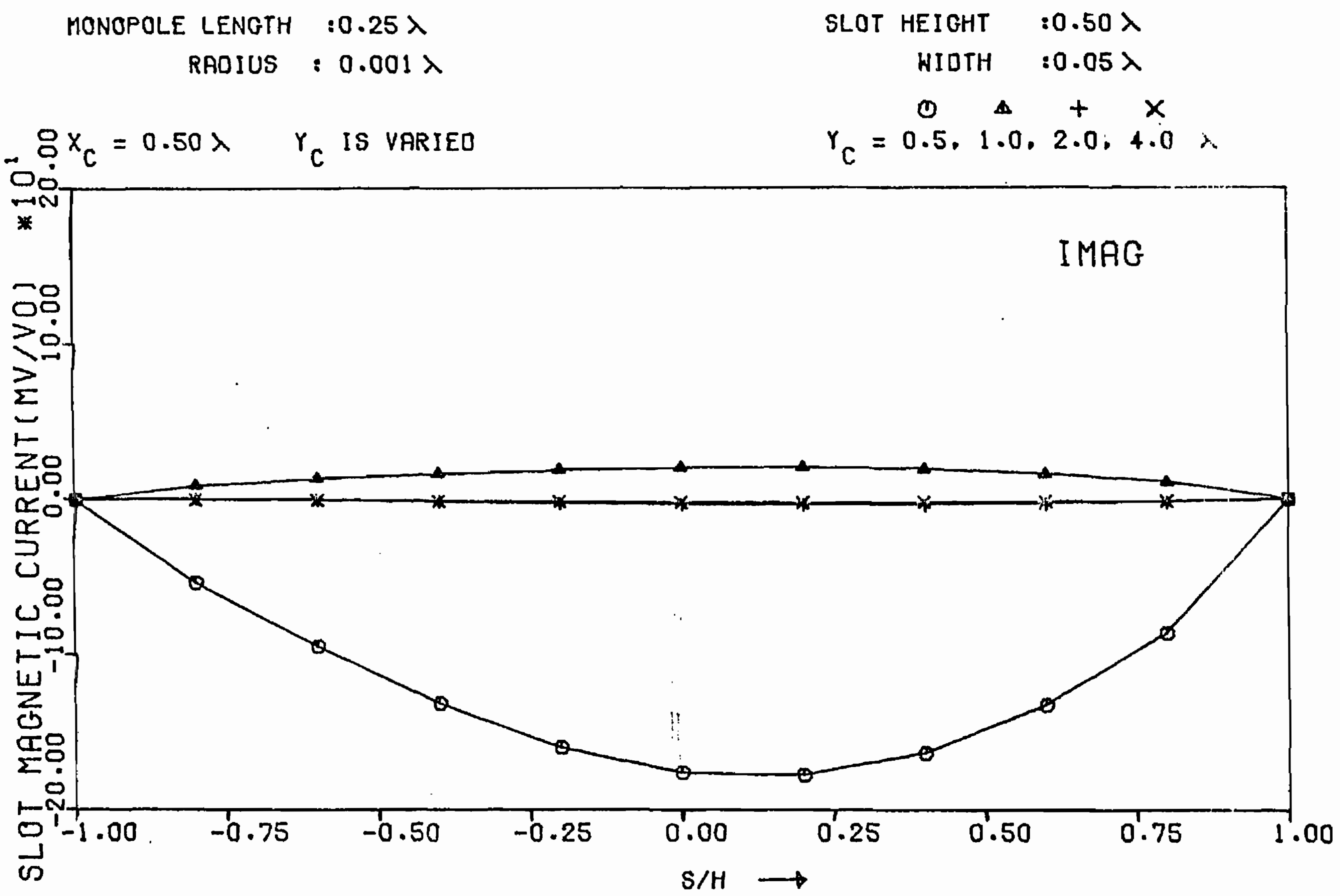

Figure 4.34 Imaginary Part of the Axial Magnetic Current in Slot in the Presence of Equivalent Dipole for cosβ=1

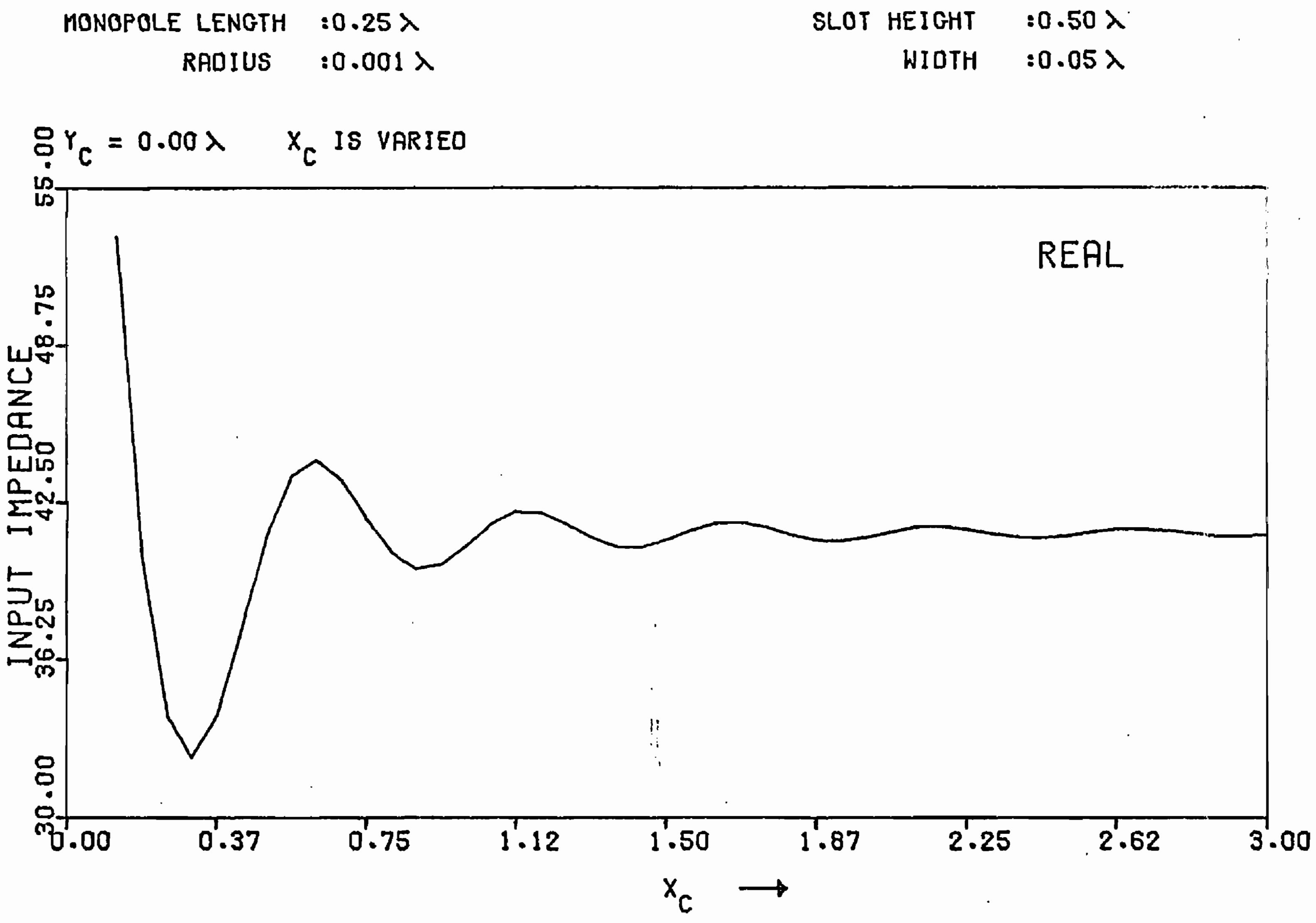

Figure 4.35 Real Part of Input Impedance of Equivalent Dipole in the Presence of Narrow Slot for $\cos\beta=1$

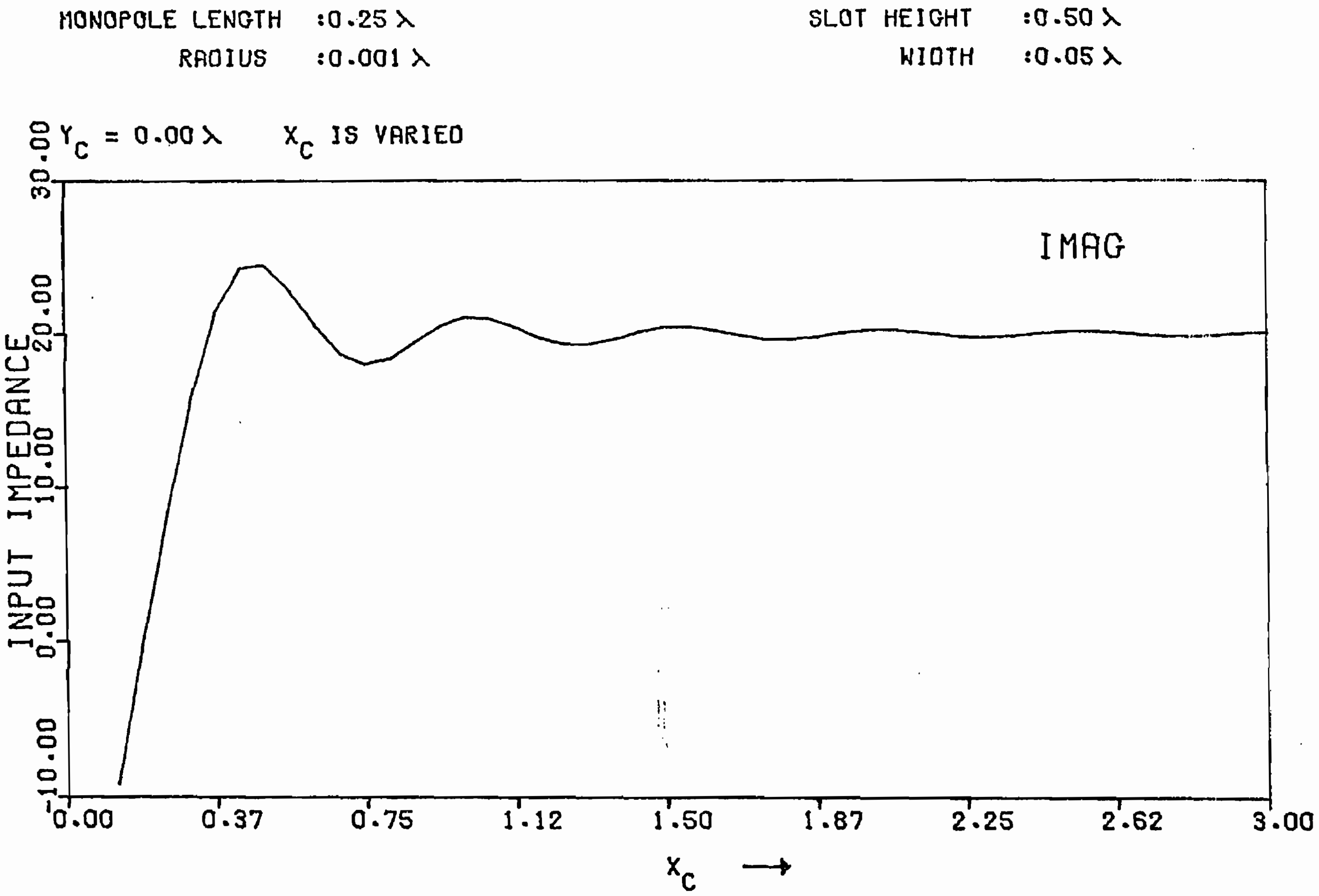

Figure 4.36 Imaginary Part of Input Impedance of Equivalent Dipole in the Presence of Narrow Slot for cosβ=1

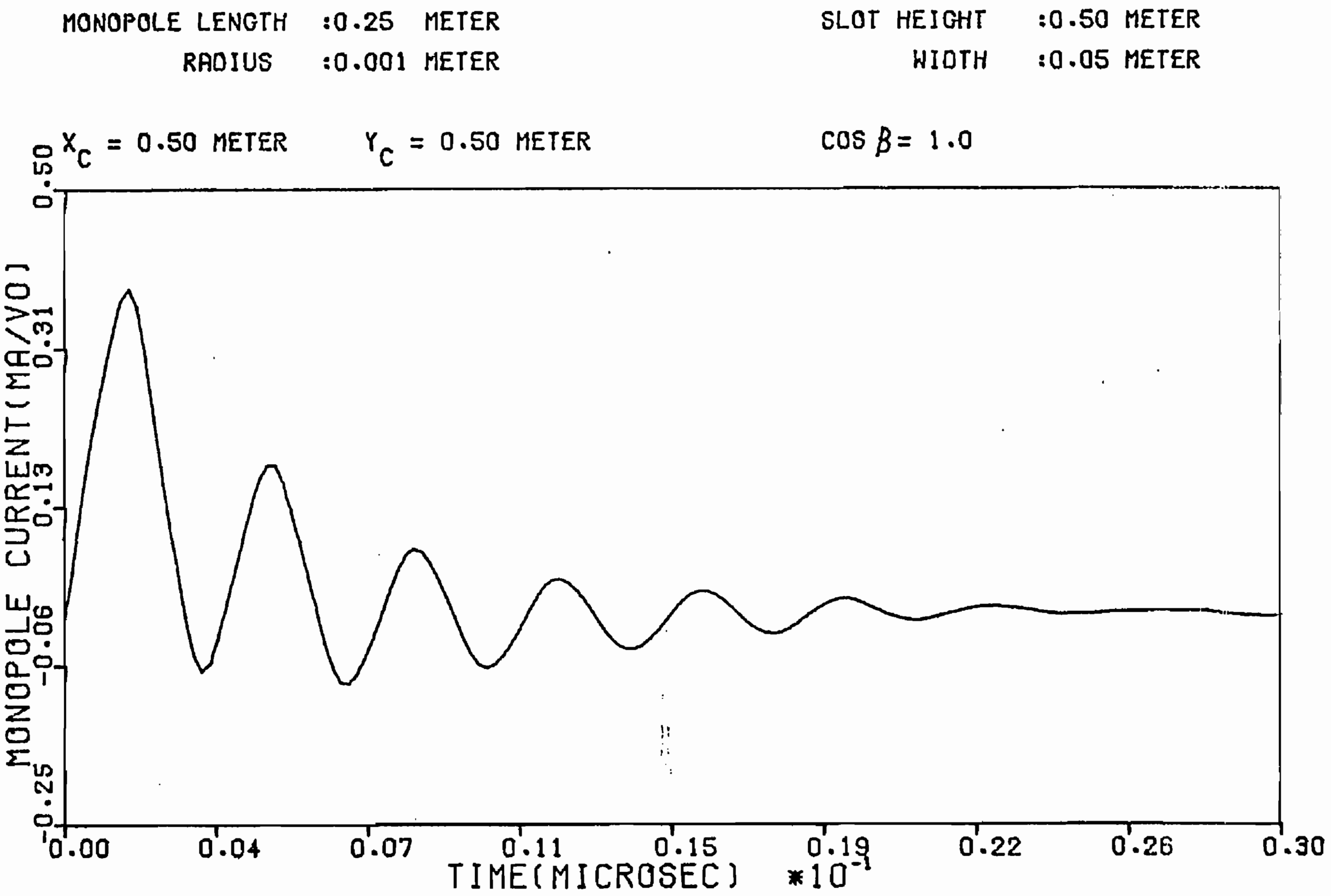

Figure 4.37 Time Domain Electric Current on Equivalent Dipole at the Feed Point in the Presence of Narrow Slot, Turned on at t=0, for (x_c,y_c)=(0.5,0.5)

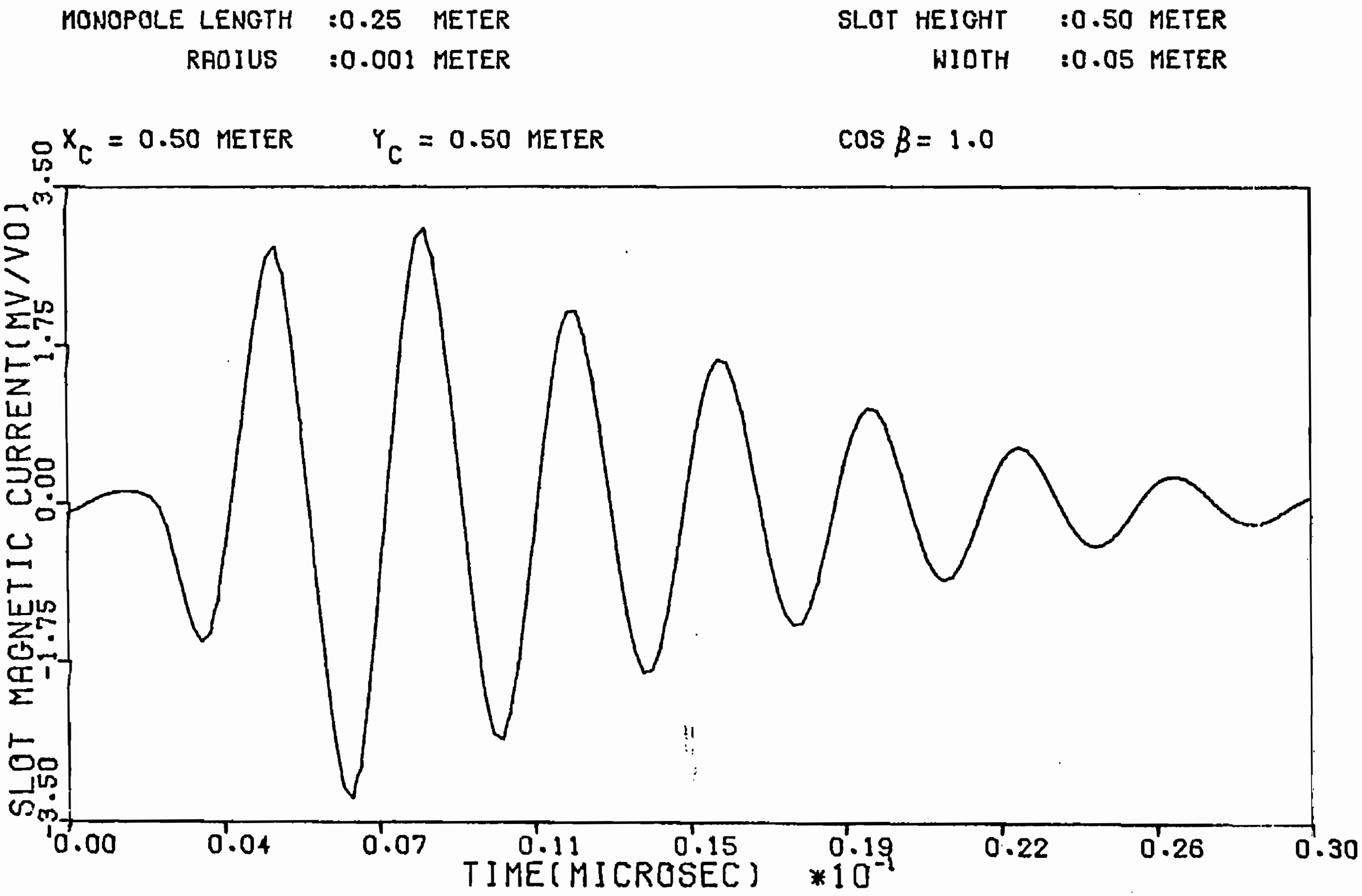

Figure 4.38 Time Domain Axial Magnetic Current at the Center of Narrow Slot in the Presence of Equivalent Dipole, Turned on at t=0, for $(x_c,y_c)=(0.5,0.5)$

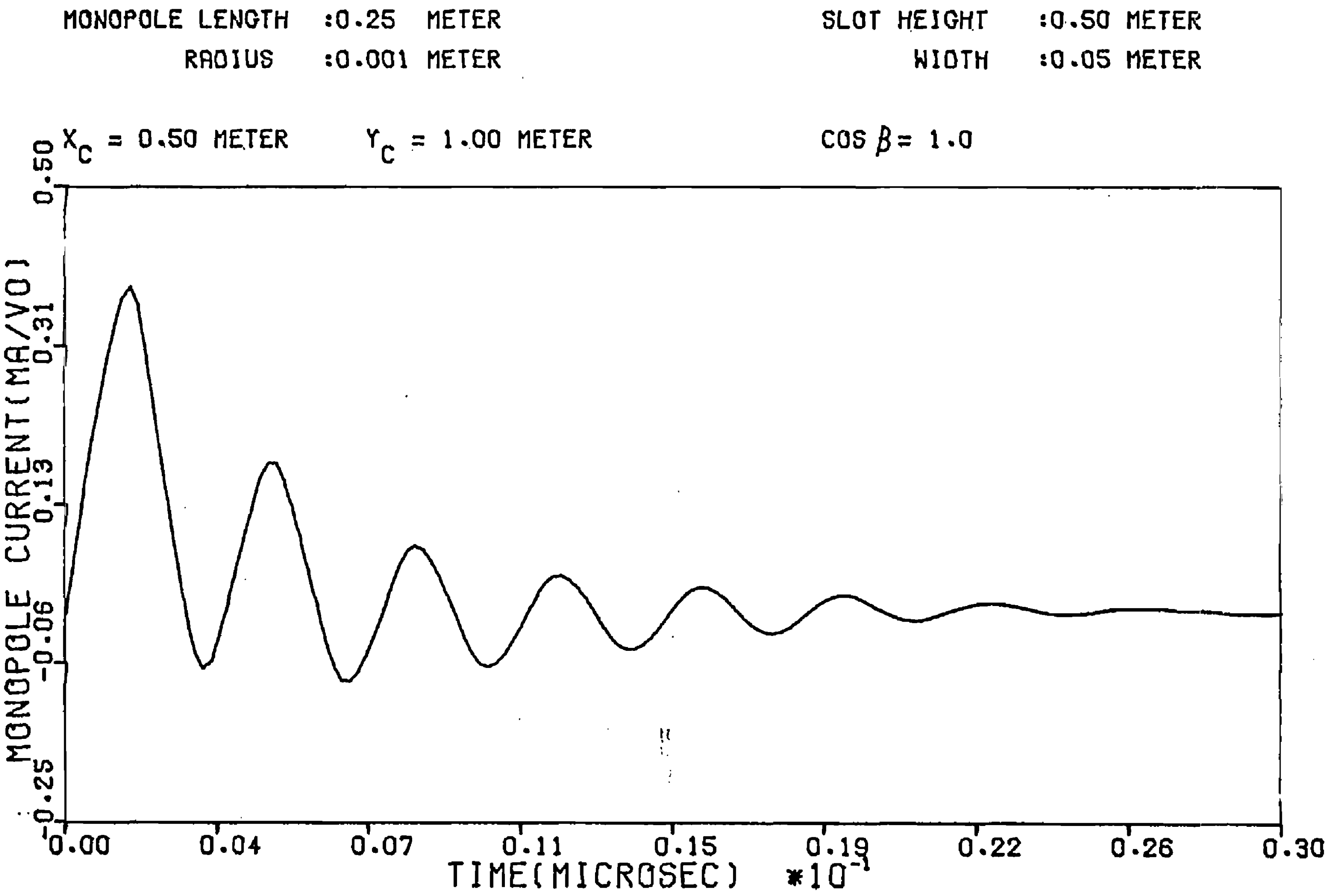

Figure 4.39 Time Domain Electric Current on Equivalent Dipole at the Feed Point in the Presence of Narrow Slot, Turned on at t=0, for (x_c,y_c)=(0.5,1.0)

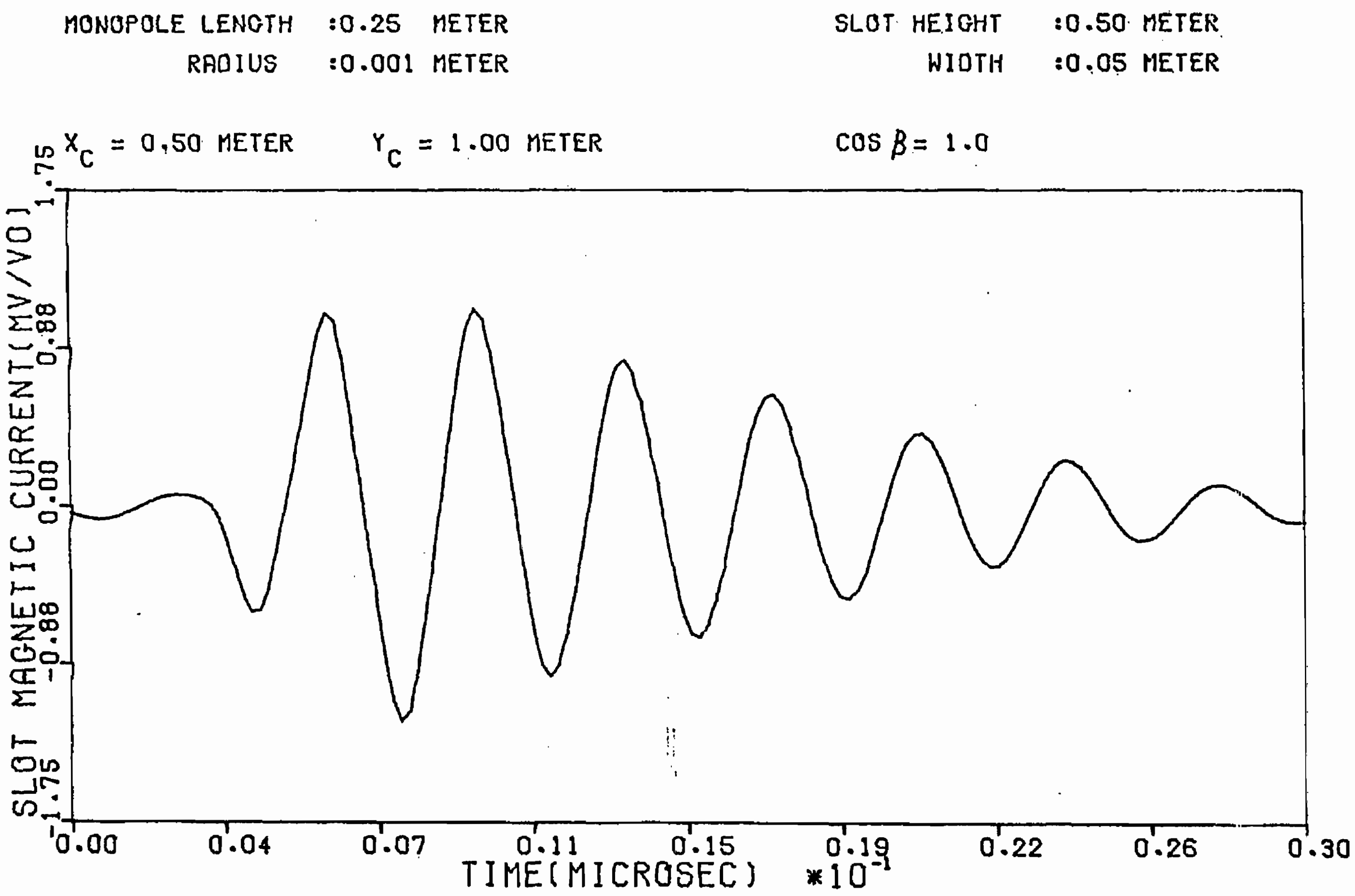

Figure 4.40 Time Domain Axial Magnetic Current at the Center of Narrow Slot in the Presence of Equivalent Dipole, Turned on at t=0, for $(x_c,y_c)=(0.5,1.0)$

SUMMARY

In this note there is reported the preliminary investigation of the interaction problem of the conducting bodies behind aperture screen geometries based on the formulation of the integral equation approach and subsequent numerical analysis. To characterize the complex interaction problem step by step, apertures in the form of a narrow slot, and rectangular and square apertures are analyzed separately; similarly the finite and infinite wire geometries above conducting ground plane are treated separately and some numerical results are reported in the frequency domain. Further simple objects in the form of finite wire antenna and scatterer geometries are characterized in the presence of narrow finite slot geometry. The Singularity Expansion Method is applied for transient characterization and an attempt is made to explain the interaction between the wire and the aperture-screen. Both the narrow slot and finite wire responses are reported in the frequency and the time domains.

The reader may refer to [30] for the analysis of the infinite wire behind a narrow slot in a conducting screen. The general analysis of infinitely long multiple wires behind arbitrarily shaped apertures and the subsequent characterization of such regions in terms of an equivalent circuit including aperture resonance effects will be reported in an upcoming separate note.

REFERENCES

1. C. E. Baum, "EMP Simulators for Various Types of Nuclear EMP Environments: An Interim Categorization," Sensor and Simulation Note 151, July 1972.

2. C. E. Baum, "On the Singularity Expansion Method for the Solution of Electromagnetic Interaction Problems," Interaction Note 88, December 1971.

3. C. E. Baum, K. C. Chen, and B. K. Singaraju, "Categorization of the Types of Apertures," Interaction Note 219, January 1975.

4. C. D. Taylor, "Electromagnetic Pulse Penetration Through Small Apertures," Interaction Note 74, March 1971.

5. D. R. Wilton and O. C. Dunaway, "Electromagnetic Penetration Through Apertures of Arbitrary Shape: Formulation and Numerical Solution Procedure," Interaction Note 214, July 1974.

6. T.B.A. Senior and G. A. Desjardins, "Field Penetration into a Spherical Cavity," Interaction Note 142, August 1973.

7. K. C. Chen, "Apertures with Various Items Behind," 1974 Spring FULMEN Meeting.

8. D. Kajfez, "Excitation of a Terminated TEM Transmission Line Through Small Apertures," Interaction Note 215, July 1974.

9. C. M. Butler and K. R. Umashankar, "Electromagnetic Excitation of a Wire Through an Aperture Perforated Conducting Screen, Interaction Note 251, July 1975.

10. C. J. Bouwkamp, "Theoretical and Numerical Treatment of Diffraction Through a Circular Aperture," IEEE Trans. on Antennas and Propagation, AP-18, No. 2, March 1970.

11. K. R. Umashankar and C. M. Butler, "A Numerical Solution Procedure for Small Aperture Integral Equations," Interaction Note 212, July 1974.

12. D. R. Wilton, C. M. Butler, and K. R. Umashankar, "Penetration of Electromagnetic Fields Through Small Apertures in Planar Screens: Selected Data," Interaction Note 213, September 1974.

13. Y. Rahmat-Samii and R. Mittra, "A New Integral Equation Solution of Electromagnetic Aperture Coupling and Thin Plate Scattering Problems," Interaction Note 224, February 1975.

14. C. M. Butler and K. R. Umashankar, "Electromagnetic Penetration Through an Aperture in an Infinite Planar Screen Separating Two Half Spaces of Different Electromagnetic Properties," Radio Science, Vol. II, No. 7, July 1976.

15. C. E. Baum and B. K. Singaraju, "Generalization of Babinet's Principle in Terms of the Combined Field to Include Impedance Loaded Aperture Antennas and Scatterers," Interaction Note 217, September 1974.

16. R. F. Harrington, Field Computation by Moment Methods, MacMillan, New York, 1968.

17. C. E. Baum, "Emerging Technology for Transient and Broadband Analysis and Synthesis of Antennas and Scatterers," Proc. of the IEEE, Vol. 64, November 1976.

18. K. R. Umashankar and D. R. Wilton, "Transient Scattering by a Thin Wire in Free Space and Above Ground Plane Using the Singularity Expansion Method," Interaction Note 236, August 1974.

19. K. R. Umashankar and D. R. Wilton, "Transient Characterization of Circular Loop Using the Singularity Expansion Method," Interaction Note 259, August 1974.

20. D. R. Wilton and K. R. Umashankar, "Parametric Study of an L-Shaped Wire Using the Singularity Expansion Method," Interaction Note 152, November 1973.

21. R. F. Harrington, Time Harmonic Electromagnetic Fields, McGraw-Hill, 1961.

22. W. L. Weeks, Electromagnetic Theory for Engineering Applications, John Wiley and Sons, New York, 1964.

23. C. M. Butler, K. R. Umashankar, and C. E. Smith, "Theoretical Analysis of the Wire Biconical Antenna," Technical Report, U. S. Army Communications-Electronics, Fort Huachuca, Arizona, January 1975.

24. C. C. Kao, "Electromagnetic Scattering from a Finite Tubular Cylinder: Numerical Solutions and Data, Pt. I; Development of Theory," USAF Cambridge Research Labs., Cambridge, Mass., Rep. AF CRL-69-0535(1), Contract F19628-68-C-0030, December 1969.

25. C. C. Kao, "Electromagnetic Scattering from a Finite Tubular Cylinder: Numerical Solutions and Data, Pt II: Tables," USAF Cambridge Research Labs., Cambridge, Mass., Rep. AFCRL-69-0535 (2), Contract F19628-68-C-0030, December 1969.

26. C. C. Kao, "Three-Dimensional Electromagnetic Scattering from a Circular Tube of Finite Length," J. Appl. Phys., Vol. 40, November 1969, pp. 4732-4740.

27. C. W. Harrison, Jr., "Missile Circumferential Current Density for Plane Wave Electromagnetic Field Illumination," Interaction Note 60, July 1970.

28. R. V. Row, "Electromagnetic Scattering from Two Parallel Conducting Circular Cylinders," Cruft Laboratory, Harvard University, Tech. Rep. No. 170, 1953.

29. G. O. Olaofe, "Scattering by Two Cylinders," Radio Science, Vol. 5, No. 11, November 1970, pp. 1351-1360.

30. K. R. Umashankar and J. R. Wait, "Electromagnetic Coupling in an Infinite Cable Placed Behind a Slot Perforated Screen," Interaction Note 330, June 1977.